NTNU – Trondheim
Norwegian University of
Science and Technology

Numerical Analysis of Primary Stability on Cementless Hip Prostheses

Sindre Nordmark Olufsen

Master of Science in Product Design and Manufacturing
Submission date: June 2012
Supervisor: Bjørn Helge Skallerud, KT

Norwegian University of Science and Technology
Department of Structural Engineering

Master Thesis

Numerical Analysis of Primary Stability on Cementless Hip Prostheses

Sindre Nordmark Olufsen

Supervisor:
Bjørn Skallerud

Trondheim, June 11th, 2012

NTNU
Norwegian University of
Science and Technology

Faculty of Engineering Science and Technology
DEPARTMENT OF STRUCTURAL MECHANICS

To My Family

Department of Structural Engineering

FAKULTY OF ENGINEERING SCIENCE AND TECHNOLOGY
NTNU – Norwegian University of Science and Technology

MASTER THESIS 2012

for

Sindre Olufsen

Numerical Analysis of Primary Stability of Cementless Hip Prostheses

Numerisk analyse av usementerte hofteprotesers primærstabilitet

Total hip arthroplasty is among the most successful surgical operations carried out over the last decades. With this procedure the orthopedic surgeon replaces the hip with a prosthesis. The lower part of the prosthesis is impacted into the femoral canal in case of cementless prostheses. The body weight is then transferred through the prosthesis into the femur in a gradual manner. Although being a successful procedure, in some cases loosening of the prosthesis stem occurs. One reason for this is the (lack of) primary stability of the stem inside the femoral canal. Over time the bone merges with the stem, denoted osseointegration. This process of bone remodeling depends significantly on the relative motion between the prosthesis and bone, i.e. extent of micromotion. Hence, the contact pressure, surface condition, elasticities of bone and stem material etc are important parameters for primary stability of the prosthesis. The thesis addresses some of these aspects.

Scope:
The project addresses finite element modeling of femur and prosthesis stem and simulation of their interaction when subjected to static and cyclic loads from typical daily activities (gait and stairclimbing). Different friction models should be considered. The effect of contact pressure on friction properties should be discussed. If time allows, some recent nonlinear friction models determined from tests can be implemented as a user subroutine in ABAQUS. The effect of different friction models on micromotion/primary stability should be discussed.

Supervisors: Prof. Bjørn Skallerud

The report should be written according to current guidelines and submitted to the Department of Structural Engineering, NTNU, by 11 June 2012.

Abstract

Since the first Total Hip Arthroplasty (THA) performed in the 60's, it has been regarded among the most successful surgical procedures. When an un-cemented hip prosthesis is employed, the prosthesis is impacted into a prepared cavity in the femur. This surgical technique is known as impact bone grafting and is commonly used in THA. The stability of the prosthesis immediately after surgery is denoted primary stability.

Numerical analyses of primary stability, often assume the forces applied during impact grafting to be lower than those present during routine activity. The magnitude of the forces applied during impact grafting is regarded a point of uncertainty, questioning this assumption. As the forces applied during impact grafting are equalized by frictional and contact forces, frictional characteristics present between prosthesis and femur could influence the primary stability of the prosthesis. The influence of grafting force magnitude and frictional characteristics on primary stability is investigated in this thesis.

A study of scientific publications on primary stability was performed, forming the basis for the further analyses. External loads, mechanical properties and recommended practice with regard to numerical analysis of THA, were based on findings from this literature study.

The performed analyses are purely numerical, using state of the art finite element software. The numerical model's response is verified, but as no experimental results are available on the particular geometry, validation is difficult. Two parametric studies were performed, investigating the influence of the impaction force magnitude and friction characteristics on micro motion.

The friction coefficient was found to influence the primary stability of the prosthesis. An intermediate friction coefficient yielded the highest stability, with the same loads applied in all cases. Based on this finding, the influence of prosthesis-bone interface lubrication was investigated. A preliminary reduced friction coefficient during impact grafting yielded an enhanced primary stability, motivating further investigation of the concept.

The magnitude of the impaction force was found to influence the primary stability of the prosthesis. An increased force magnitude above 240% of the patient bodyweight yielded an enhanced primary stability. This finding motivates a further investigation of the force magnitudes present during surgery.

In order to extend the numerical model to include non-linear friction characteristics, a subroutine is proposed. The friction model's behavior is verified in this thesis, but further implementation is required.

Sammendrag

Den første Total Hip Arthroplasty(THA) operasjonen ble gjennomført på 60-tallet og denne typen kirurgi har siden da blitt ansett som en av de mest suksessfulle. Ved bruk av usementerte proteser, bankes protesen inn i femur. Denne kirurgiske teknikken er kjent som "bone impact grafting". Stabiliteten som oppnås umiddelbart etter kirurgi er kjent som primærstabilitet.

Når primærstabilitet undersøkes ved bruk av numeriske modeller, antas det ofte at kreftene påført under kirurgi er mindre enn de som påføres under daglig aktivitet. Hvor store kreftene er under kirurgi, ansees som et usikkerhetsmoment. Dette setter spørsmåltegn ved denne antagelsen. Kraften som påføres for å banke protesen inn i femuren motvirkes av kontaktkrefter of friksjonskrefter. Friksjonens innvirkning på primærstabilitet er derfor en faktor som undersøkes i denne masteroppgaven.

Nødvendig kunnskap om faktorer som innvirker på primærstabilitet ble tilegnet gjennom et litteraturstudie. Det ble i litteraturstudiet lagt spesielt vekt på eksterne laster og mekaniske egenskaper samt anbefalt praksis for numerisk analyse av THA.

Analysene gjort i denne masteroppgaven er rent numeriske og baserer seg på elementmetode-programvare. I mangel av eksperimentelle data, er modellenes oppførsel kun verifisert.

I denne masteroppgaven ble det gjort to studier. Det første studiet undersøker friksjonskoeffisientens innvirkning på primærstabilitet. Dette ble undersøkt i form av et parameterstudium. Parameterstudiet avdekket at en middels friksjonskoeffisient ga den høyeste primærstabiliteten. Konsekvensen av midlertidig redusert friksjonskoeffisient under kirurgi ble så undersøkt. En midlertidig redusert friksjonskoeffisient ga en økt primærstabilitet. Dette motiverer videre undersøkelse av denne teknikkens potensiale.

Det andre studiet undersøker koblingen mellom kreftene påført under kirurgi og primærstabilitet. Krefter større enn ved gange ga en økt primærstabilitet. Dette motiverer videre undersøkelse av kreftene som påføres under kirurgi, ettersom disse potensielt innvirker på primærstabilitet.

Ettersom den brukte elementmetode-programvaren ikke tilbyr ulineære friksjonsmodeller, er det her utviklet en subrutine. Denne subrutinen er verifisert, men trenger videre implementering før den tas i bruk.

Preface

The following master thesis is done in the 10^{th} semester of my master degree in Mechanical Engineering at the Norwegian University of Science and Technology (NTNU). The thesis is weighted 30 ECTS, counting for 100% of the workload in this semester. The work was started January 2012 and ended June 2012.

This study is motivated by personal relations and experience with the possible complications associated with total hip arthroplasty. The use of numerical tools on biomechanical problems has long been a field of interest, and I am grateful that I have been given the opportunity to work on this field.

The assignment was defined in collaboration with professor Bjørn Skallerud. I would like to thank him for valuable guidance and discussion throughout my work. I would also like to thank Dr.Med Olav A. Foss for valuable discussion and the introduction of practical experience into my work. My co student Vegard Martinsen has also been a valuable partner for discussion and motivation throughout my work. I would also thank my girlfriend MSc. Sigrid R. Vatne and her sister PhD. Inga R. Vatne for feedback on my work.

Trondheim 11.06.2012

Sindre Nordmark Olufsen

Contents

List of Figures

Nomenclature

BW	Body Weight
THA	Total Hip Arthroplasty
C	Contact stiffness parameter
$\{C_{EP}\}$	Tangent stiffness matrix
$c(u)$	Constraint equation
$\{D_{n+1}\}$	Displacement increment vector
$\{D^e_{n+1}\}$	Elastic displacement vector
$\{D^P_{n+1}\}$	Plastic displacement vector
$\{E\}$	Material stiffness matrix
E	Material stiffness parameter
E_i	Material stiffness in direction i
F	Force
F_i	Force component in direction i
f	Yield condition
f^{trial}_{n+1}	Value of the slip condition, using trial stresses
G_{xy}	Material shear stiffness
$G(\alpha)$	Hardening function
g_n	Slave-master inter-penetration
g_T	Slave-master relative tangential movement
h	Gap opening variable
K	Linear stiffness of the non-linear friction model
K_1	Parameter used in the Voce-rule
K_2	Parameter used in the Voce-rule
LM	Parameter defining a slip or stick state
M	Moment

M_i	Moment arround axis i
P	Contact pressure
P_C	Pressure coefficient
$\boldsymbol{R}(u)$	Stress divergence tensor
R	Term used in the Newton Rapson scheme
$\{S_{n+1}\}$	Vector containing normalized stress increment components
u_i	Displacement field component i
α	The plastic parameter
ε_y	Yield strain
ε_u	Ultimate tensile strain
γ	The consistency parameter
μ	Static friction coefficient
μ_K	Kinematic friction coefficient
ν_{ij}	Poisons ratio between system i and j
Π	Potential energy
σ_y	Yield stress
σ_u	Ultimate tensile stress
σ_{ij}	Stress component ij of the stress tensor
$\{\tau_{n+1}\}$	Updated stress vector
$\{\tau_{n+1}^{trial}\}$	Trial stress vector
τ_y	Slip shear stress

1 Introduction

Diseases causing joint trauma, could significantly reduce the individual's quality of life. A mean to increase these individual's quality of life is to restore the functionality of the joint with the use of joint implants. In the case of hip trauma, this is done using a hip prosthesis.

Extensive surgery is required in order to mount a hip prosthesis and considerable strain is inflicted on the patient. For the patient receiving this kind of surgery, the longevity of the surgery is therefore important. The longevity is influenced by a range of factors, and the most central factors are introduced in this thesis.

There are two main classes of hip prostheses in use today, being un-cemented and cemented prostheses. The cemented designs are inserted into the human femur surrounded by a layer of cement. This layer acts as a bounding compound between the prosthesis and the bone. Due to their increasing popularity, un-cemented prostheses are the point of focus in this thesis. The un-cemented prostheses are pressed into the femur with no additional material between the prosthesis and the bone. As no cement is used to constrain the prosthesis, the ingrowth of bone into the prosthesis surface is the main mechanism constraining the prosthesis. This bone ingrowth is denoted osseointegration and is a process requiring limited movement in the prosthesis-bone interface. The consequence of excessive relative movement between the prosthesis and the femur, is the formation of fibrous bone tissue instead of successful osseointegration, reducing the longevity of the surgery. The stability of the implant prior to osseointegration is denoted primary stability.

The relative movement between the prosthesis and bone due to external loads is denoted micro motion. Micro motion has been a point of research since the first un-cemented designs was taken into commercial use. The investigations range from in-vivo animal studies to purely numerical studies using numerical tools as the finite element method. Several of the findings from the investigations deviate both qualitatively and quantitatively. It has been highlighted that the assumptions made on external loads, constraints and geometry has a large impact on the obtained results.

In this thesis the assumptions made for the interaction between prosthesis and bone are investigated. The parameters used to describe the characteristics of prosthesis-bone friction have been found to deviate between several of the scientific publications available. The impact of this inconsistency is the main point of focus in this numerical study.

The technique used to implant an un-cemented hip prosthesis is known as impact bone grafting. This technique uses a hammer to apply force on the prosthesis, in order to press it into the prepared cavity of the femur. Numerical analyses available in the literature regarding primary stability of un-cemented hip prostheses, assume that the forces used under grafting are lower than the

longitudinal forces present during gait. There is a limited amount of experimental results confirming this assumption and the influence of the assumption is studied in the thesis.

In order to develop a numerical model able to reproduce the phenomena of interest, an extensive study of scientific publications on primary stability were done. In order to produce a conservative estimate of primary stability, literature regarding femoral loads due to routine activities was emphasized. The most central findings of this literature study is presented in this thesis.

As numerical tools were employed to investigate the interaction between a un-cemented prosthesis and femoral bone, an understanding of the phenomena of friction and contact was considered important. A basic understanding of contact was obtained through finite element courses, and the main aspects are presented in this thesis. Friction is discussed both as phenomenon and as subject of mathematical analysis using continuum theory. Wear is closely related to friction and is also introduced.

The lack of experimental validation does reduce the credibility of this study. The numerical model is not validated, but the purely numerical aspects are investigated and the models response verified.

The finite element software employed in this thesis did only allow for Coloumb friction characteristics. The non-linear frictional response found by Shirazi-Adl et al. (1993) was a point of interest in this study and a subroutine is proposed.

2 Total Hip Arthroplasty

2.1 General

People suffering from different forms of arthritis and other diseases causing hip joint trauma are possible candidates for total hip arthroplasty (THA). THA is a surgery where the femoral head and neck region is removed from the femur, a cavity in the femur prepared, and a prosthesis introduced into the cavity.

THA is considered a highly successful type of surgery with only 10% revisions within 15years (Malchau et al. (1993)). However for the patients receiving this kind of surgery, complications and further revision surgery can significantly reduce the patient's quality of life.

The reasons for revision surgery are greatly dominated by aseptic loosening making approximately 80% of all revisions (Malchau et al. (1993)). Aseptic loosening is a detachment of the prosthesis from the bone or cement interface, causing excessive movement and pain for the patient. The reasons for aseptic loosening are many and complex, also varying between cemented and un-cemented prostheses. In this study the main emphasis will be on un-cemented prostheses. Several factors found to contribute to aseptic loosening are discussed in section 2.2.

Figure 1: Illustration of THA. Capture from (*Information for Patients of Total Hip Replacement, or Total Hip Arthroplasty (THA)* (02.06.2012))

When a un-cemented prosthesis is introduced into the prepared femoral canal, the prosthesis is knocked into the canal using a hammer. This technique is called impact grafting and has shown great surgical success.

The impaction force applied under surgery is determined by the surgeon performing the surgery, which allows for large deviations between individuals. The commonly used surgical technique is to increase the force and prosthesis

size until the fixation of the prosthesis is considered sufficient. The force used to obtain this fixation may be large enough to cause femoral failure, and failure rates of 16% have been reported (Cummins et al. (2011)).

The stability achieved immediately after surgery is called primary stability and is thought to have a large influence on the rate of osseointegration (Soballe (1992)). Osseointegration is the ingrowth of bone tissue into the surface of the hip prosthesis, and is considered a major fixation mechanism of the prosthesis (Soballe (1992)). If the primary stability is insufficient, excessive motion in the prosthesis-bone interface is observed, inhibiting successful bone ingrowth. Lack of primary stability and excessive micro motion has been reported to cause formation of a fibrous layer in the periphery of the prosthesis, increasing the micro motion further (Soballe (1992), Waide et al. (2004)).

The time after surgery is dominated by healing of the surgical wounds, osseointegration and of a relatively low level of activity. The patients level of activity does vary greatly between individuals as well as between hospital practices. After surgery, the bone is in a adaptive state adjusting to the new loading state. This adaptation is observed as bone growth as well as local changes in bone density and stiffness (Orleans (1976)).

2.2 Reasons for Aseptic Loosening

Aseptic loosening is a term commonly used for loosening in the prosthesis-prosthesis interface. This loosening allows for excessive movement, causing pain for the patient.

Through the years since the first commercial total hip arthroplasty, there have been many theories around the phenomenon of aseptic loosening. Several of the theories has caused significant change in prosthesis design, both with regard to geometry and material usage (Mjoberg (1994), Sundfeldt et al. (2006)).

The dominant theories of the present is: inflammatory reaction caused by wear particles, excessive micro motion with a subsequent fibrous layer formation and the phenomenon of stress shielding (Sundfeldt et al. (2006)). The theories are briefly introduced in the following sections.

2.2.1 Particle Disease

The presence of cement wear particles in the prosthesis-cement interface observed under revision surgery formed the basis for the theory of particles disease (Mjoberg (1994)). The particles trigger an immunoinflamatory reaction, which is thought to cause aseptic loosening.

The theory of particle disease motivated the development of un-cemented prostheses, avoiding the use of cement in the surgery and thereby avoiding

formation of cement debris. However, even with the use of un-cemented prostheses, immunoinflamatory reactions are observed. The particles now found in the prosthesis interface is now mainly wear particles from the acetabular cup (Gilbert & Jacobs (1994)).

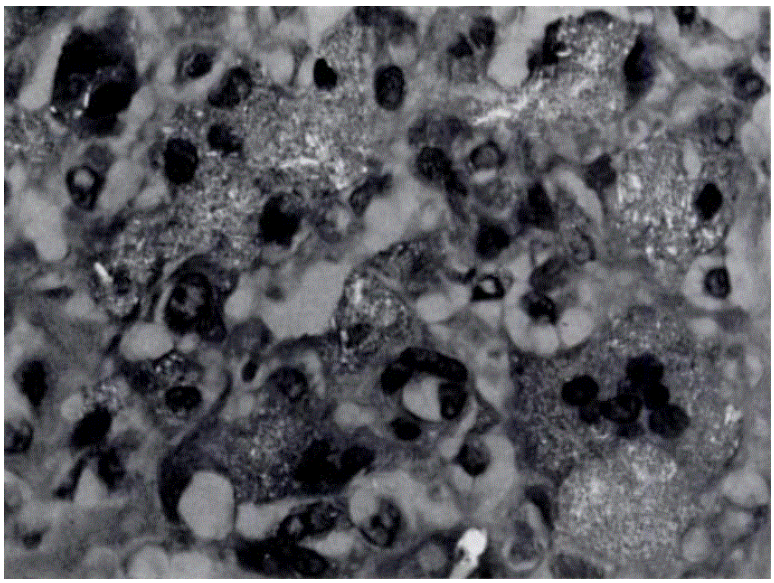

Figure 2: Photomicrograph of wear particles (Black) in the interfacial membrane. Taken from Gilbert & Jacobs (1994)

2.2.2 Micro Motion and Fibrous Tissue Formation

The initial fixation of the prosthesis has been found to be a good indicator of surgical success (Sundfeldt et al. (2006), Soballe (1992)). When the surgery is done there is only a partial contact between the prosthesis and femoral bone, and an even smaller contact surface with cortical bone. The rest of the contact surface is in contact with materials such as marrow and blood, having a reduced load carrying capacity.

The lack of full fixation may allow for movement of the stem relative to the femoral canal. This movement is thought to cause immunoinflamatory reactions at the bone-prosthesis interface, often triggered by ion release or debris formation. This relative movement is called micro motion and has shown good correlation with the degree of osseointegration (Soballe (1992)). The exact limits acceptable for successful osseointegration shows large deviations in the literature, but 30-150 micrometer is considered an upper bound (Götze et al. (2002)).

If the micro motion is increased further, a fibrous layer lining the stem may be observed. This fibrous layer then allows for an increased movement from daily loads due to its lower stiffness and strength (Waide et al. (2004)).

As the presence of a fibrous layers around the prosthesis or cement interfaces has been shown to have a significant negative effect on the longevity of the surgery, there is a strive to avoid this phenomenon. It has however been indicated that the avoidance of such a layer is difficult. The connection between micro motion and a fibrous lining of the stem has been investigated by several authors, indicating the presence of such a layer yields unacceptable degrees of micro motion even for layer thicknesses hard to detect with conventional roentgenographic technique (Waide et al. (2004)).

The investigation done by Waide et al. (2004), using both in vitro experiments as well as numerical models, indicated that fibrous layer thicknesses of less than 500 micrometer could yield micro motion exceeding 200micrometer, which has been indicated as more than acceptable for successful osseointegration and bone ingrowth.

2.2.3 Peripheral Fluid Pressure

There are several theories concerning the formation and consequence of fibrous layers in the prosthesis periphery. Fluid flow in the fibrous layer was investigated by Vis et al. (1999), observing a correlation between the increased fluid pressure against the cortical bone due to fibrous layer compression, and loosening. This was found to cause bone resorption and a subsequent aseptic loosening on rabbit femurs. This compression of fibrous bone is assumed to be due to micro movement of the prosthesis relative to the femoral canal. The increased pressure has been found to cause bone devitalization and subsequently, bone resorption (Scand (1998); Mjoberg (1994)). The investigation by Vis et al. (1999) showed that a fluid pressure exceeding 70-150 mm Hg caused osteocyte death and a forming of fibrous tissue in the interface.

2.2.4 Stress Shielding

The bone's adaptive mechanism to mechanical loading has been a field of interest for many authors. The bone adapts to the altered load field after surgery, with both formation of new bone (modeling), and rebuilding of existing tissue (remodeling). Bone modeling and remodeling could cause changes in bone geometry, bone density, stiffness and strength (Orleans (1976)).

The adaptive response of the bone to the altered load-field has shown to cause load redistribution (Huiskes et al. (1986)). Bone resorption is often found proximally, causing a reduced load carrying capacity in the proximal end of the prosthesis. A more in depth review of the mechanisms governing bone remodeling and work done on the field is found in the literature study by Olufsen (2011).

2.3 The Human Femur

The human skeleton is formed by a large number of bones, varying in shape and mechanical properties. The human femur commonly called a hip-bone or thigh-bone, is the largest bone in the human skeleton and is subjected large loads exceeding 240% of the human bodyweight even at routine activities (Bergmann et al. (2001)).

Figure 3: Illustration of human femur. Femoral head (Red), femoral neck (Blue), Greater Trochanter (Green), Lesser Trochanter (Yellow) and outer and inner Condyles (Purple)

The human femur is divided in several regions, being the femoral head, neck, greater trochanter, lesser trochanter, shaft and condyles. The femoral head and neck, located at the proximal medial end of the femoral shaft is illustrated in figure 3. The femoral head is the point of contact between the femur and the acetabulum acting as a rotational link between the pelvis and the lower extremities.

The greater trochanter is located at the proximal lateral end of the femur and is acting as a point of contact for a large number of muscles such as the gluteus medius and minius.

The lesser trochanter is located below the femoral neck, being a point of connection for the muscle psoas major. The midsection of the femur is called the femoral shaft and at the distal end of the femur we find the outer and inner condyles.

Depending on location, the type of bone varies. The human femur mainly consists of two types of bone, being cortical (dense) bone and trabecular (spongious) bone. The parts of the femur dominated by uniaxial loading shows a tendency to form cortical bone whereas the locations exposed to a more triaxial loading is dominated by trabecular bone formation.

The femoral shaft consists of a core of trabecular bone surrounded by thick layer of cortical bone as illustrated in figure 4. The greater trochanter and head region mostly consist of trabecular bone but also here surrounded by a layer of cortical bone forming the outer-surface. The mechanical properties of the

Figure 4: Roentgenographic image of proximal end of human femur. Caption taken from Porrino et al. (2010)

different classes of bone is further discussed in chapter 7.1.

3 Primary Stability

The stability of the prosthesis obtained immediately after surgery has been found to have a large impact on the longevity of the surgery. Factors influencing this stability have been investigated by several authors, both experimentally and analytically. Findings from several studies available through scientific publications regarding primary stability are here introduced. This is done to gain an overview of the phenomena involved and the methods used to investigate these.

3.1 General

Primary stability is the prosthesis stability obtained directly after surgery and is found to be a product of several factors such as bone quality, prosthesis shape and fit of the prosthesis in the reamed cavity.

The main mechanism connecting the bone and prosthesis prior to osseointegration is friction acting in the prosthesis-bone interface. The frictional forces are influenced by contact pressure and surface tribology[1], making primary stability a complex phenomenon. The contact pressure between the femur and proshesis is obtained under surgery as described in section 4, and additionally during physical activity.

To illustrate the role of the different force components present after THA, a simplified model is presented:

The prosthesis position in the reamed cavity is symbolized by a wedge shaped plug pressed into a wedge shaped cavity. When a longitudinal force is applied at the top of the plug, reaction forces are present in the interface between the geometries. The longitudinal component of the contact force, $F_{N(L)}$, and the longitudinal component of the frictional force $F_{N(L)}$ are the two reaction forces counteracting the longitudinal force. The frictional force is commonly assumed to be a function of the contact pressure F_N, giving a non-linear response. The phenomenon of friction is further discussed in section 6.

When the axial loading is removed, the axial component of the contact pressure is equalized by the frictional force. This would imply that the highest frictional force is obtained with the highest contact pressure possible. Based on this reasoning, it is assumed that a higher contact pressure is beneficial for obtaining the highest possible stability of the prosthesis, coinciding with the findings of Abdul-Kadir et al. (2008).

[1] Def: The science of the mechanisms of friction, lubrication, and wear of interacting surfaces that are in relative motion

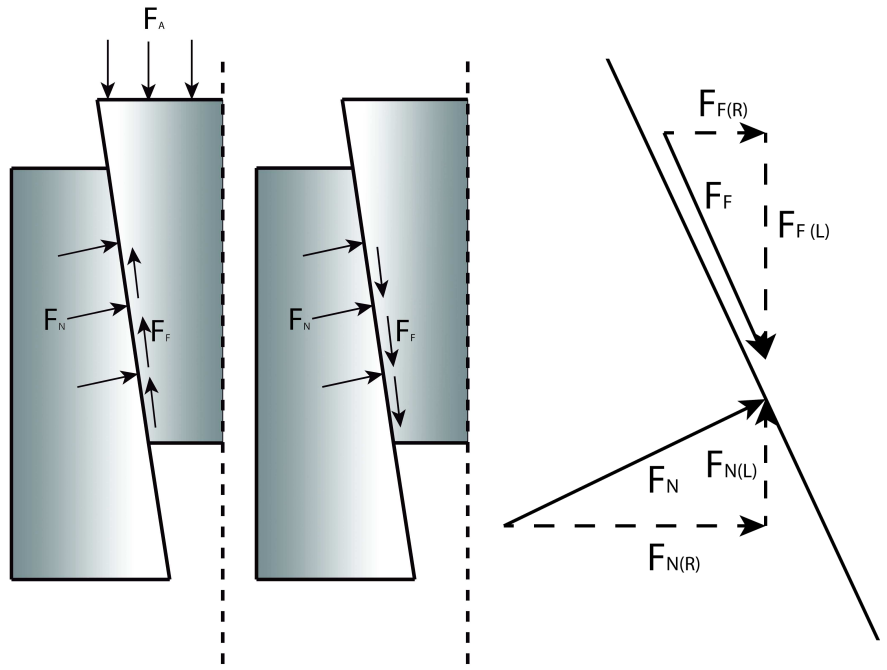

5a: With external load

5b: Unloaded

5c: Force decomposition

Figure 5: Simplified forcefield. Axial force F_A, contact pressure F_N and frictional force F_F. The components in the longitudinal direction are denoted with (L) and radial components are denoted with (R)

3.1.1 Micro Motion

Micro motion is, as introduced in section 2.2.2, a measure of prosthesis primary stability. Micro motion is connected to relative relative motion in the prosthesis-bone interface. This relative displacement is divided into an elastic and a plastic part. The plastic part is here defined as the part of the displacement leaving a residual after the loading is removed. The longitudinal component of the plastic displacement is denoted subsidence, and is a measure used in the determination of implant stability after surgery.

In this study, interface micro motion is the factor of primary interest, and is defined as the difference in relative displacement in the prosthesis-bone interface, at maximum loading and at the unloaded state, see figure 6.

3.2 Findings from Available Literature

There is a large amount of scientific publications available on primary stability. The investigations deviate both in complexity and nature, ranging from in vivo[2]

[2]Def: In the living organism.

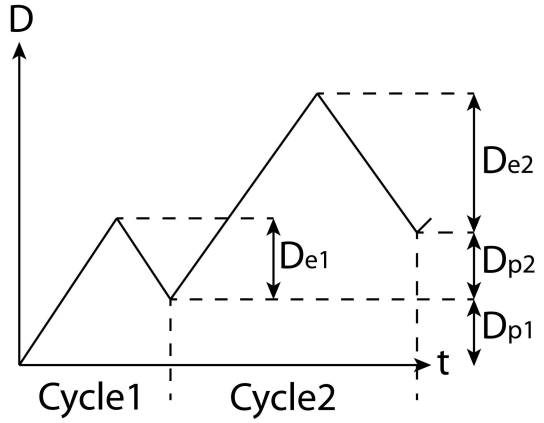

Figure 6: Interface displacement(D) under two load cycles, decomposed into a elastic(D_e) and a plastic(D_p) part, cycle number is denoted with 1 and 2

experiments to purely numerical studies. In order to gain an understanding and overview of the phenomenon of primary stability, several findings from the literature is here presented. Special emphasis is put on the work by Abdul-Kadir et al. (2008), due to its similarity to analyses presented later in this thesis.

3.2.1 Experimental Determination of In Vivo Conditions

Factors influencing primary stability of hip prostheses has been investigated in vitro[3] by several authors. Several of the investigations done deviate in test protocol both with regards to test setup and loads applied. The in vitro studies deviate also with regard to reference system used to describe the relative motion at the prosthesis interface (Monti et al. (1999)). Combined with the differences in applied loads, constraints and geometry direct comparison is difficult.

In order to experimentally and analytically produce conservative estimates of primary stability, the most critical in vivo loads have to be employed. The femoral loads under different daily activities has been determined through in vivo experimental studies, and findings are presented in section 7.3.

The most critical loads with regard to prosthesis loosening and excessive micro motion is caused by torsional loads, typically from stair climbing (Kassi et al. (2005)). Load fields corresponding to stair climbing is therefore often used in studies on interface micro motion.

When an in vitro investigation of primary stability is done, the in vivo load field is to be replicated. A setup used in several studies simplify the external loads to a joint contact force acting at the femoral head, neglecting the effect of muscle forces acting on the femur (Götze et al. (2002)). This neglecting of

[3]Def: In an artificial environment, such as a test tube

muscle loads is a simplification which could underestimate the micro motion due to excessive bending of the femoral shaft(Duda et al. (1998)).

When the human hip joint is loaded during daily activities, it is over constrained by the joint, muscles and ligaments. This complex load and constraint scenario is considered hard to reproduce. A recommended practise is to use the minimum number of constraints necessary to avoid bending motion of the bone and thereby coupling through highly unpredictable force transfers (Monti et al. (1999)).

A simplified load field is proposed by Heller et al. (2005) and discussed in section 7.3.2. The proposed setup has been used in studies as by Kassi et al. (2005) which emphasize the importance of muscle forces in micro motion analyses. The work of Kassi et al. (2005) concluded that the neglection of the muscle forces underestimate micro motion and thereby overestimate the prosthesis primary stability.

3.2.2 The Influence of Interface Conditions

The numerical investigation of a femoral hip implant is regarded a highly complex analysis, often including both constraint and material non-linearities. The prosthesis-bone interaction is often of high interest due to phenomena such as interface micro motion, and contact is therefore often incorporated in the analyses. The contact interface modeling introduces a range of variables, some experimentally determinable, some of a purely numerical nature, see section 7.4. The importance of validation with experimental results has been emphasized, as by Bernakiewicz & Viceconti (2002).

Several numerical analyses of stem-femur interaction have been performed, and various interface conditions in the prosthesis-bone interface have been assumed. Commonly used interface conditions are: stick, Coloumb friction, non-linear Coloumb friction and slip (Mann et al. (1995), Kuiper & Huiskes (1996*a*)).

The interface conditions mimic different interface scenarios. The influence of the different boundary conditions on bone loading and interface stress field, has been a subject of interest for several authors. Findings indicate that the assumed interface conditions has a strong correlation with both the qualitative as well as quantitative nature of the stress-fields and loadings (Kuiper & Huiskes (1996*a*), Mann et al. (1995)).

The analysis by Kuiper & Huiskes (1996*b*) investigated the influence of the Coloumb friction coefficient and material stiffness mismatch, on interface micro motion. The findings indicated that the frictional coefficient has a large impact on interface micro motion, however with decreasing impact for frictional coefficients above 0.15.

The influence of linear friction-displacement characteristics on micro motion, has been investigated with the use of numerical tools. The work of Mann

et al. (1995) implemented a linear friction model, having a linear increase towards a displacement of saturation. Their findings were compared to a stick condition, showing substantial changes both with regards to interface stress magnitudes, but also the qualitative shape of the interface stress fields. The friction model by Mann et al. (1995) has certain similarities to the frictional response determined by Shirazi-Adl et al. (1993). The frictional response found by Shirazi-Adl et al. (1993) does however exhibit a non-linear response, further discussed in section 13

When doing fatigue analysis of stem-femur interface material, the stresses behavior in time is of high importance. In a typical loading estimated from walking or climbing a stair, the head contact forces does not pass through zero (Bergmann et al. (2001)).However, finite element analysis assuming a zero loading when the foot is lifted has been done, and gives interesting results.

A numerical analysis on prosthesis-bone interface fatigue was done by Mann et al. (1995), assuming a full-stick or a friction free interface. Both interface conditions yielded a total relaxation of the interface stresses as the load was removed. However, an interface condition including friction was found to yield a non-zero stress in the same load free state. This was found to be due to a sticking of the interface before the load is totally removed, causing a stored stress in the interface. This was caused by the constrained movement of the stem relative to the femur. This was found to have a significant impact on the longevity of the interface material. The resulting lifespan from the analysis including interface friction was less than what was considered acceptable.

3.2.3 The Consequence of Geometrical Inaccuracies

The fit of the prosthesis in the reamed femur influences the contact pressure field around the prosthesis (Abdul-Kadir et al. (2008)).

As the femur is prepared for the prosthesis, the shape and dimension of the reamed cavity may deviate from the shape and dimension of the prosthesis. The reamed cavity is often assumed to be smaller than the prosthesis dimensions, causing a pressure between the prosthesis and the femoral canal.

Reaming tools used in THA surgery today, deviate in their function (Olav (2012)). Some of the reaming tools mainly compress bone tissue whereas others mainly remove bone tissue.

The investigation done by Abdul-Kadir et al. (2008) showed that the interface micro motion is greatly reduced as the femoral canal dimension is reduced relative to the prosthesis, causing an increased contact pressure. Abdul-Kadir et al. (2008) highlighted that interference fit is a point of high uncertainty. In his analysis interference fit was determined using back-modeling against experimental data, and the obtained interference value was far less than given by the suppliers of the prosthesis. The numerically obtained micro motion values spanned from 150 microns to 2 microns, with the interference as the only

variable in the model.

The interference can only be increased to a degree where the stresses in the femur do not exceed its fracture limits. A threshold interference fit of 100 microns has been suggested by Shultz et al. (2006), as it was found to cause interface damage due to high interface stresses.

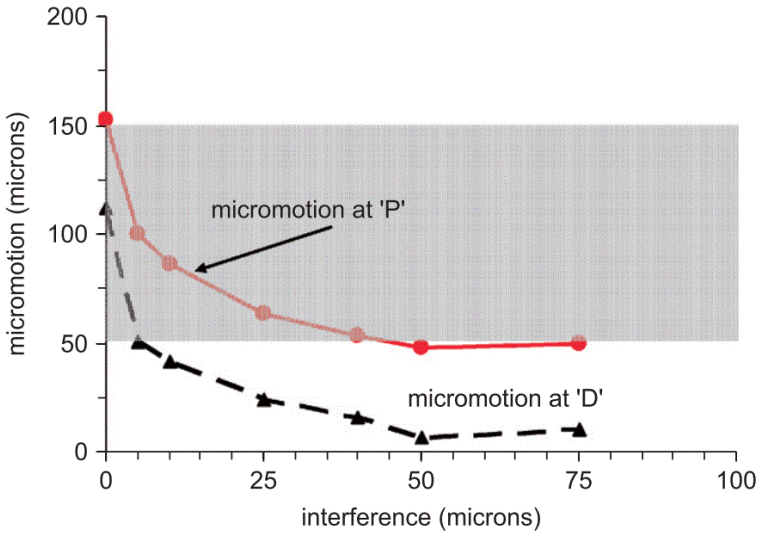

Figure 7: Micromotion as a function of intereference fit, as found by Abdul-Kadir et al. (2008). P denotes a proximal sampling point, D denotes a distal sampling point. Grey zone indicates unacceptable micromotion for osseointegration. Location of sampling points described by Abdul-Kadir et al. (2008)

Another factor having significant impact on interface micro motion and thereby primary stability, is the presence of a lateral gap after insertion of the prosthesis (Park et al. (2008)). The reaming of the prosthesis cavity often leaves a lateral gap at the proximal end of the prosthesis. This gap reduces the contact surface, inhibits bone ingrowth in the gap, and could also be a site for infiltration of wear particle from the acetabular cup. The reduced contact surface was found to correlate with increased micro motion, and a reamer design proposal was made in order to avoid this gap.

The fit of the prosthesis in the bone is a point of difficulty as the cortical wall thickness and curvatures of metaphysis may deviate. Götze et al. (2002) investigated the influence of a custom prosthesis based on CT-images from a donor femur with a conventional prosthesis design. The improved fit of the prosthesis was found to generally decrease interface micro motions, but did actually increase the medial-lateral translation of the prosthesis.

3.2.4 Summary

As a summary of the above mentioned studies, their findings with regard to interface micro motion are summarized in table 3.2.4. The findings does deviate in both experimental setup and in investigated parameters, but gives an indication of the range of micro motion commonly found both experimentally and numerically.

Predictions of micro motion $[microns]$			EXP.		FEM	
Author	μ $[-]$	Load	Dist.	Prox.	Dist.	Prox.
Park et al. (2008)	0.5	H,w	10±4	12±6	10±3	22±7
Park et al. (2008)	0.5	H,s	25±7	16±7	14±4	26±12
Abdul-Kadir et al. (2008)	N-L	M,H,s	18±2	19±5	2-150	2-150
Kassi et al. (2005)		H,s		50		
Kuiper & Huiskes (1996*b*)	0.4	H,self			13	4
Götze et al. (2002)		H,self	8±9	37±27		
Monti et al. (1999)		several				

Table 1: Loads are defined as Head(H) and or Muscles(M). The loadings are either Walking(W) or Stair climbing(S) equivalent as found by Heller et al. (2005) and Bergmann et al. (2001). Additionally self-defined loadings have been used(self). All micro motion values are given in microns. Micro motion sampled are given proximally (Prox) and distally (dist)

4 Surgical Technique and Bone Impact Grafting

4.1 General

The surgical techniques used in the implementation of hip prostheses are of interest in this study due to their possible influence on primary stability. The surgical technique for a cemented and an uncemented prosthesis are similar, deviating mainly in the size of the reamed cavity.

The main steps of total hip arthroplasty are presented and briefly discussed in order to better understand the possible influence of the surgical technique on the primary stability of the prosthesis.

4.2 The Surgical Procedure

The recommended practise used in implementing a press fit hip prosthesis is supplied to the surgeons who perform the surgery from the supplier of the prosthesis. An outline of the surgical procedure is here presented based on the recommended technique provided by Gladiator, to clarify the most relevant steps of the surgery.

The procedure begins with an evaluation of the patient's discrepancy between femurs, this to allow for early accountancy of leg length differences etc. The roentgenographic anterior-posterior views are then used to determine an initial prosthesis size, based on both metaphyseal and diaphyseal fit. This is done through a comparison of the patient's endocortical canal shape, and templates of the prosthesis provided to the surgeon. The neck length and angles are then estimated based on the roentgenograpic images.

Figure 8: Head cut with 45° angle relative to longditudional axis. Caption from Wright (2010)

The femoral head is then cut with a 45° angle relative to the longditudional axis of the bone, using the bottom of the great trochanter as reference for the cut, see figure 8.

The now freed surface of the proximal femur is prepared for reaming using a box-chisel pressed laterally, to ensure the correct orientation of the prosthesis. The femoral shaft is then reamed using a longer slender reamer to remove the bulk material of the cavity into which the prosthesis is to be pressed, as illustrated in figure 9.

Figure 9: Preparation of the femoral canal using a box chisel(Left) and a slender reamer(Right). Caption from Wright (2010)

After the reaming process, the canal is expanded to the dimensions of the prosthesis. This is done using a broach corresponding to the prosthesis dimension, as illustrated in figure 10.

Figure 10: Preparation of the femoral cavity using a broach. Caption from Wright (2010)

This broaching procedure is done with increasing broach size until an increased resistance is noted. This increase in resistance is due to lateral and medial cortical bone contact. The broach is then used for trial reduction[4] to determine if the primary stability is satisfactory. This judgment is based on the surgeon's experience, and may deviate between surgeons.

If the fit of the broach is considered satisfactory, the broach is removed and the corresponding prosthesis is implanted. This is done through the attachment of a handle to the neck region of the prosthesis and then applying force, typically with the use of a surgical hammer, as illustrated in figure 11. A final trial-reduction is then done.

4.3 Impact Grafting and femoral Fracture

In order to obtain a primary stability sufficient for osseointergration, a significant contact pressure is needed between the bone and prosthesis (Abdul-Kadir et al. (2008)). The surgical technique used to obtain this contact pressure is often based on the use of impacts. This grafting technique is known as bone impact grafting and has shown great surgical success.

The surgical techniques used for inserting an uncemented prosthesis into a human femur, is performed using impacts and not a continuous force. This is in practice done using a hammer, knocking onto a device coupled to the neck region of the prosthesis, illustrated in figure 11.

This device is used in order to avoid contact between tools and the patient, and to allow for unrestrained movement for the surgeon. The force used to press the prosthesis into the human femur is not exactly defined pre-surgery, as the individual variations between patients and surgical techniques are significant (Cummins et al. (2011)). The prosthesis is then knocked into the femur until the stability of the prosthesis is considered satisfactory and its location is according to initial specifications. However, complications have been observed.

This grafting technique does cause large stresses both transient and stationary in the femur, which may cause fracture of the femur under surgery.

The force necessary to cause femoral fracture has been experimentally investigated by Cummins et al. (2011) using a group of 17 femurs for destructive testing. A threshold value of which no fracture of the femur was found in any specimen was determined, but the deviations between specimens were of almost one order of magnitude. In the test-rig used in the experiment they fully constrained the midsection of the bone, which decreased the longitudinal movement of the bone relative to a surgical situation. From their test setup and their specific prosthesis geometry, a lower bound threshold value for fracture of 0.5KN was found. However, the measured values were considered conservative, due to numerous factors such as reduced material toughness due to formalde-

[4]The application of force in order to test the protshesis stability.

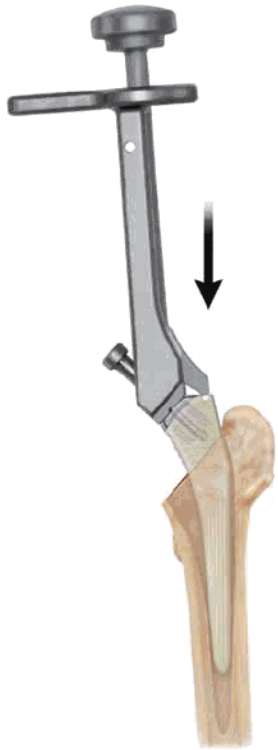

Figure 11: Insertion of prosthesis in the prepared cavity, using a attached tool. Caption from Wright (2010)

hyde storage. A femur which undergoes THA does typically have cortical defects and a significantly reduced bone stock, not evident in their study. Soft peripheral tissue was also removed in the experiments, which is thought to reduce the fracture strength of the bone (Cummins et al. (2011)).

5 Contact Mechanics

Most phenomena found in real life do include some kind of contact between bodies, or self-intersection. Problems including inter body contact, fasteners or couplings, may be treated as contact analyses. Most commercial finite element packages do include algorithms to account for contact, but the exact implementation of the algorithms varies. The modeling of contact does introduce a number of new variables and concepts for the analyst to define. The influence of some of these variables has been investigated by Bernakiewicz & Viceconti (2002), specifically for modeling of prosthesis-bone interaction. The significance of these variables are discussed in section 7.4. In this section, some of the concepts of constraint imposition and contact found in the literature, are presented and discussed.

5.1 The Phenomenon of Contact

As two bodies move in space, their movement may be constrained by boundary conditions. Typical boundary conditions used in analyses are prescribed displacements or velocities, assigned at a point or surface. Suck boundary conditions could be assigned in order to mimic a weld, a bearing or any other physical phenomenon. These boundary conditions are often linear in the sense that they do not change with respect to displacement nor time.

If two bodies move in space and are able to intersect, meaning that they occupy the same point in space at the same time, we observe the phenomenon of contact. To ensure a physically correct behavior, boundary conditions are also here enforced on the bodies.

As two bodies come in contact, a force transfer act between the two bodies depending on their physical state. A more formal description of contact between bodies can be given as by Wriggers (2006):

β^α denotes the body α. The part of the bodies that intersect during an analysis is denoted γ_c, and the position of the bodies at point $\boldsymbol{X_1}$ and $\boldsymbol{X_2}$ are denoted $\psi(\boldsymbol{X_1})$ and $\psi(\boldsymbol{X_2})$. Formally this would imply that two bodies which are in contact has at least one set of points coinciding in time, meaning $\psi(\boldsymbol{X_1}, t) = \psi(\boldsymbol{X_2}, t)$. From this current configuration contact conditions are formulated.

In the search of contact between two bodies, two steps are done to detect whether the bodies contact or not. The first step is to globally identify all points which may come into contact and define possible contact constraints Γ_C. The second step is to define the kinematic conditions needed to determine which contact constraints s that are activated. $s \in \Gamma_a \in \Gamma_C$. In matrix form, the contact constraints are denoted $\boldsymbol{G}^c(u)$. The determination of active contact constraints s are done through the evaluation of the following equation:

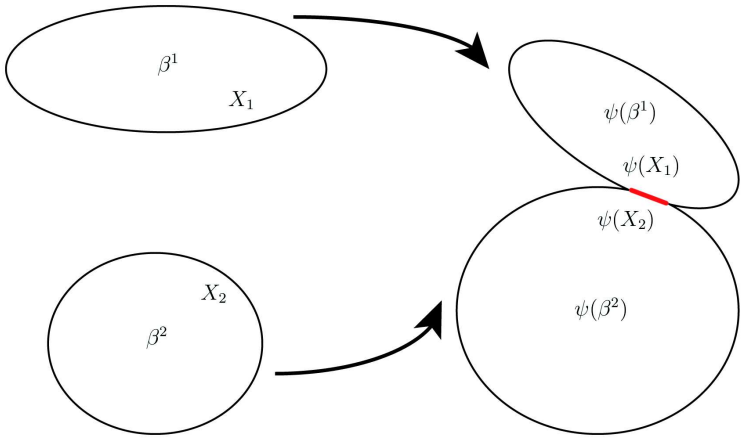

Figure 12: Illustration of bodies before and after displacement

$$\boldsymbol{R}(u) - \boldsymbol{P} = 0 \qquad \text{with} \qquad \boldsymbol{G^c}(u) \geq 0 \tag{1}$$

Here $\boldsymbol{R}(u)$ denotes the stress divergence term as a function of displacement u and $\boldsymbol{P}$ is the load per volume applied. Equation 1 refers to a force equilibrium of a continuum element, and may may for one component be written as:

$$\sigma_{11,1} + \sigma_{12,2} + \sigma_{13,3} - P_1 = 0 \tag{2}$$

Here $\sigma_{11,1}$ is the stress in direction 11 and the comma denotes a differentiation in direction 1. The active constraints determined from the evaluation of equation 1, are then sorted in $\boldsymbol{G^c_s}(u)$.

5.2 Imposing Constraints

In order to enforce a boundary condition upon an equation system, several methods can be used, but share the same basic concept. Imposing constraints is done by augmenting the potential energy Π of the system with additional terms. This augmentation may enforce either linear or nonlinear boundary conditions with the use of several methods. Some of the most common methods are presented here.

5.2.1 The Constraint Equation

In contact problems, a condition for contact between surfaces has to be found. The condition describes the distance between the two surfaces as a function of their displacements, and is zero at the moment of contact. Such a condition may take the following form:

$$c(u) = h - u \geq 0 \tag{3}$$

Here u denotes the displacement, and h the gap size. For $c(u) > 0$ the gap is open, for $c(u) = 0$ the gap i exactly closed.

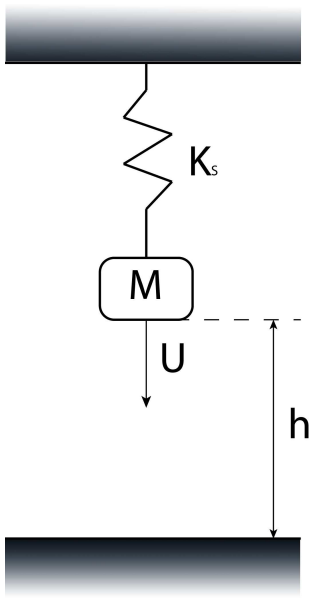

Figure 13: Spring-Mass setup. Spring stiffness K, displacement U, gap size h and mass M

5.2.2 Lagrangean

In order to introduce the contact constraints as described by equation (3) the lagrangean multiplier method may be used. The potential energy of the system is augmented through the addition of the constraint equation (3) multiplied with a constant λ. The potential energy of the spring system illustrated in figure 13 then takes the following form:

$$\Pi(u, \lambda) = \frac{1}{2} k_s u^2 - mgu + \lambda c(u) \tag{4}$$

The potential energy is then made stationary through variation of variables. Differentiation in u and λ direction leads to the following expressions:

$$k_s u \delta u - mg\delta u - \lambda \delta u = 0 \tag{5}$$

$$c(u)\delta\lambda = 0 \tag{6}$$

In the case of contact, $c = 0$ the reaction force is now equal the Lagrangean multiplier λ.

$$\lambda = k_s h - mg = \text{Reaction Force} \tag{7}$$

5.2.3 Penalty Method

Using the penalty method, the potential energy of the system is augmented with the addition of $\frac{1}{2}\alpha c(u)^2$ to the potential energy of the system. Here α denotes the penalty parameter. The potential energy of the system now takes the following form:

$$\Pi(u, \lambda) = \frac{1}{2}ku^2 - mgu + \frac{1}{2}\alpha c(u)^2 \tag{8}$$

Derivation of the potential energy in the displacement direction u gives the following expression:

$$ku\delta u - mg\delta u - \alpha c(u)\delta u = 0 \tag{9}$$

In the case where $\alpha \to \infty \Rightarrow c(u) \to 0$ there is no penetration of the surface, which may be regarded equivalent to the Lagrangean multiplier method.

5.2.4 Practical Differences between Methods

The method chosen to impose constraints may have influence on the end results and efficiency of the analysis (Wriggers (2006)). When using the Lagrangean multiplier method, constraints are imposed exactly. However, the dimension of the equation system is enlarged by the number of constraints imposed, which may lead to increased computational cost.

The penalty method however uses additive terms to impose constraints, which does not increase stiffness matrix dimensions. The penalty method does not impose constraints exactly for $\alpha < \infty$ which would cause surface inter-penetration, and may be non-physical for the problem at hand. In the case of a very large penalty parameter α, an ill conditioned matrix may result.

In software as Abaqus, master and slave surface are common terminology. The master surface is the surface, onto which the constraint is imposed, with the slave surface as a variable in the constraint equation.

The penalty parameter α can be interpreted as a surface stiffness of the slave surface, affecting the degree of overclosure. In the case of normal contact, Abaqus uses the penalty parameter as a contact stiffness C $[N/mm]$. This contact stiffness is constant as illustrated in figure 14. Abaqus also offer the possibility to tabulate a pressure-overclosure relationship, making the analyst able to include non-linear pressure-overclosure relationships. It should be noted that this non-linear pressure-overclosure relation is not implemented in Abaqus

as a penalty parameter, but as a constitutive equation enforced using the Lagrangean method (Simulia (2012)).

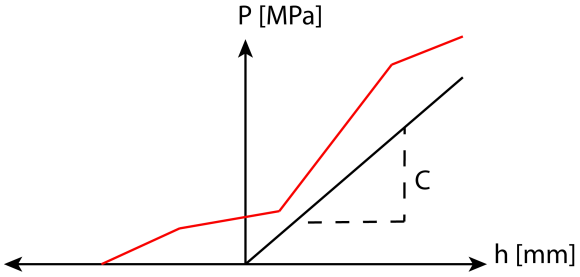

Figure 14: Pressure overclosure relationships. Linear contact stiffness (Black) and tabulated (Red)

5.3 Constitutive Contact Equations

Contact conditions are often of a purely geometrical nature, ignoring micro-mechanical interactions between the surfaces in contact. To account for micro mechanical effects between the surfaces in contact, elastic or elastic-plastic constitutive laws may be calibrated. The constitutive condition between the surfaces describes the interface traction as a function of for example surface displacements. The constitutive conditions are often based on surface tribology, accounting for geometrical parameters as surface roughness and material parameters as hardness.

5.3.1 Normal Contact

In the case of normal contact between surfaces, the surface tribology may play a major role in the interaction. Constitutive models for contact between two surfaces have been developed by several authors as Greenwood and Williams (1966),Cooper et al (1969) and Kragelsky et al (1982). The normal contact between surfaces often yield some kind of compliant response which could be nonlinear in respect to both displacement, wear and several other variables. An example is here given by Kragelsky et al., resulting in a power-law described by equation (10).

$$p_n = c_n(g_n)^n \tag{10}$$

Here c_n and n are material dependent parameters which typically are experimentally determined. It should be noted that n typically lies in the range between 2 and 3.33 yielding a pronounced hardening response. g_n is here the normal displacement of the master surface into the slave surface.

In Abaqus, several normal contact constitutive equations are implemented. A softened contact interface can be modeled using either an exponential, a linear or a tabulated pressure-overclosure relationship. It is to be noted that the linear pressure-overclosure relationship implemented in Abaqus results from the penalty parameter, and not from a constitutive relation.

5.3.2 Tangential Contact

In tangential contact, one has to distinguish between two states, a stick state and a slip state. Stick means that there is no relative movement allowed between surfaces, and slip implies that there is relative movement between surfaces. Conditions for the transition between stick and slip, may be defined as done by Coloumb where slip is evident when $\tau_t > \tau_{fric}$ and there is stick when $\tau_t \leq \tau_{fric}$. This assuming that stick is the initial state, or that kinematic and static friction coefficients are identical. This condition does have weaknesses when it comes to numerical stability, due to its discontinuous behavior in the point of transition. This problem is overcome by a continuous approximation of the stick slip behavior as proposed by Oden and Pires (1983) and Raous (1999).

An example of such a function is:

$$t_t = -\nu\phi^i(\frac{dg_T}{dt})p_N \tag{11}$$

Here ϕ^i defines the shape of the stick slip transition and g_T is the tangential relative displacement between surfaces. ϕ^i may take the form of a polynomial regularization, a hyperbolic tangent regularization or a square root regularization. They are all approximation to the behavior suggested by Coloumb, but have the benefit of differentiability in the point of transition, allowing for more robust algorithms.

5.3.3 Non-Linear Tangential Contact

In the cases where parameters as surface roughness, relative sliding velocity , temperature and contact pressure between bodies is to be included, models based on elastic-plastic models have been developed. They are often based on non-associated elastic-plastic models and is considered standard in several finite element software packages. The finite element software to be employed does not offer non-linear friction models. In order to extend the Abaqus environment to a non-linear friction model, a numerical model is proposed, and can be found in section 13

6 Friction and Wear

6.1 A Continuum Approach

The treatment of friction and contact problems has been a subject of interest for many authors for a long time. In order to gain an understanding of the basic aspects of friction and wear, a continuum based theory is here introduced. One of the most central continuum theories of contact between bodies is the Hertzian contact theory, being a theory describing the intersection of a stiff circular body presses against an elastic half space. The Hertzian contact theory provides an analytical solution for the pressure needed for an indentation in the circular body into the elastic half space, and is widely expanded to several other scenarios. To gain an understanding of the basic concepts of inter body contact, some of the main principles of Hertzian contact theory is presented in this section.

6.1.1 Hertzian Contact Theory

When a point load is enforced on an elastic half space, the following expression for the surface displacement field is used:

$$u_x = \frac{1+v}{2\pi E}\left[\frac{xz}{r^3} - \frac{(1-2v)x}{r(r+z)}\right]F_z \tag{12}$$

$$u_y = \frac{1+v}{2\pi E}\left[\frac{yz}{r^3} - \frac{(1-2v)y}{r(r+z)}\right]F_z \tag{13}$$

$$u_z = \frac{1+v}{2\pi E}\left[\frac{2(1-v)}{r} + \frac{z^2}{r^3}\right]F_z \tag{14}$$

Here $r = \sqrt{x^2+y^2+z^2}$. If the displacement of the free surface is to be determined, the coordinate z is defined as zero. The given expressions are the displacement fields due to a single point load. The displacement gradient of the surface is assumed to be much smaller than unity. As this is a linear theory, superposition are utilized to expand the theory to arbitrary shaped load fields. The following expression for the free surface displacement field in z-direction is given as:

$$u_z = \frac{1}{\pi E^*}\int\int p(x',y')\frac{dx'dy'}{r} \tag{15}$$

$$r = \sqrt{(x-x')^2+(y-y')^2} \tag{16}$$

$$E^* = \frac{E}{1-v^2} \tag{17}$$

These expressions are based on an assumed pressure field, which does not necessarily equal a contact problem. For a contact problem involving a rigid body pressed against an elastic body, one can assume the surface displacement field to be known and equal the surface shape of the rigid body. If now the qualitative shape of the pressure field is assumed, one can determine the remaining parameters defining the pressure field.

If the indentation of a circular rigid body in a elastic half space is assumed, a pressure field p defined as in equation 18 and displacement field u_z as given in equation 19 can be found. This assumed pressure field is also known as a Hertzian pressure distribution.

$$p = p_0 \left(1 - \frac{r^2}{a^2}\right)^{0.5} \tag{18}$$

$$u_z = \frac{\pi p_0}{4E^* a}(2a^2 - r^2), \qquad r \leq a \tag{19}$$

$$F = \int_0^a p(r) 2\pi r dr = \frac{2}{3} p_0 \pi a^2 \tag{20}$$

Equation 19 and 20 are now general in the sense that they describe every displacement field u_z and force field F of the pressure distribution as in equation 18. If now a circular rigid body is introduced, and pressed into a elastic half space, the displacement field of the half space surface is assumed to take the shape of the rigid body. This displacement field u_z can be described as:

$$u_z = d - \frac{r^2}{2R} \tag{21}$$

If we compare equation 21 to equation 19 the parameters a and p_0 can be determined. This gives:

$$a = \sqrt{Rd} \tag{22}$$

$$p_0 = \frac{2}{\pi} E^* \left(\frac{d}{R}\right)^{\frac{1}{2}} \tag{23}$$

Which then give:

$$F = \frac{4}{3} E^* R^{\frac{1}{2}} d^{\frac{3}{2}} \tag{24}$$

However, if the contact involves intersection of two elastic bodies, the model can be modified to account for this. This can be found in the book by Popoc (2010).

6.2 Rough Surface Friction and Wear

When looking at a surface, one often observe an apparently smooth surface. However when the surface is examined closely, a certain surface texture may be observed. This surface texture or roughness plays a significant role in most real life situations and problems. The surface roughness has a pronounced influence on several phenomena as electrical contact, thermal contact and friction. The real contact surface of two intersecting bodies may greatly deviate from the surface of the two bodies observed by the eye. Real contact surface here means the surface area in contact, observed on a micro scale.

When observing the phenomenon of friction on a micro scale, one may observe cutting reactions of peaks in the contact interface caused by the breaking of microscopic bonds. Therefore, interface friction is influenced by factors such as material fracture strength, real contact area and normal force.

When there is interaction between surfaces, wear may occur. The process which we call wear is considered a highly complex phenomenon, as there are many different mechanisms involved.

The main four wear mechanisms are: adhesive wear, abrasive wear, corrosive wear and surface fatigue wear.

Adhesive wear is what occurs when there is a adhesive stick between the surfaces, causing parts of one surfaces to be torn out, and sticking to the other surface.

Abrasive wear is further discussed in section 6.2.2 and is caused by plastic ploughing of a harder surface into a softer surface, leaving a groove with displaced material on the sides. In the case of loads large enough to cause a cutting reaction, the material in the groove forms loose material.

Corrosive wear is the exposure of un-protected material to a corrosive environment due to sliding contact. This is typically associated with the removal of a passive or protective layer surrounding for example aluminum exposed to seawater, which then allows for further corrosive wear.

Surface fatigue wear happens when a material is loaded repeatively, causing a fatigue crack formation on or under the material surface, causing a subsequent breakup of the surface. This again may cause the formation of wear particles. This is known as fretting wear.

6.2.1 Non-Elastic Surface Response

When a rigid asperity is pressed against an deformeable half space and then displaced tangentially relative to the deformable surface, several scenarios may occur.

If the contact pressure between bodies is sufficiently low, meaning that the rigid body is either sufficiently blunt, or that the external force is sufficiently low, the deformation of the half space may be fully elastic. If this is the case, the

wear rate of the surface is low, as the only mechanism contributing to permanent deformations is fatigue. The only mechanism contributing to the frictional coefficient would then be adhesive friction.

If now the asperity has a reduced radius or the external forces are increased, the mode of the surface deformation changes to plastic. This means that the rigid sphere ploughes a groove in the deformable half space. The material which wear in the groove is then forced to the edges of the groove, causing a accumulation of wear material on the side ridges.

When the contact pressure is further increased, either with a reduced contact area by reduction of radius or by increased external loads, a cutting reaction occur. This means that some of the material in the groove is lost through a cutting reaction, causing the formation of loose wear material. The rest of the material is displaced to the groove's side ridges as with ploughing.

If now this movement is done repeatively, assuming a sufficiently high initial contact pressure to cause ploughing, the process may stabilize. This is caused by the increased contact surface as the aspherity deforms the deformable half-space, reducing the contact pressure to below the limit of plastic deformation. This contact pressure is denoted the shakedown-limit, and is a function of the friction coefficient and the shear yield stress.

The factor governing whether an elastic shakedown, ploughing or cutting takes place is governed by serveral factors:

* The interfacial friction coefficient
* The mechanical properties of the surface
* The distance between asperities
* The geometry of the asperities

In order to control the frictional and wear behavior of a surface, these factors has to be controlled and form several degrees of freedom influencing the desired results.

6.2.2 Abrasive Wear

Abrasive wear causes the formation of grooves in the softer body and the formation of wear particles. The volume of wear particles produces can be analytically estimated.

If the hard asperities are assumed to have a cone shape and a stiffness much larger than the softer body, the following expression can be assumed for the force required to indent the cone into the softer body:

$$\Delta F_N = \sigma_0 \pi r^2 \tag{25}$$

This expression is now used to predict the indentation depth of the asperity, and thereby its displaced volume in the softer body.

$$dV = Adx = r^2 tan(\theta)dx = \frac{\Delta F_N tan\theta dx}{\pi\sigma_0} \tag{26}$$

Where A is the area of the cone projected in the vertical plane. If now superposition of the number of cones are used and the expression is integrated over the displacement length, the following expression is obtained.

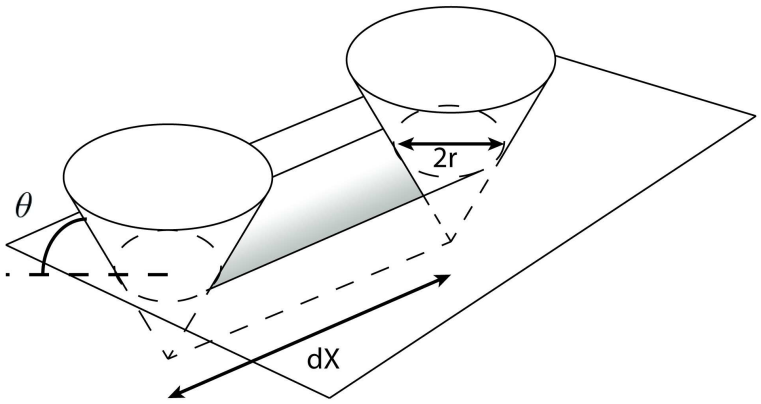

Figure 15: Illustration of cone cutting in infinite halfspace. The traveled distance dX, cone angle θ and radius at half-space surface r

$$V = \frac{F_N tan\bar{\Theta}}{\pi\sigma_0} \tag{27}$$

Here $\bar{\Theta}$ is the weighted average angle of all the cones used in the superposition. Rewritten this forms the Archard Wear Equation.

$$V = \frac{F_N K_{abr} x}{\sigma_0} \tag{28}$$

A other interpretation of the above equation rewrites the force and displacement into a equivalent work term.

$$V = \frac{\bar{k}W}{\sigma_0} \tag{29}$$

It should be noted that this expression has been shown to be valid only in the absence of wear particle accumulation. The presence of wear particles does effectively stagnate the formation of new wear particles, as they act as bearings in the interface (Popoc (2010)).

6.3 Coloumbs Friction

The first documented description of experiments on frictional between bodies are the early experiments of Leonardo da Vinci, who observed the independence of surface area and surface roughness to frictional forces. Later Couloumb (1733-1806) did a more detailed investigation on the phenomenon of friction. He discovered that the tangential frictional forces F between two bodies, subjected to a normal force P could be described by the following relation:

$$F_s = \mu P_n \tag{30}$$

The coefficient μ is often denoted the frictional coefficient, describing the relation between tangential frictional force and the applied normal force. This parameter was found to show very little correlation with surface roughness. However the material stiffness matching showed a pronounced correlation to the parameter.

A similar expression was also experimentally found by Coloumb for the frictional forces between bodies, when there is a relative motion between the surfaces.

$$F_k = \mu_k P_n \tag{31}$$

The coefficients μ and μ_k are often very similar, and often considered identical. However, for some material combinations the difference between static and kinematic friction may be prominent, and a continuous transition may as well be observed.

It is also interesting to note that the frictional forces often are time dependent. Coloumb observed that there was a deviation from the simplified laws of friction as described by equation (30) and equation (31) as the resting time between bodies increased. For metals, this phenomenon is explained by the viscous properties, which increases the contact surface with time causing a logarithmic trend (Popoc (2010)). This again reduces the creep rate, due to the lower interface stresses. It is also noted that capillary forces between bodies may as well exhibit a logarithmic response on the frictional forces.

7 Constituents of the Numerical THA Analyses

Numerical models able to predict primary stability, has been found to be greatly influenced by the assumptions made in the analysis, as discussed in section 3.2. In this section, findings from the literature employed in the model development are presented. External loads, mechanical properties, coordinate system and recommendations with respect to the numerical aspects are discussed in the following sections.

7.1 Mechanical Properties of Human Bone

Human bone tissue is divided into two main classes, being: trabecular (spongious) bone and cortical (dense) bone. The two types of bone tissue deviate in their micro-structure and mechanical properties. Cortical bone is often found in regions dominated by a uni-axial load pattern as found in the femoral shaft. Trabecular bone is commonly found in the interior of bones and in regions with a lower loading, as in the interior of the greater trochanter. The amount of trabecular and cortical bone in the femoral cross-section does therefore vary depending on location (Reilly & Burstein (1974)).

The work of Reilly & Burstein (1974) is the source of mechanical properties used in this thesis. The work was performed in 1974, but no findings contradicting the determined parameters are known to the author.

7.1.1 Trabecular Bone

Trabecular bone has a structure made by connected rods and plates, forming a complex micro-structure. The mechanical properties of trabecular bone on a tissue level is to date of high uncertainty (Bayraktar et al. (2004)). The tissue level properties are however only of interest in analyses accounting for response on a micro-level, and the global response of trabecular bone is well documented as by Reilly & Burstein (1974). Typical bone properties of trabecular bone is found in the review of Reilly & Burstein (1974). Trabecular bone yields an isotropic response with typical properties of $E = 0.325$ GPa and $v = 0.29$.

Figure 16: Trabecular(Spongious) bone. The pore-size of trabecular bone is typically in the area of 1mm. Caption from *Science Photo Library, Trabecular Bone* (02.06.2012)

7.1.2 Cortical Bone

Cortical bone has a far denser structure made up of osteons, being longitudinally directed canals. This is thought to cause the anisotropic nature of cortical bone. Typical values of cortical bone is found in the literature both on a tissue level and on a global level.

Typical properties for the global level response are $E_x = 17$ GPa, $E_y = 11.5$ GPa, $G_{xy} = 3.6$ GPa, $v_{xy} = 0.31$ and $v_{yz} = 0.58$, with x denoting the longitudinal direction of the Havarsian envelopes, and y being the transverse direction (Reilly & Burstein (1974)).

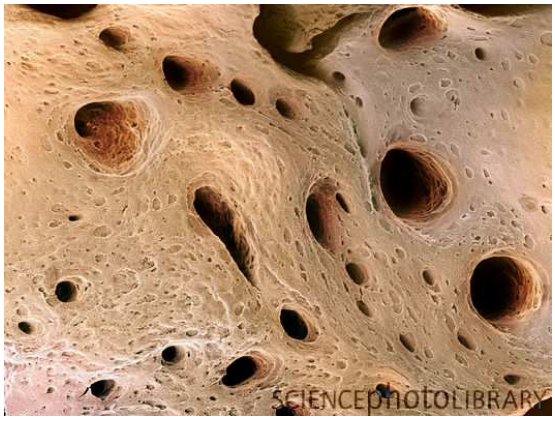

Figure 17: Cortical(Dense) bone. The typical diameter of a Havarsian envelope is in the area between 28 and 135 microns. Caption from *Science Photo Library, Cortical Bone* (02.06.2012)

The investigation done by Reilly & Burstein (1975) determined the anisotropic

ultimate properties of cortical bone, reporting a pronounced anisotropy with regards to ultimate stress. The mean longitudinal fracture strength found was 135MPa, whereas the mean transverse fracture strength was as low as 53Mpa.

Human cortical bone exhibits a significant plastic response (Reilly & Burstein (1974)). The total deformation of test specimens at failure has been shown to constitute of over 70% plastic deformation. The pre-yield response exhibits a typical Hookian response and the post-yield state shows a work-hardening as illustrated in figure 18, being data extracted from the work of Reilly & Burstein (1974). The values employed in subsequent simulations are $\sigma_y = 115$ MPa and $\sigma_u = 150$ MPa. The corresponding strains are $\varepsilon_y = 0.008$ and $\varepsilon_u = 0.048$. The mechanical properties of the human cortical bone do however vary due to position, health and age of the individual (Reilly & Burstein (1974)).

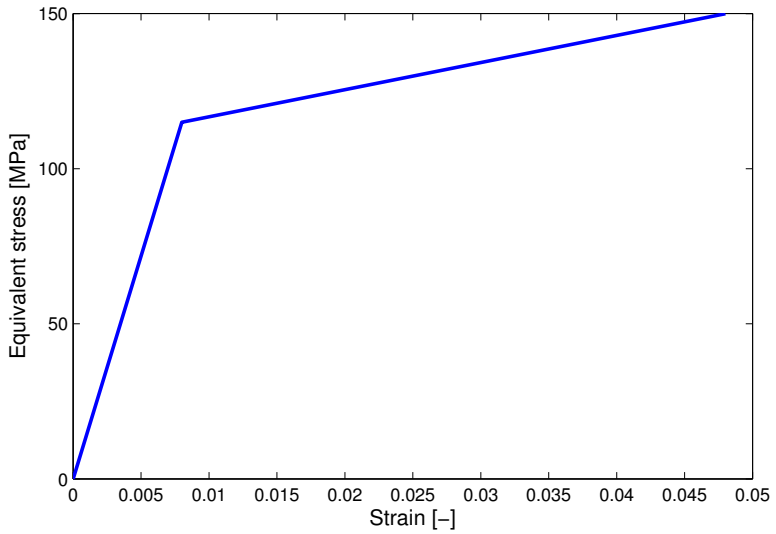

Figure 18: Typical plastic response of human cortical bone, as found by Reilly & Burstein (1974)

7.2 Global and Local Coordinate System

In order to ensure consistency with the input data used in the model, and to ease data extraction, the global coordinate system $[X, Y, Z]$ used by Bergmann & Graichen (1993) also found in the work by Bergmann et al. (2001), is adopted and illustrated in figure 19. In order to extract data from the reamed cavity and the prosthesis surface, a local coordinate system $[\bar{X}, \bar{Y}, Z]$ is defined.

As the longitudinal axis of the prosthesis is aligned with the longitudinal axis of the femur in the analysis, they share the same axis Z. The anterior-posterior axis Y is in the global coordinate system is defined as by Bergmann & Graichen

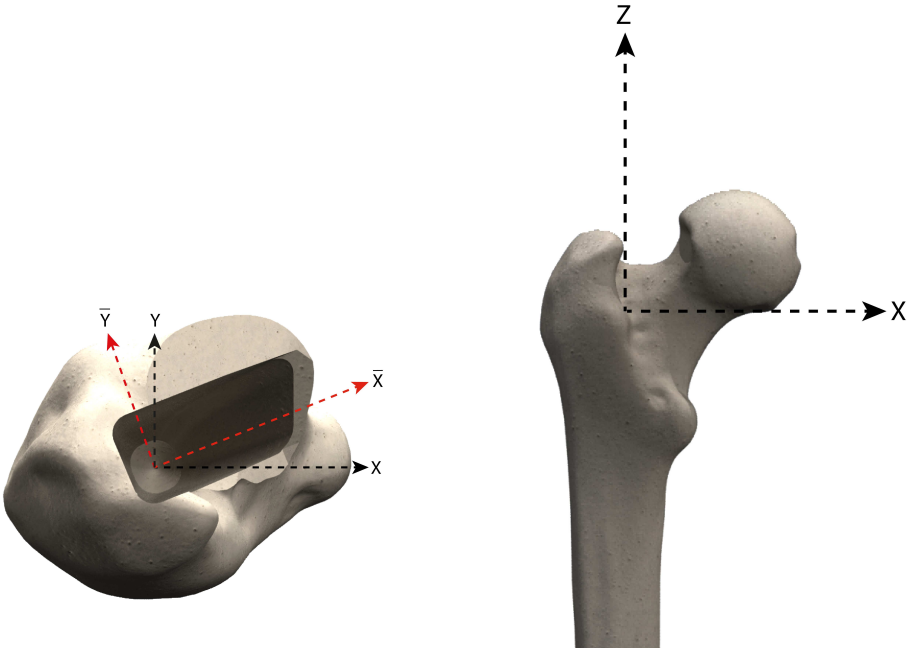

19a: Proximal-Distal view

19b: Anterior-Posterior view

Figure 19: Global coordinate system $[X, Y, Z]$ as defined by Bergmann & Graichen (1993), and local prosthesis coordinate system $[\bar{X}, \bar{Y}, Z]$

(1993), being the center axis through the inner and outer condyles. This axis corresponds to the axis of rotation for the knee joint. In the local coordinate system, the medial-lateral axis $\bar{X}$ is defined as the tangent to the medial-lateral axis of the prosthesis. The angle between the local coordinate axis $\bar{X}$ and the global coordinate axis X is here 14°.

7.3 Femoral Loads

The human femur is subjected to a highly complex load field both from contact between the femoral head and the acetabulum, as well as from muscles attached to different locations on the femur. Numerical analyses investigating the influence of muscle forces on the femoral stress and strain distributions has been done by several authors, highlighting its influence (Duda et al. (1998)). In this section, femoral loads are introduced and discussed.

7.3.1 Joint Moments and Forces

Contact between the acetabulum and femoral head is the point of load transfer between the lower extremities and the upper body. The loads transferred has been found to vary depending on the physical activity as well as between individuals. There are two load scenarios commonly used in micro motion analyses, being a one legged stance based on walking, and stair climbing. The choice of loading scenarios for the following analyses is based upon the frequency of which they occur and their peak loads. The work of Morlock et al. (2001) indicated that the most frequent loading scenario for THA patients is walking, and is therefore a loading scenario considered relevant for this study.

Torsional loads have been suggested the most critical load scenario by several authors (Kassi et al. (2005),Bergmann et al. (2001)), and is also one of the top five most frequent activities for THA patients (Morlock et al. (2001)). The load field extracted from stair climbing is therefore included in the analysis.

Previously, the femoral loads were determined using optimization routines. The use of optimization routines was necessary as the load field in the proximal region of the human femur is over determined. Later this was done using instrumented femoral implants tested in in vivo situations. However, none of these studies included detailed gait data but rather peak loads from scenarios as stair climbing or walking.

The investigation by Bergmann et al. (2001) used instrumented femoral hip prostheses and telemetric transmitting techniques. The patients used in the data sampling had a healing time of 9years and the measuring technique allowed for continuous determination of forces and moments in the whole load cycle. The available amount of data is large and in order to reduce the data down to a manageable complexity, the maximum forces were extracted from the work of Bergmann et al. (2001).

The extracted data are peak loads based on the work of Bergmann et al. (2001). Forces as function of time are illustrated in figure 20.

The direction of the load on the femoral head does change direction throughout the loading cycle, but the study of Bergmann et al. (2001) concluded that the change in direction is to be considered very small.

Hip Joint forces $[\%BW]$			
Activity	F_x	F_y	F_z
One legged stance	-35	-15	-230
Stair climb	-60	-60	-240

Table 2: Hip joint forces defined in coordinate system illustrated in figure 19. Taken from the work of Bergmann et al. (2001)

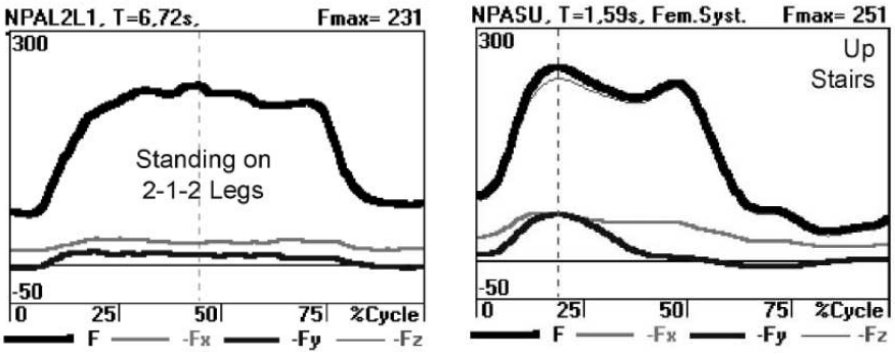

20a: Walking 20b: Stair climbing

Figure 20: Contact forces based on an one legged stance a) and stair climbing b). Data extracted from Bergmann et al. (2001)

7.3.2 Muscle Forces

The work of Bergmann et al. (2001) did only provide forces acting on the prosthesis head. In addition, there is also a load transfer through a number of muscles attached to the femur. The complexity of tendons and muscles are large on the human femur, but a simplified equivalent load field has been suggested by Morlock et al. (2001). This simplified load field has shown to reproduce the femoral strain patterns with good accuracy, and with a great reduction of modeling complexity compared to including all muscles and tendons. The attachment points of the muscles are reduced to three points with several muscle equivalent forces attached to each point. The force vectors are assumed not to change direction in time and the force magnitudes corresponds to the maximum value obtained throughout the load cycle. Muscle equivalent loads are given in table 3 for the walking case and in table 4 for the stair climbing case.

Points of attachment for the muscle loads are illustrated in figure 21 and based on the coordinates provided by Morlock et al. (2001).

Forces [%BW] from walking cycle				
Muscle Group	F_x	F_y	F_z	Point of attachment
abductor	58.0	4.3	86.5	P1
tensor fascia latae, proximal	7.2	11.6	13.2	P1
tensor fascia latae, distal	-0.5	-0.7	-19.0	P1
vastus lateralis	-0.9	18.5	-92.9	P2

Table 3: Simplified muscle load field based on a walking cycle. Extracted from the work of Morlock et al. (2001)

Forces [%BW] from stair climbing				
Muscle Group	F_x	F_y	F_z	Point of attachment
abductor	70.1	28.8	84.9	P1
ilio-tibial tract, proximal	10.5	3.0	12.8	P1
ilio-tibial tract, distal	-0.5	-0.8	-16.8	P1
tensor fascia latae, proximal	3.1	4.9	2.9	P1
tensor fascia latae, distal	-0.2	-0.3	-6.5	P1
vastus lateralis	-2.2	22.4	-135.1	P2
vastus medialis	-8.8	39.8	-267.1	P3

Table 4: Simplified muscle load field based on stair climbing. Extracted from the work of Morlock et al. (2001)

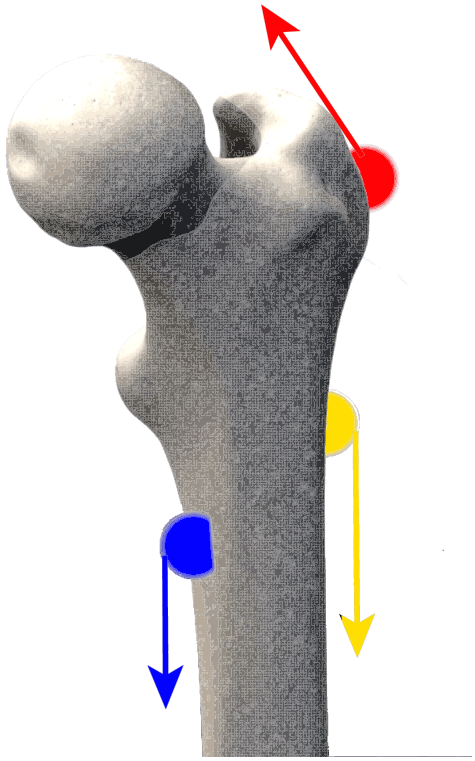

Figure 21: Point of attachment for muscle equivalent forces. P1(Red), P2(Yellow) and P3(Blue)

7.4 Recommendations for Numerical Analysis of THA

A large number of finite element analyses on THA have been done through the years, with a large span of input parameters (Bernakiewicz & Viceconti (2002)). There are many factors affecting the results of such a finite element analysis, ranging from mesh and discretization problems, to the choice of parameters used in the numerical solving process.

A range of parameters thought to influence analyses of THA were investigated by Bernakiewicz & Viceconti (2002), and some findings and recommendations are presented in this section.

Several of the analyses investigated by Bernakiewicz & Viceconti (2002), deviate in their choice of contact elements, method of constraint imposition, choice of contact stiffness, contact traction control, convergence tolerance and convergence norm. Several of the studies did not even document their methods.

The investigation was done as a parametric study based on the experimental setup by Baleani et al. (2000), using a numerical study by Viceconti et al. (2000) as a benchmark case. In order to isolate the individual parameter's influence on the results, single parameters were varied and their influence mapped. It was assumed that the physical parameters determined from experiments were correct, and it was emphasized that the results were connected to a specific geometry.

Only two parameters were found to have a significant influence on the end results. The choice of contact stiffness (penalty parameter) and the choice of convergence criterion was found to have significant influence on the results. The average error was found to stabilize as the contact stiffness passed 600-700N/mm, but with an increasing computational cost. The opposite trend was found for a increased convergence tolerance. The increased tolerance reduced computational costs, and increased both peak and average errors. Based on these findings, Bernakiewicz & Viceconti (2002) stated the following for analyses of THA:

"*A finite element model is fully qualified when the level of mesh refinement and the contact stiffness are assigned after multiple exploratory runs and when all parameters with a physical meaning have been accurately identified with previous independent experiments. From the present study, it can be concluded that using such a model it is possible to carry out predictions without a direct experimental validation of the model. Stress residuals, convergence tolerance and contact compenetrations*[5] *can be used to define an upper bound for the model error, in combination with the necessary sensitivity analyses on the parameters uncertainties.*"

Taking these recommendations into account, a purely numerical study is done in this thesis.

[5]The penetration of the master surface into the slave surface

8 Development of a FE-Model

The main goal of the FEM analysis is to give a qualitative measure of primary stability on un-cemented hip prosthesis. The possible influence of impact grafting on primary stability is to be investigated, and loads mimicking impact grafting is therefore included. Earlier studies regarding primary stability of un-cemented hip prostheses, has neglected pre-stressing of the femur under impact grafting. To investigate this, a parameter study covering the impaction force under grafting and the frictional response from the femoral bone is performed. This is done in two separate analyses, isolating the impaction force as the only variable in one analysis, and frictional coefficient as the only variable in the other.

The prosthesis geometry used is a Gladiator prosthesis produced by Wright Corp. The Gladiator prosthesis is a commonly used un-cemented prosthesis with a relatively simple geometry. The prosthesis is modular in the sense that different neck angles and lengths can be chosen under surgery, along with the option of a collar. The prosthesis geometry was simplified in the sense that a small groove on the proximal end was removed, and the collar option not used. The entire neck and head region of the prosthesis was removed, and equivalent loads placed on the proximal end of the prosthesis.

In order to develop a model giving relevant results, an anatomically correct femoral geometry is discretized. The femoral geometry used is based on a 3D-scan provided by "Redding Engineering LLC" and the geometry is further verified through comparison to available roentgenographic images. The geometry was rescaled to represent an average male femur, and is prepared using the surgical procedures provided with the Gladiator prosthesis (Wright (2010)).

In the following sections, the preparation of the geometry, application of loads, data sampling and mesh verification are discussed. The resulting model is later used in the numerical investigation of primary stability.

8.1 Preparation of the Geometry

The discretized prosthesis geometry is based upon Gladiator templates functioning as a basis for the 3D geometry. The geometry is exact in its geometrical measures, but simplifications on the prosthesis neck not in contact with the bone were made in order to simplify the meshing procedure. Based on the prosthesis geometry, a reamer equivalent geometry was developed in order to produce a cavity representative to what could be produced in a real surgical procedure, assuming a zero interference fit. The reamer was extended with one millimeter distally in order to avoid load concentrations in the distal end of the cavity. This elongation is justified by the high concentration of trabecular bone in the distal end of the reamed cavity, having a reduced load carrying capac-

ity relative to cortical bone. All CAD-work was done using the latest version of Solidworks with all geometries exported to Abaqus for meshing and analysis.

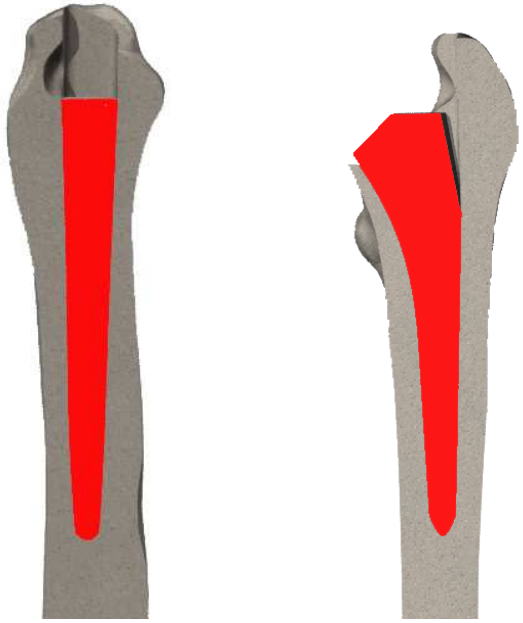

22a: Medial-anterior view

22b: Anterior-posterior view

Figure 22: Prosthesis orientation. Prosthesis marked in red

In order to reproduce a fit representative to what is obtained under surgery, the steps described in section 4 were performed.

The femoral head is first cut in a 45° angle relative to the femoral shaft central axis. The reamer is then positioned such that it follows the curvature of the endo-cortical envelope. This envelope is not present in the geometry, and is therefore approximated through comparison to roentgenographic images. The prosthesis orientation and location was then validated with the help of an experienced surgeon, and the obtained fit is shown in figure 22. The femur is then cut approximately 80 mm distally of the distal tip of the prosthesis. The cut is assumed not to interfere with the stress field caused by the prosthesis.

8.2 Applying Loads

In order to construct a model with a manageable complexity accounting for the external loads on the femur, the loads on the femoral head are simplified to moments and axial forces acting on the top of the prosthesis. The muscle forces are assigned as traction onto three points on the femur, see figure 23

Figure 23: Constrained model with global coordinate system and points used for loading. Muscle loads are marked in Red, Yellow and Blue, whereas all prosthesis loads are assigned at prosthesis reference point(Green).

8.2.1 Head Loads

In order to impose the head contact forces onto the prosthesis without using a prosthesis neck, the forces are translated into equivalent forces and moments. The forces and moments are then assigned to a reference point, fully constrained to the top of the prosthesis, see figure 24.

The translation of forces from the femoral head to the reference point results in additional moments. The distances used to calculate the moments were based on the center point of the femoral head prior to surgery, and the reference point on the prosthesis. The position of the reference point relative to the femur, corresponds to the prosthesis sitting in the bottom of the femoral cavity without additional forces applied.

In order to spread the forces and moments onto the prosthesis top, the reference point is tied to the prosthesis top surface.

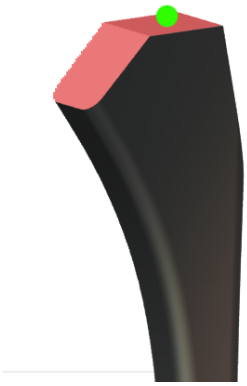

Figure 24: Reference point (green), fully constrained to the femoral neck region (red).

8.2.2 Impact Grafting

The loads applied by the surgeon during surgery, are simplified into an longitudinal force acting at the reference point at the prosthesis top. Cummins et al. (2011) found a threshold grafting force of 0.5KN for femoral fracture. This value would translate to an longitudinal force of 62 %BW in the case of a 82 Kg person. The loads during routine activities have been found to impose axial loadings on the femur of 230% BW and 240% BW for walking and stair climbing respectively. This is a significantly higher load than suggested by Cummins et al. (2011). Practice varies between hospitals with respect to post surgery loading of the femur. The practice of several hospitals include full loading of the femur immediately after surgery (Olav (2012)).

The fracture strength of human cortical bone has been found by Reilly & Burstein (1975) to be approx. 50Mpa in the transverse direction of the bone, being perpendicular to the longitudinal direction of the femoral shaft. This has been an indicator of the acceptable amount of bone pre-stressing in numerical analysis as by Abdul-Kadir et al. (2008). The analysis by Abdul-Kadir et al. (2008) used the maximum principal stresses in the interface as a criterion for femoral failure, and is also here adopted.

8.2.3 Muscle Loads

The simplified muscle load model developed by Heller et al. (2005) discussed in section 7.3.2, reduces the muscle forces into force vectors acting at three points on the femur. The points are illustrated in figure 23. The location of the points are based on coordinates provided by Morlock et al. (2001). The force vectors are assigned in the points as general traction, resulting in two shear components and one pressure component. The model by Heller et al. (2005) assumes that the direction of the force vectors does not change in time.

8.2.4 Load History

As can be observed in figure 20, the load history throughout one gait cycle is non-linear. In the numerical model here developed, the application of loads is simplified into linearly increasing loads. This is done in order to reduce the complexity of the analysis and the computational time. The function used to describe the load history is a ramp function with a maximum amplitude equivalent to the maximum load. This simplification is based on the assumption that due to the neglecting of viscous effects, only the maximum amplitude of the load has an effect on the displacement of the prosthesis. This assumption is however considered a point of uncertainty, and should be a subject for further investigation.

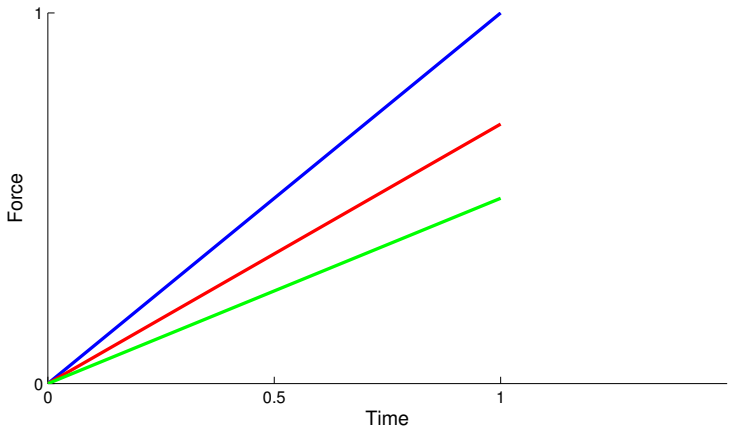

Figure 25: Symbolic representation of load ramping. All loads, including muscle forces are simplified into a ramped load

8.3 Data Sampling

Micro motion values vary depending on location on the femur. The sampling regions used for data acquisition are here presented, as well as the post processing done on the exported values.

8.3.1 Gruen Zones

The locations used for data acquisition has been found to greatly influence the micro motion measurements in experimental setups. The work of Pancanti et al. (2003) and Reggiani et al. (2007) both based their data sampling on a region definition by Gruen, commonly used in roentgenograpic terminology. The Gruen zones are chosen due to their clear definition, and independence to geometrical variations. The Gruen zones are illustrated in figure 26.

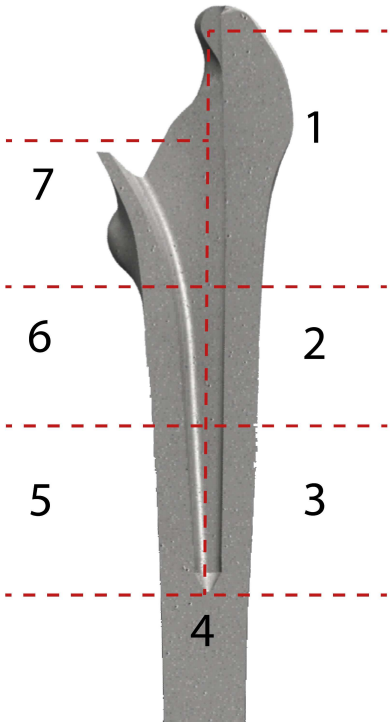

Figure 26: Illustration of Gruen zones

The numbering starts at the greater trochanter ending above the lesser trochanter. The main characteristic points are the bottom of the lesser trochanter and the distal end of the prosthesis. The midsections (2,3,5,6) are separated at the mid distance between the lesser trochanter and the distal end of the prosthesis. The micro motion values used are the peak values in the respective gruen zones.

8.3.2 Sampling Paths

In order to investigate the pressure distributions along the prosthesis surface, two paths located medially and laterally were defined, see figure 8.5. Data are the plotted as a function of the z-distance from the distal end.

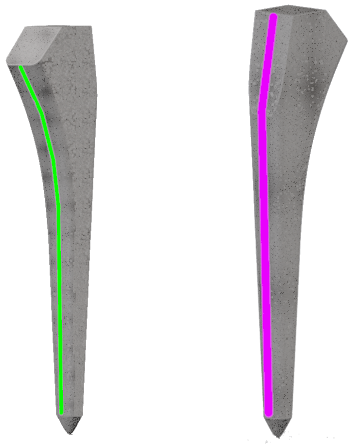

27a: Medial-anterior view

27b: Distal-posterior view

Figure 27: Sampling paths used for data extraction. Medial (Green) and lateral (Purple)

.

8.3.3 Micro Motion

Micro motion is defined in section 3.1.1, and is sampled as peak values in the Gruen zones. The extracted values are named $Cslip_1$ and $Cslip_2$ in Abaqus, being accumulated nodal slip values (Simulia (2012)). The slip components correspond to a local coordinate system, which does not necessarily coincide with the global coordinate system of the model. In order to obtain slip values that are independent of the orientation of the local coordinate system, the equivalent value is calculated using equation (32):

$$Cslip_{eq} = \sqrt{Cslip_1^2 + Cslip_2^2} \tag{32}$$

It should be noted that the slip variables $Cslip_1$ and $Cslip_2$ are updated only for positive contact pressures. The slip values used should therefore originate from nodes having a positive contact pressure in the whole loading cycle.

8.4 Material Properties

In order to reduce the complexity of the analysis, the whole femur is assumed homogeneous with the mechanical properties of cortical bone. This assumption is based on the large portion of cortical bone in contact with the prosthesis after reaming, and that the surgeon's evaluation of the prosthesis fit is based on cortical bone contact as discussed in section 4. Ct-based meshes from real femurs are considered superior on this point, but is here avoided due to time constraints.

The femur is assumed isotropic and homogeneous with elastic properties being E=17 Gpa, and ν=0.3. This is an approximation to the properties found by Reilly & Burstein (1975). Plastic response is as presented in section 7.1.2, and isotropic linear hardening and a yield stress of 115 Mpa is assumed in the analyses.

The prosthesis material was assumed isotropic with linear elastic response, using E=110 Gpa and ν=0.3, being equivalent to titanium alloys commonly used in prosthesises. The assumption of linear elasticity was justified later in the analysis as stresses were found to be lower than the yield stress of titanium.

8.5 Mesh Generation

The mesh was generated using the built-in in meshing algorithms in Abaqus, using a manual seed in the interior of the reamed canal. The appropriate mesh refinement was determined from several factors such as: contact pressure distribution, the energy response of the system and frictional dissipation energy from the prosthesis-bone interface. The elements used were quadratic tetrahedrons (D3T10), as they showed superior performance compared to brick elements with regards to ease of creating a functioning mesh with the built-in meshing algorithms.

The converged mesh contained 58584 elements (86820 nodes) for the bone mesh and 20680 elements (31181 nodes) for the prosthesis mesh. The number of nodes used is almost one order of magnitude above the mesh used by Abdul-Kadir et al. (2008). The seed used for the converged mesh was 4 mm globally with a 2.5 mm seed for the reamed cavity and the prosthesis. The reason for this deviation in mesh refinement, is unknown but is thought be caused by difficulties in contact surface reproduction. The study by Abdul-Kadir et al. (2008) used another FE-software which could have reproduced this interface more efficiently.

8.6 Mesh Verification

In order to verify the model's response to loading, a series of investigations were performed with different mesh refinements. The mesh refinement has an

28a: Medial-anterior view 28b: Distal-posterior view

Figure 28: Illustration of bone geometry 1) and the converged mesh b)

influence on both the global response to loading, and the reproduction of local phenomena such as contact and stress concentrations (Wriggers (2006)). In order to methodically investigate the model's response to loading, the bone and prosthesis meshes are first investigated individually without any kind of contact. This is done in order to uncover the individual meshes response to loading, avoiding phenomena caused by contact.

When the individual meshes have obtained an acceptable convergence, contacts between the parts are investigated with the converged meshes as an initial setup. When the frictional dissipation, internal energy and contact pressure field have obtained convergence, the model is considered sufficient with regard to micro motion reproduction. The compenetration governed by contact stiffness and convergence tolerance, has to be within the recommendations by Bernakiewicz & Viceconti (2002).

8.6.1 The Response of the Femur Mesh

The global response of the bone mesh was investigated through a gradual mesh refinement, monitoring the models internal energy. An axial compressive force was assigned proximally and off centered to trigger a bending, compressive and torsional mode. The internal energy of the system was monitored as the mesh was refined. As linear elasticity and no form of contact is present, internal energy and external work are equal and internal energy is therefore the only monitored parameter.

The mesh refinement started at a global element size 10 mm, which was considered out of bound for proper geometric discretization at the proximal end of the femur. Small curvatures were poorly described by the 10 mm mesh but it was included in order to observe a clear trend in internal energy. The mesh was gradually refined and a gradual increase in internal energy was observed, illustrated in figure 29.

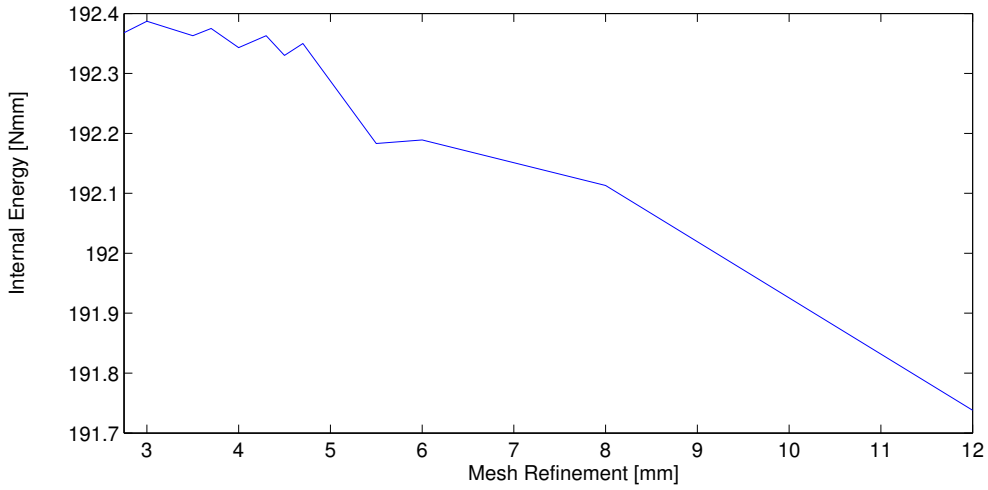

Figure 29: Internal energy as function of mesh refinement. Note a plateau in internal energy below 4.5mm.

The mesh refinement investigation uncovered threshold mesh resolutions for avoidance of excessively distorted elements. Global element seeds larger than 8 mm caused distorted elements to be formed, which was considered unfavorable for the analysis and therefore avoided.

The internal energy reached a plateau at a element size of 4.5 mm ,with only minor fluctuation of below 0.05% as the mesh was further refined. For the investigation of prosthesis-bone interaction, 4 mm was chosen as an appropriate global element size for the femur, acting as a compromise in computational cost, still located at the internal energy plateau.

8.6.2 The Response of the Prosthesis Mesh

The procedure used to investigate the prosthesis mesh was identical to the procedure used on the femur mesh. Convergence in internal energy was obtained for a global seed of 6 mm. However, in order to have matching mesh refinements on the femur and prosthesis, the prosthesis refinement used for prosthesis-bone interaction was 4 mm.

8.6.3 Bone Prosthesis Interaction

In order to verify the models ability to reproduce the frictional behavior of the contact interface, and thereby micro motion, several parameters illustrating the models behavior are monitored. In order to avoid the introduction of further non-linearities, linear elasticity is assumed. Both prosthesis and bone used a 4 mm mesh as a initial setup for verification of the bone-prosthesis interaction.

The contact constraints were enforced using the prosthesis surface as master surface, and the reamed cavity as a slave surface. The tangential contact constraints were enforced using the penalty method with a frictional coefficient of 0.3 using Coloumb friction. A frictional coefficient of 0.3 corresponds to a mid-value for the later analyses. The normal contact was enforced using the same method, using a linear overclosure relationship.

Contact between the bone and the prosthesis was made by pressing the prosthesis down into the cavity of the femur. This was done by enforcing a displacement on the proximal end of the prosthesis, directed in the longitudinal direction of the bone. The assigned displacement was equal for all mesh refinements.

A displacement of 5 mm was assigned at the top surface of the prosthesis and directed along the center axis of femoral cavity. This displacement constraint was removed at the end of the analysis. The distal end of the femur was fully constrained. The prosthesis was also constrained in both out of axis directions in order to ensure convergence. This constrained setup is not intended to exactly reproduce any in-vivo situation but rather test the model and its interface response to loading both with respect to surface reproduction and energy response.

In order to investigate the behavior of the contact interface, pressure distribution and frictional dissipated energy are monitored. The contact pressure distribution was monitored using the paths introduced in section 8.3.2.

From the resulting contact pressure distributions, it is observed that the influence of mesh refinement was most pronounced medially. The contact pressure distribution from the medial side is therefore used in the investigation of convergence. The medial pressure distribution for several mesh refinements are presented in figure 30

The contact pressure distribution shows a stabilizing trend down to an element size of 2.5 mm. Below this mesh refinement, only limited changes in

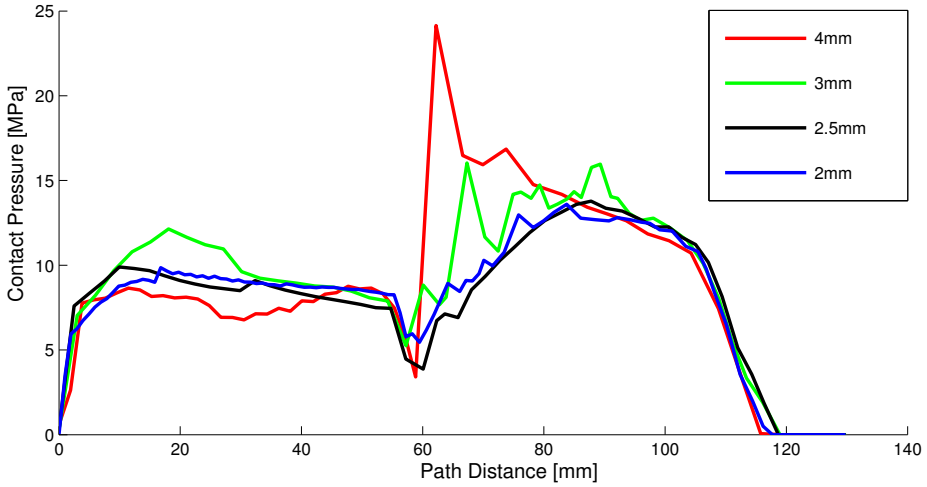

Figure 30: Medial contact pressure distribution for several mesh refinements.

pressure distribution is observed, but with an increasing computational cost.

Another indicator on the contact interface's behavior is dissipated frictional energy. As the 4mm meshes were used as an initial setup, the model could very well have reached a converged state. This was found not to be the case as frictional work, internal energy and external work were affected by a further mesh refinement, see figures 31, 32 and 33.

The frictional dissipation energy was reduced by 68.8% when the mesh seed was reduced from 4mm to 3mm. The internal energy showed a increase of only 1.9% for the same change in mesh refinement. The external work showed a reduction of 55.5%. However, after this transition, the internal energy, external work and dissipated frictional energy stabilized.

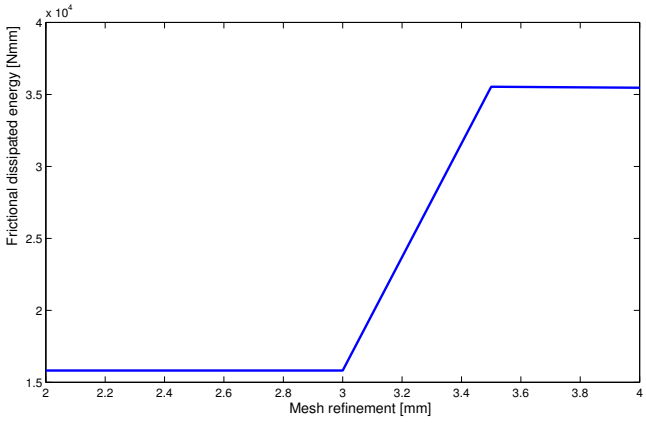

Figure 31: Frictional dissipated energy as function of mesh refinement.

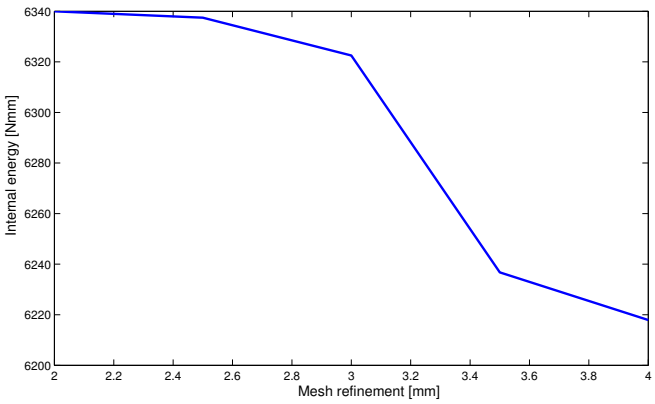

Figure 32: Internal energy as function of mesh refinement.

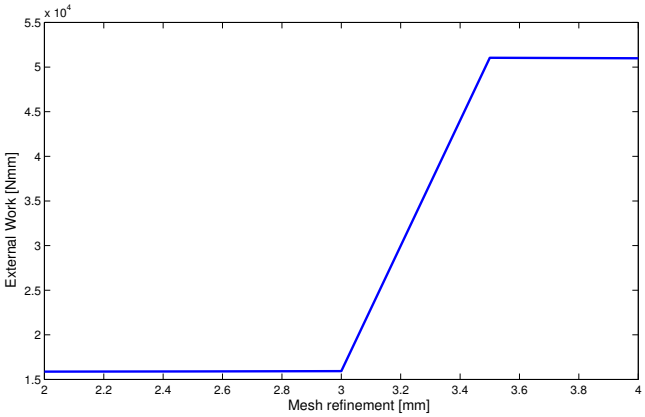

Figure 33: External work as function of mesh refinement.

The monitoring of energy parameters does not uncover the mesh's ability to reproduce local phenomena as stress peaks, but rather the models global response. As micro motion is a phenomenon connected to friction in the prosthesis-bone interface, frictional dissipated energy is used as an indicator. The frictional dissipated energy is a work integral of frictional force and the corresponding displacement. If the frictional dissipated energy converges, it indicates that the work integral of frictional force and interface micro motion converges. As the frictional forces are connected to contact pressure, the convergence in contact pressure is used to give an indication of frictional force convergece. From figure 30, limited changes in contact pressure distribution are observed for element seeds below 3 mm. This corresponds to the transition point observed in figure 31. If based on this observation, the frictional forces are assumed equal for all mesh refinements below 3 mm, the changes in micro motion should be evident in the dissipated frictional energy.

As the dissipated frictional energy remains stable for mesh refinements finer than 3mm, meshes finer than 3mm are considered able to reproduce interface micro motion sufficiently. Based on this finding a global seed of 4mm is used for the femur, and a seed of 2.5mm is used in the reamed cavity. Matching meshes between the reamed cavity of the femur and prosthesis are used, resulting in 2.5mm element size for the prosthesis mesh.

The contact stiffness and convergence tolerance has been highlighted by Bernakiewicz & Viceconti (2002) as parameters with a significant impact on micro motion analyses. The convergence tolerance was by default significantly lower than the lowest value used by Bernakiewicz & Viceconti (2002), and is therefore assumed appropriate. In order to investigate the contact stiffness influence on compenentration, a parameter study done on the above described mesh and setup was done, resulting in the trend observed in figure 34.

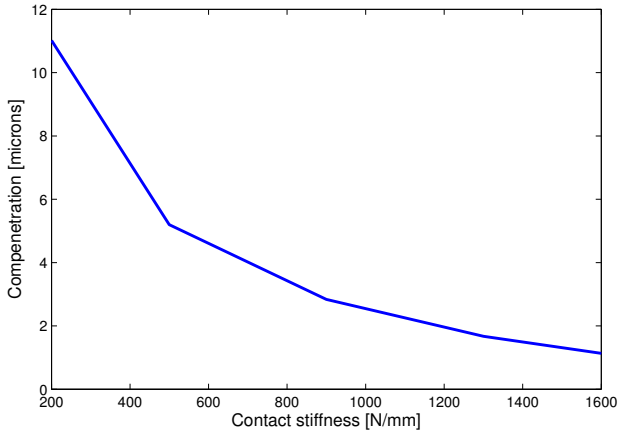

Figure 34: Surface compenetration peak values as a function of contact stiffness.

As the contact stiffness is increased, the compenetration shows a steep reduction. The reduction in compenentration from a contact stiffness of 1300 N/mm to a contact stiffness of 1600 N/mm was found to be 32.2% which is far more than found by Bernakiewicz & Viceconti (2002). Convergence difficulties were found for contact stiffnesses above 1600 N/mm, indicating this as a upper bound. It should be noted that the compenetration is far lower than found by Bernakiewicz & Viceconti (2002). The chosen contact stiffness of 1300 N/mm gave a upper bound for compenetration of approximately 1.7 microns.

9 The Analyses

The following studies use the verified model discussed in section 8.6. The loads used are introduced in section 8.2.

Following are two analyses. The influence of the magnitude of the impaction force used under impact grafting is investigated in one study. The effect of a potential residual pressure field is of interest, as the contact pressure between the prosthesis and bone has been found to influence primary stability. A study including the grafting phase, using the impaction force as the only variable is done in section 11.

The friction coefficient assumed in the interface between prosthesis and bone has been found to have limited influence on micro motion, for friction coefficients over 0.15 (Kuiper & Huiskes (1996*b*)). The study by Kuiper & Huiskes (1996*b*) did not include the grafting phase of the surgery. As the grafting phase was neglected, the possible influence of this simplification is investigated in this study. An analysis including the grafting phase is performed, using the interface friction coefficient as the only variable. This analysis is found in section 10.

In order to understand some of the effects at hand, a preliminary study was done using a simplified geometry. This study is presented in section 12, and it is important to note that the geometries and loads are not equivalent to a real femur and prosthesis, but rather highly simplified scenarios meant to isolate single phenomena.

10 Investigation of Pressure Field to Frictional Coefficient Coupling

10.1 Objective

The relative movement in the prosthesis-bone interface is constrained by the geometrical shape of the prosthesis, and frictional forces (Götze et al. (2002)). The frictional forces surrounding the prosthesis are function of the contact pressure as discussed in section 6.3, and could therefore influence the micro motion of the prosthesis.

Based on the preliminary analysis of a simplified geometry, it was expected that the interface frictional coefficient has influence on the contact pressure field obtained after grafting, see section 12. In the preliminary study , the contact pressure field was influenced by the frictional coefficient, and it was found that the contact pressure could be increased with a lower frictional coefficient. A relative shift in contact pressure distribution towards the proximal end was observed as the friction coefficient decreased. If this coupling between contact pressure and frictional characteristics is evident also in a real THA scenario, it could provide one additional degree of freedom for further improvement of the designs.

The process of pressing the prosthesis into the reamed cavity is as described in section 4. The impact grafting procedure is simplified into a axial force as in the experiments by Cummins et al. (2011).

It is noted by Cummins et al. (2011) that the axial force threshold values for femoral fracture obtained experimentally, could be conservative due to a reduction of material toughness. The experiments performed suggested that a lower bound for the axial load used under impact bone grafting is as low as 0.5 KN, see section 4.3. If the fracture load of the femur is 0.5 KN, the patient would not be able to walk prior to osseointegration as axial loads of approx. 230 %BW has been suggested by several authors during gait (Heller et al. (2005),Bergmann et al. (2001)). However, clinical practice may include loading the bone fully after surgery (Olav (2012)), which could contradict this finding.

It is here assume that the forces used in impact bone grafting are greater than the threshold values found by Cummins et al. (2011). An axial force of 6KN is assumed in this analysis to ensure full contact in the prosthesis-bone interface. It is emphasized that the results of interest are of qualitative nature, but their credibility is also discussed.

In order to gain an upper bound estimate of micro motion, the most critical load scenario is used. As discussed in section 7.3, stair climbing equivalent loads found by Bergmann et al. (2001) are used along with the corresponding muscle loads.

10.2 Geometry and Boundary Conditions

In order to reproduce the impact grafting process with subsequent loading of the prosthesis, a specific loading procedure had to be used. The prosthesis was first placed into the reamed cavity of the femur, then loaded with a load mimicking impaction in the impact grafting procedure, and later loaded with loads based on daily activity (stair climbing). Between steps, all external loads are removed. In order to successfully implement this procedure, some additional steps were necessary.

Load history	
State	Description
1-Initial contact	Displacement controlled loading to ensure initial contact
2-Unloading	Removal of the displacement constraint
3-Pressing	Imposing 6KN axial force at end of prosthesis stem
4-Unloading	Removal of axial force
5-In vivo loading	Imposing In-Vivo stair climbing equivalent load field
6-Unloading	Removal of In-Vivo loads

Table 5: Steps performed in the analysis

As in the study of mesh convergence, the femur was fully constrained distally.

The initial contact between prosthesis and bone was ensured through imposition of an axial displacement. This was proven necessary to ensure convergence of the model. The displacement constraint is then removed, leaving the prosthesis hanging on the contact pressure in the canal. It is emphasized that this preliminary contact pressure should be significantly lower than the contact pressure obtained at the end of the analysis, and not affect the geometry of the model, meaning that no plastic straining is permitted.

After initial contact is obtained, an axial force is imposed to mimic the effect of the surgeon hammering the prosthesis into the reamed cavity, as assumed by Cummins et al. (2011). The axial force is enforced as a point load at the top of the prosthesis as illustrated in figure 24. The force is now removed, representing the load free state after surgery. The residual pressure field is now investigated. The residual pressure field is investigated using the paths illustrated in figure 8.5.

In vivo equivalent loads are then applied, representing physical activity of the patient soon after surgery. The stair climbing equivalent femoral loads used were enforced at the top of the prosthesis as moments and forces described in section 7.3. The muscle and femoral head loads are imposed simultaneously using a ramp function, see section appliloads. The loadings are determined equivalent to a 82kg male, corresponding to the average size of the femoral bone.

The axial displacement history is extracted from the reference point on the prosthesis neck, and the axial force is extracted as reaction force at the constrained distal end.

The imposed loads and displacements are given in the following table:

10.3 Results and Discussion

In order to verify the results, the displacement history and reaction force history are monitored. The initial contact step using displacement control was necessary to ensure convergence when the axial force was applied. The displacement used was prescribed to 3mm for all friction coefficients, which yielded convergence for the frictional coefficients of 0.6 and 0.3. However, the analysis with a frictional coefficient of 0.1 did have convergence issues for this displacement. This was overcome with an increased displacement, evident at increment 1 in figure 36. The displacement able to ensure convergence for the analysis with a frictional coefficient of 0.1 was 4.5mm. This displacement did cause the axial force to exceed the 6 KN force applied later.

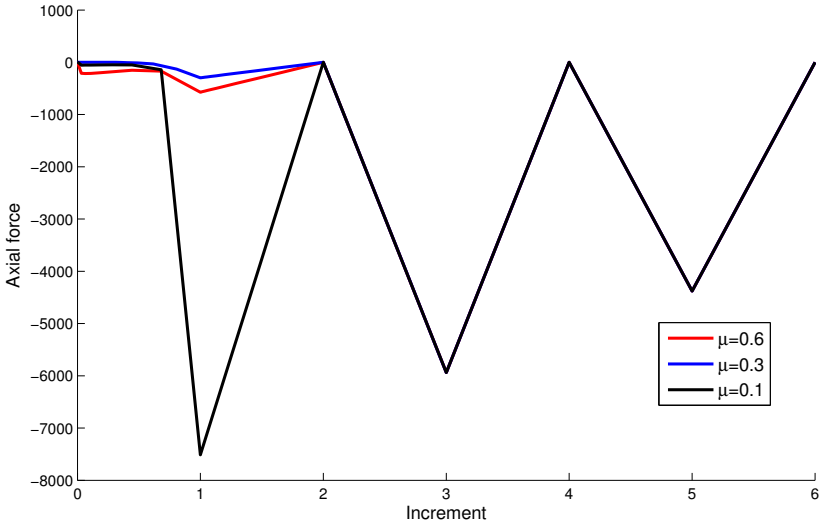

Figure 35: Force history

When the axial force was enforced later in the analysis, the displacement did increase relative to the displacement obtained initially for all friction coefficients. For the friction coefficient of 0.1, the axial load enforced in step 3 was smaller than the load resulting from the displacement controlled step 1. However, the 6KN load applied in step 3 caused a larger displacement of the prosthesis into the femoral cavity than the larger load applied in step 1. This observation seems counter-intuitive at first. This can be explained as the prosthesis was constrained at the proximal end in the displacement controlled step,

which makes the prosthesis unable to adjust to the exact shape of the femoral cavity. This explains the observation of further displacement into the femoral canal as a lower load is applied without these constraints.

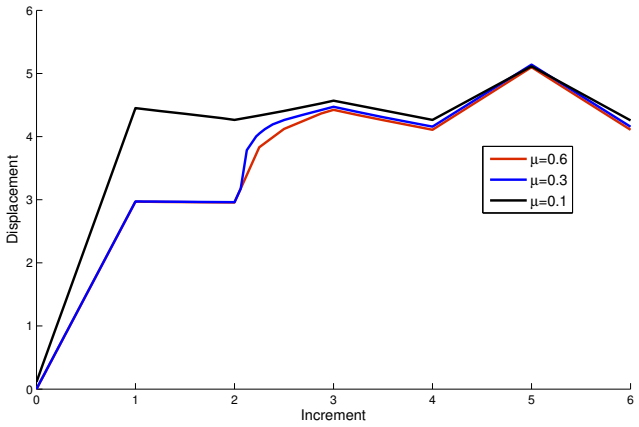

Figure 36: Displacement history

As no there is no plastic dissipation evident in these steps, the new displacement of equilibrium is assumed to be independent of the previous load history.

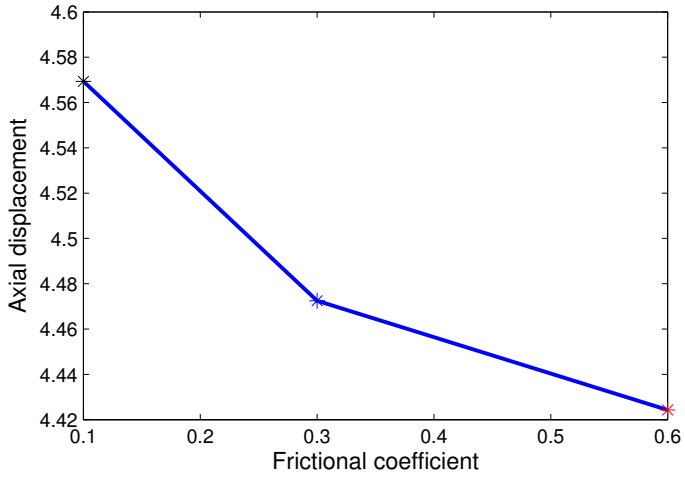

Figure 37: Displacement obtained for the 6 KN load as function of friction coefficient

In order to visualize how the friction coefficient influences the displacement of the prosthesis into the cavity of the femur, the displacement values corresponding to the 6 KN load are extracted for all friction coefficients, see figure

37. The trend observed in figure 37 indicates that the prosthesis is pressed further into the cavity in the femur as the friction coefficient is decreased. This corresponds to the discussion in section 3.1. If the forces equalizing the external load are frictional forces and contact forces, a reduction in frictional forces implies an equal increase in contact forces. The increase in contact forces is then obtained from further displacing the prosthesis into the cavity of the femur.

Based on the assumption that the 6 KN force has obtained equilibrium independent of previous load history, the investigation of the friction coefficient's influence on micro motion is performed in the following sections.

10.3.1 Contact Pressure Distributions

The contact pressure is evaluated both medially and laterally after the 6 KN grafting equivalent load is removed. The resulting pressure fields does show fluctuations along the paths, being caused by surface mesh imperfections, see figure 38 and 39.

Based on the preliminary study, an increasing contact pressure is expected as the frictional coefficient is decreased. The medial and lateral pressure distribution illustrated in figure 38 and 39 showed similar trends.

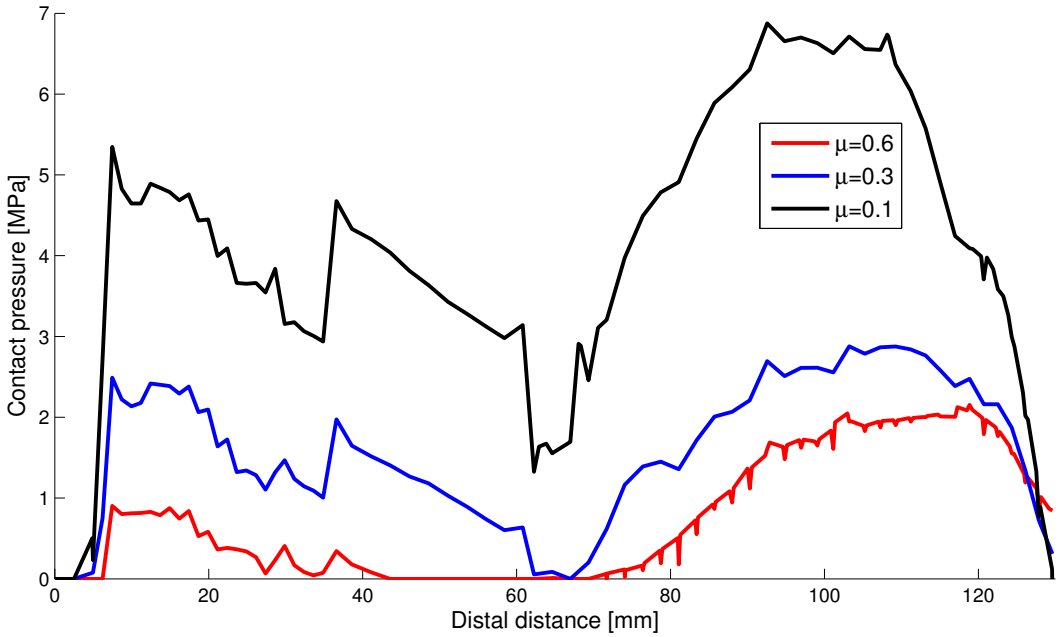

Figure 38: Medial pressure distribution along path defined in section 8.3.2 and with a 6KN pre-stressing.

The medial pressure distribution increased from a maximum contact pressure of approximately 2 MPa to approximately 7 MPa as the frictional coefficient was reduced from 0.6 to 0.1. The qualitative shape of the pressure distribution

is similar for all contact pressures, but increasing fluctuations are observed for decreasing frictional coefficients, see figure 38. The general observed trend is that a higher contact pressure is found both distally and proximally than in the midsection, with the highest pressures proximally. The increase in contact pressure towards the proximal end is pronounced for all frictional coefficients, indicating a geometrical connection. As surface of the prosthesis has a larger angle relative to the centerline of the prosthesis proximally than distally, an axial displacement would cause a larger increase in diameter proximally than distally. As the strain in the bone cavity is connected to contact pressure, this could be the mechanism causing an increased contact pressure proximally. The increase in contact pressure at the distal end of the prosthesis could be reasoned by another mechanism. As the reduced frictional coefficient causes a increased displacement of the prosthesis into the femoral cavity, the circumferential strain of the femoral shaft increases. The femoral shaft has an increased wall thickness relative to the proximal region, which could cause an increased constraint distally. An increased constraint could be a reason for the increased distal contact pressure.

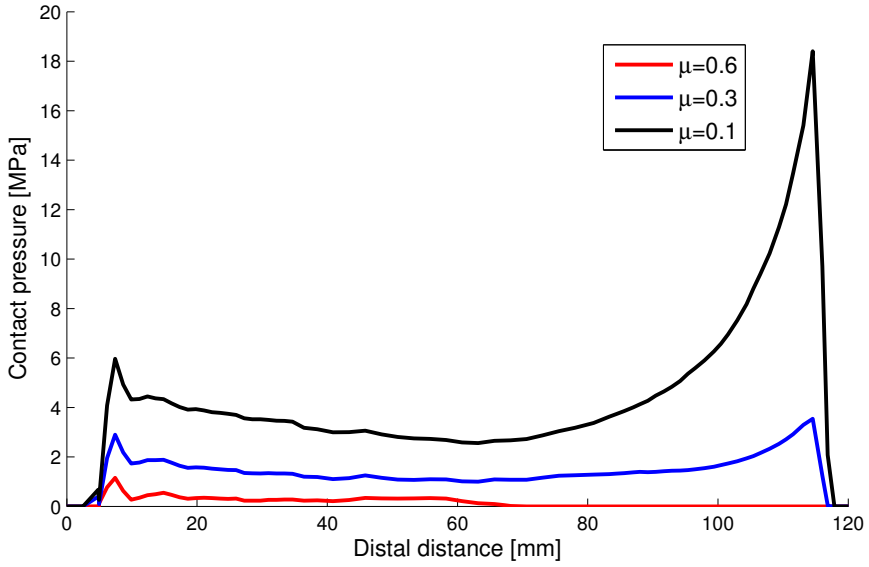

Figure 39: Lateral pressure distribution along path defined in section 8.3.2 and with a 6KN prestressing.

The lateral pressure distribution shows a large peak proximally for the lowest frictional coefficient, and a flatter pressure distribution for the higher friction coefficients. The proximal peak could be caused by the proximal end of the prosthesis bending laterally as the axial displacement is increased. The trend observed in figure 39 shows a increasing contact pressure for decreasing friction coefficient. This is consistent with findings from the medial pressure distri-

bution.

10.3.2 Interface Stresses and Unloading

In order to have some measure on the risk of femoral fracture, the frictional coefficient's effect on the maximum principal stresses is investigated.

The maximum principal stresses are exported from the same paths as the contact pressure in order to ease the comparison of the trends. The maximum principal stress is here determined by Abaqus, and its orientation is unknown. The maximum principal stress corresponds to the largest component of the diagonal stress matrix, which results from a coordinate transform where all resulting shear components are equal zero.

This lack of the stress orientation could produce conservative results of the bone's fracture strength, as the longitudinal fracture strength of cortical bone is significantly higher than the transverse fracture strength assumed critical in this investigation (Reilly & Burstein (1974)).

In figure 40 and 41 medial maximum principal stress distributions are illustrated. The medial maximum principal stress distribution does indicate that the stresses are generally increased for a reduced frictional coefficient, coinciding with the increased contact pressure. The fluctuations are reduced as the frictional coefficient is increased, as found for the medial contact pressure.

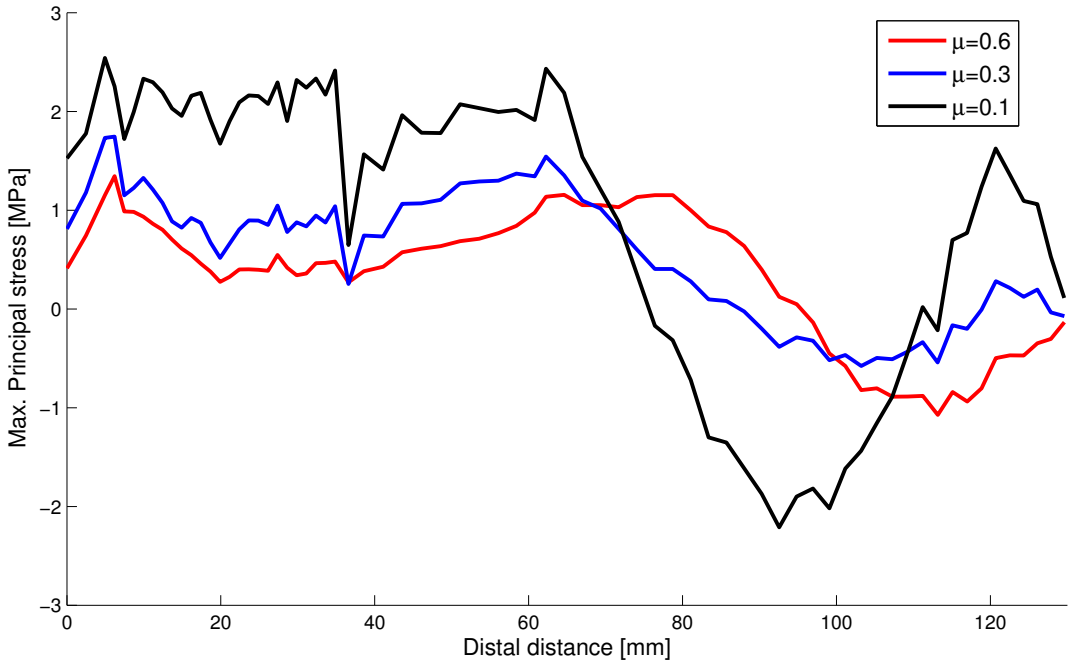

Figure 40: Medial maximum principal stress distribution along path defined in section 8.3.2.

Laterally the lowest frictional coefficient causes the highest peak stress, but does show a reduction in the peak between 80mm and 110mm. The decrease in frictional coefficient from 0.6 to 0.1 causes an approximately doubling in maximum principal stresses.

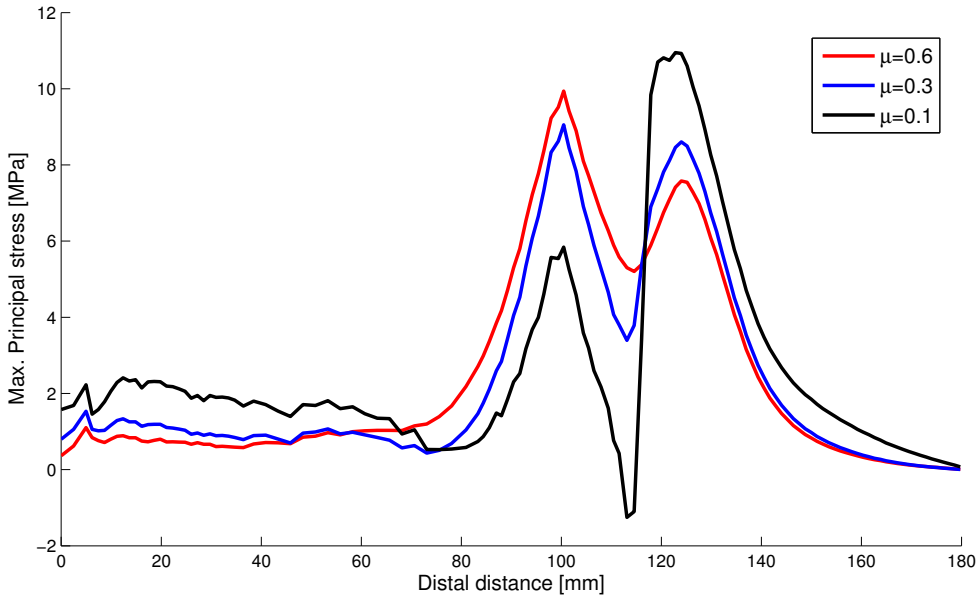

Figure 41: Lateral maximum principal stress distribution along path defined in section 8.3.2.

After the axial force mimicking the impaction force is unloaded, changes in contact pressure distribution and maximum principal stress distribution are observed. The changes in contact pressure are shown in figure 42 and 44. The changes in maximum principal stress are shown in figure 43 and 45. The contact pressures, both medially and laterally shows a reduction as the external load is removed. The reduction does vary in magnitude depending on its location. Qualitative changes in pressure distribution are observed, with a general translation towards the proximal end, see figure 42.

The changes in maximum principal stress distribution shows a limited response to the removal of the external load, see figure 43 and 45. This indicates that the maximum principal stresses are caused by the residual stresses in the femur, and not by the external load.

The peak maximum principal stress values found in the cavity of the femur did not exceed 50 MPa. The highest value found was approx. 45 MPa, indicating that a 6 KN grafting force could be possible without failure of the prosthesis. The highest maximum principal stress values were not found on the sampling path used.

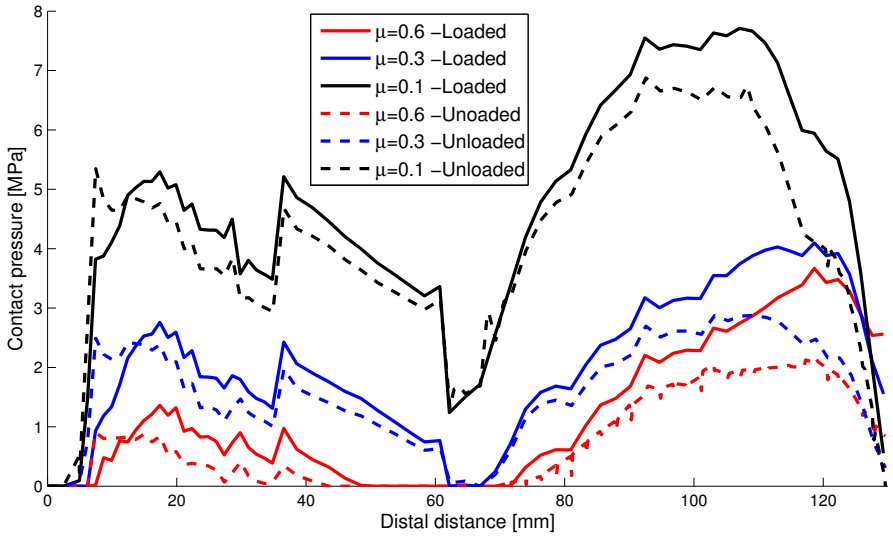

Figure 42: Medial contact pressure distributions, with and without loading.

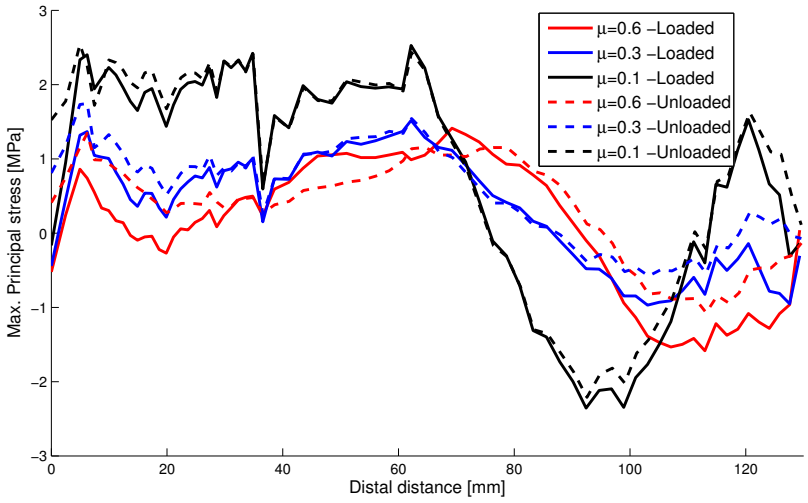

Figure 43: Medial maximum principal stress distributions, with and without loading.

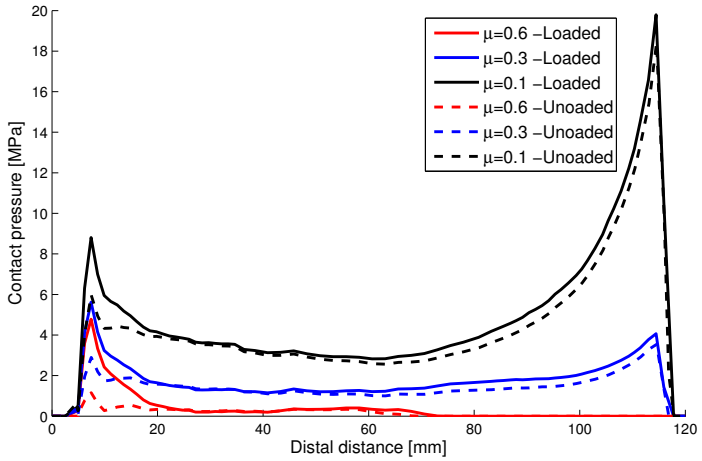

Figure 44: Lateral contact pressure distributions, with and without loading.

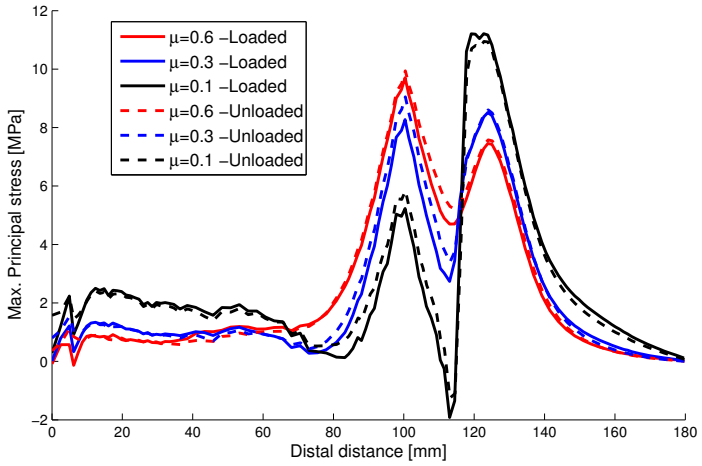

Figure 45: Lateral maximum principal stress distributions, with and without loading.

10.3.3 Micro Motion

The interface micro motion values are peak values sampled in the Gruen zones, and presented in figure 46. The lowest friction coefficient does yield the overall highest micro motion, but the highest friction coefficient does not yield the lowest micro motion. It is interesting to note that the intermediate friction coefficient actually does yield a lower micro motion value than the highest frictional coefficient. A reason for this could be a reduction of the obtained contact pressure after grafting.

The findings illustrated in figure 38 and 39 indicate that a decreased frictional coefficient yields a increased contact pressure. As coloumb friction is used, the frictional stress at sliding is linearly dependent on the contact pressure. An increase in contact pressure therefore yields an increase in frictional stress and an increased stability. However, as the frictional coefficient is decreased in order to obtain a higher contact pressure, the gain in stability may be equalized. The coupling between friction coefficient and the obtained contact pressure after grafting shows a non-linear trend. A reduction from a friction coefficient of 0.3. to 0.1 causes a larger increase in contact pressure than a reduction from 0.6 to 0.3, see fig 38. This non-linear coupling could yield a stability optimum being located within the range of frictional coefficients, coinciding with the findings illustrated in figure 46.

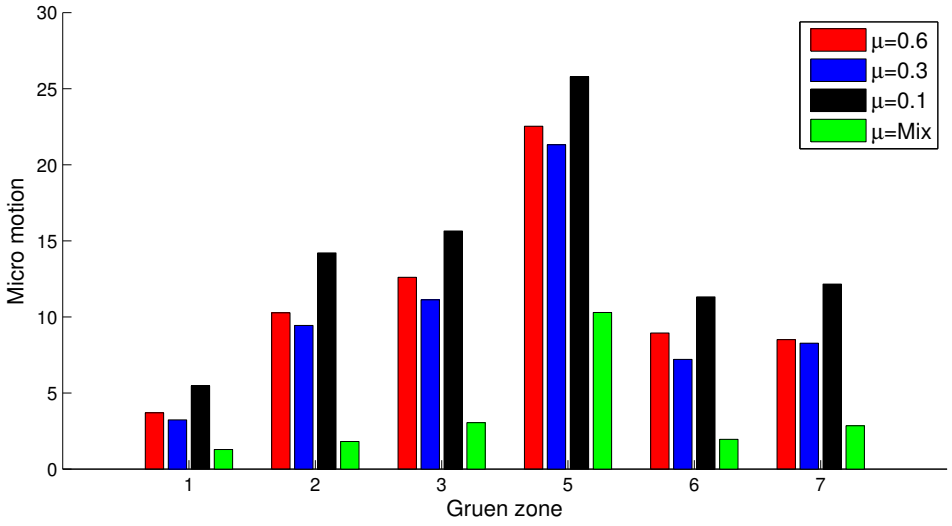

Figure 46: Micro motion values for the different Gruen zones. The Mixed friction coefficient corresponds to a lubricated grafting state.

It is found that a lower friction coefficient is a mean to obtain a increased contact pressure using the same force, which could be favorable for stability.

This potential improvement is more than equalized by the reduction if frictional stresses due to the low frictional coefficient. However, if the interface could be manipulated in such a way that the interface friction was lower upon grafting than post-surgery, this equalization could be avoided, and one could possibly expect an enhanced stability. From this investigation, the idea of interface lubrication upon impact grafting is formed.

This hypothesis was investigated with a numerical analysis identical to the analyses done for the other friction coefficients, but with a frictional coefficient of 0.1 in all states except for the stair climbing load and unloading step. In the steps mimicking stair climbing, a frictional coefficient of 0.6 was chosen. The results showed an overall reduction in interface micro movement, indicating that the technique indeed could be beneficial for the stability of the prosthesis.

10.4 Conclusion

This numerical study indicates that the lower friction coefficients yield a higher contact pressure. If the highest possible contact pressure is to be obtained without femoral failure, a reduced frictional coefficient could be one mean. The maximum interface principal stress does also show an increase, but to a lesser extent. A reduced frictional coefficient does also increase fluctuations in the contact pressure distribution, as well as in the maximum principal stress distribution.

The increase in contact pressure caused by reducing the frictional coefficient was found not to decrease interface micro motion. The highest micro motion value was found using the lowest friction coefficient, which caused the highest contact pressure. The lowest interface micro motion was found using the intermediate friction coefficient. If the frictional coefficient was reduced upon grafting and restored when loads are later applied, an enhanced stability was obtained. This gave rise to the concept of prosthesis lubrication upon impact grafting and the dissipation of this lubrication post-surgery, restoring the frictional characteristics. No such concept is known to the author, nor lubrication compatible with such an application. The numerical investigation showed significant reduction in micro motion, motivating further investigation.

11 Influence of Grafting Induced Residual Pressure Field on Micro Motion

11.1 Objective

Analyses regarding micro motion in the prosthesis-bone interface often neglect a possible residual pressure field caused by impact bone grafting. All discussed primary stability analyses but the work of Abdul-Kadir et al. (2008) assume that the only pre-stressing of the femur is performed by a force equivalent to the axial force of either a gait or a stair climbing cycle.

It is here assumed that the initial pressure field caused by the impact grafting technique could exceed this force and affect the frictional behavior and thereby micro motion in the prosthesis interface. The motivation for this hypothesis is based on the findings by Abdul-Kadir et al. (2008), highlighting the influence of interference fit on micro motion.

The following study is based on a zero-interference fit in order to isolate the effect of pre-stressing on micro motion.

Two different load scenarios are investigated, being a walking equivalent and a stair climbing equivalent load. The walking and stair climbing loads are applied in separate analyses. Stair climbing with included muscle forces has been proposed as a load scenario producing a conservative estimate of primary stability. This recommendation is based on experimental findings and numerical analyses, see section 3.2. The effect of the muscle loads are investigated for the stair climbing case in order to investigate possible connections between increased pre-stressing of the femur and the effect of muscle loads.

11.2 Geometry and Boundary Conditions

The geometry employed is as described and verified in section 8.6. The loads are applied in the same manor as described in section 10. The calculations are only performed with one frictional coefficient chosen as 0.6, coinciding with the saturated measurements by Shirazi-Adl et al. (1993). The investigated grafting equivalent axial forces are a 6 KN, 4.5 KN and a 1.85 KN load, the latter equivalent the the axial force of bodyweight at gait. 6 KN was chosen as an upper bound for the grafting equivalent loads,as the maximum principal stresses determined in section 10.3.2, were close to the transverse fracture strength of cortical bone.

Nine analyses were performed. The three grafting equivalent loads were analysed, each performed for both walking and stair climbing, with an analysis for stair climbing neglecting muscle loads.

The loading procedure was as follows:

The loads are simplified into monotonically increasing loads, as described

Load history	
State	Description
1-Initial contact	Displacement controlled loading to ensure initial contact
2-Unloading	Removal of the displacement constraint
3-Pressing	Imposing axial force at end of the prosthesis stem
4-Unloading	Removal of axial force
5-In vivo loading	Imposing In-Vivo equivalent load field
6-Unloading	Removal of In-Vivo load

Table 6: Steps performed in the analysis

in section 10.2. The loadings are determined equivalent to a 82kg male, corresponding to the size of the femoral bone.

11.3 Results and Discussion

11.3.1 Global Response

The axial force and displacement history is used for validation purpose. The plastic dissipation is also monitored to ensure that the displacement controlled step does not cause plastic deformation of the inner cavity.

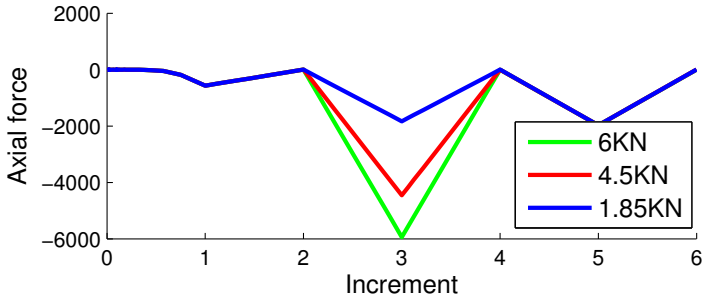

Figure 47: Axial force history. Steps as described in table 11.2.

The axial displacement is increased as the axial loading increases, causing the prosthesis to subside further into the femur. This is observed in figure 36 from step 2 to 4. The displacement shows a correlation to the applied axial loading as expected, see figure 49.

As the stair climbing load is applied in step 5, the axial force is increased as observed in figure 47. This causes a corresponding axial displacement.

The plastic dissipation is monitored, and no plastic dissipation is present in the displacement controlled step and in the unloading step. It is surprising that

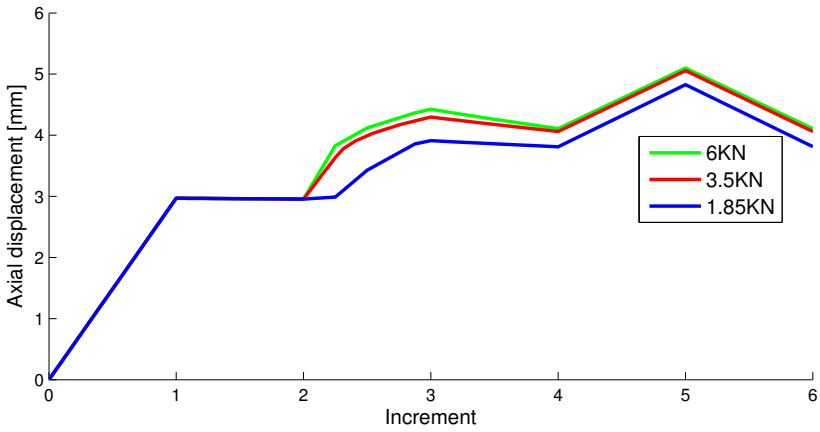

Figure 48: Axial displacement history. Steps as described in table 11.2.

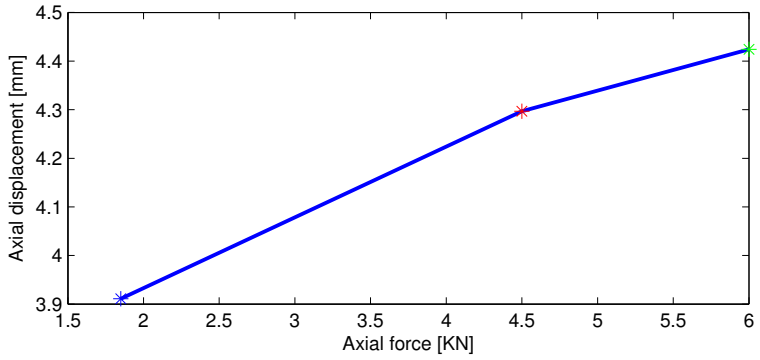

Figure 49: The displacement obtained as the grafting force is applied

no plastic dissipation is present even at maximum axial loading, indicating that the contact pressure is caused by elastic deformations.

11.3.2 The Effect of Pre-Stressing

The applied grafting equivalent loads of 6 KN, 4.5 KN and 1.85 KN resulted in different micro motion values as expected, and showed a reduction as the grafting force in increased. The loading corresponding to stair climbing are here employed as they have been found to produce the most conservative estimate of primary stability. The highest micro-motion was found in Gruen zone 5, being located medial-distally. The magnitude was found to be within the suggested threshold for osseointegration of 50microns for all zones. The largest micro

motions were generally found distally. The micro motions were generally larger medially than laterally.

The non-symmetric micro motion distribution could be explained by the resulting bending moment from the femoral head. The interface contact pressure was found largest proximally, which could explain the lower interface micro motions proximally.

The reduction of micro motion due to the increase from a 1.85KN to a 6KN grafting force, was found to be largest proximally yielding a reduction of over 50%. This is also the case medial-distally with a similar value. The grafting force of 6KN did still not produce interface principal stresses exceeding 50Mpa, which suggest that such a grafting force could be plausible in the case of a zero interference fit, using the Gladiator prosthesis.

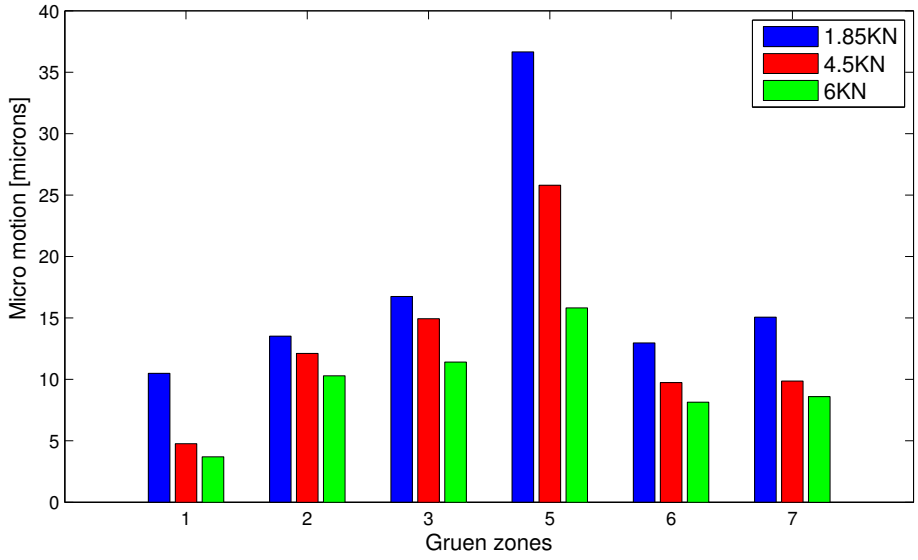

Figure 50: Micro motion in the Gruen zones for the three pre-stressing scenarios.

The reason for this reduction in micro motion for increasing axial force could be explained by the increased contact pressure as found by Abdul-Kadir et al. (2008). The frictional force is linearly dependent to the contact pressure for the assumed Coloumb model, which explains the relation between increased contact pressure and reduced micro motion. The influence does however show a non-linear relation which could be due to geometrical effects.

11.3.3 The Effect of Different Load Scenarios

In the comparison of walking and stair climbing loads on micro motion, the highest micro motion value was found for the stair climbing case including muscle forces, see figure 51. The largest micro motions are found distally with

stair climbing producing the highest values in zone 3 and 5. The influence of applied load is limited in the proximal and midsection regions.

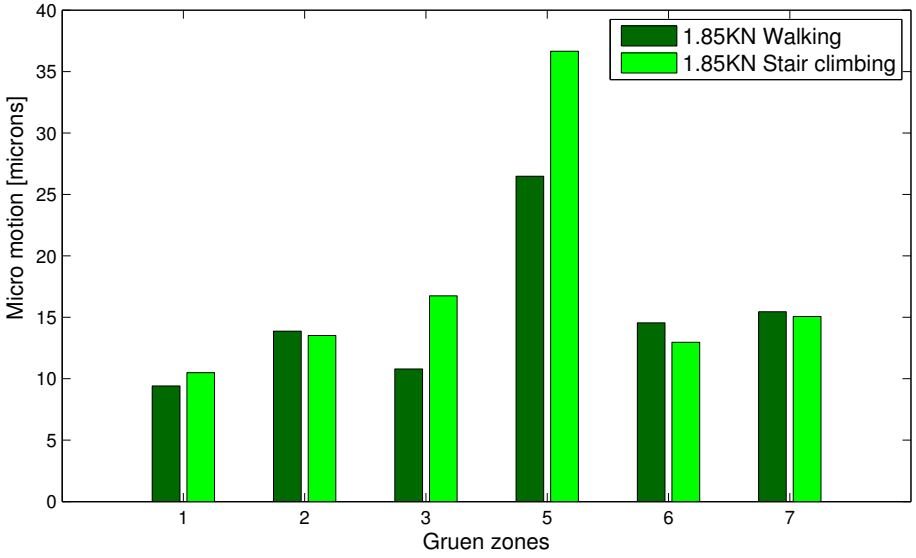

Figure 51: Micro motion in the Gruen zones for walking and stair climbing equivalent loads. Data from 1.85 KN pre-stressing.

The influence of including muscle loads on micro motion for increased contact pressures is illustrated in figure 52 for a 6 KN axial load, and in figure 53 for the 1.85 KN load. The highest micro motions were found medially for both the 1.85KN and a 6KN axial force. The peak micro motion does change location from Gruen zone 5 to 6 as the loading is increased.

Head only loads causes higher micro motions in several gruen zones. This could indicate that the muscle loads causes bending of the bone, inhibiting interface movement locally. The 6 KN grafting force indicated that the muscle loads reduces micro motion laterally and increases micro motion medially, see fig 52.

The 1.85 KN grafting load did however not show a clear trend as the muscle loads are included.

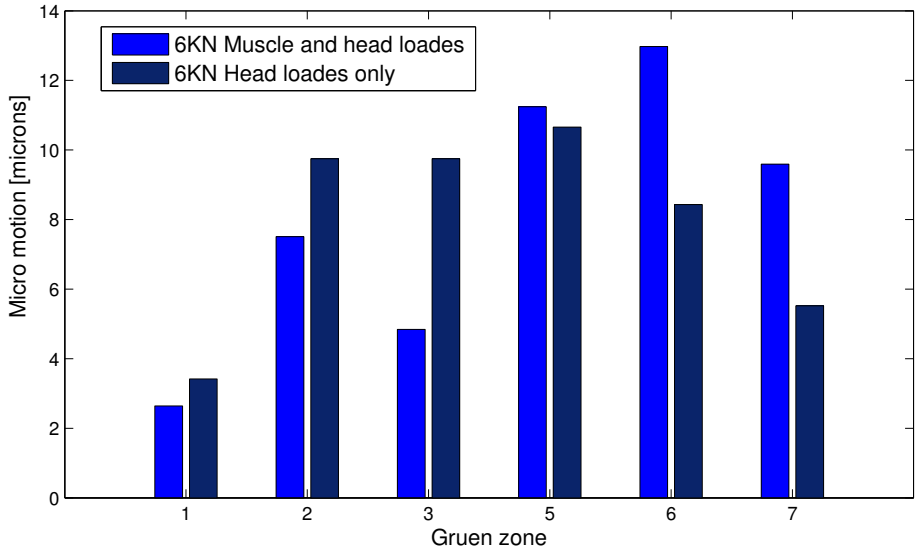

Figure 52: Micro motion in the Gruen zones for Muscle and head loads compared to head loads only. Data from 6KN pre-stressing and a walking equivalent loading.

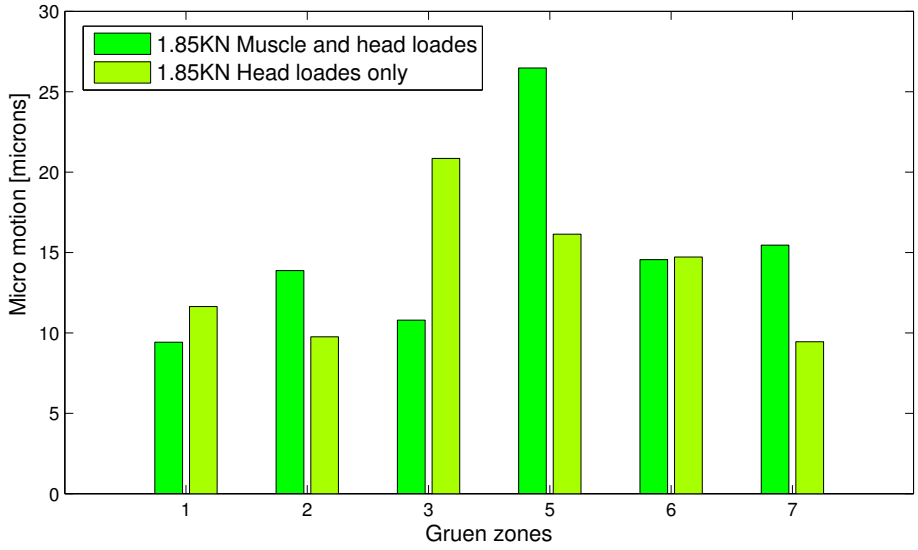

Figure 53: Micro motion in the Gruen zones for Muscle and head loads compared to head loads only. Data from 1.85KN pre-stressing and walking equivalent loads.

11.4 Conclusion

The residual pressure from the impact grafting process was generally found to reduce the interface micro motion as indicated by Abdul-Kadir et al. (2008). The grafting force's influence on micro motion is dependent on the sampling region on the prosthesis, having the largest impact proximal-laterally and at the medial-distal end. The comparison of micro motion values from walking and stair climbing loads, confirmed the findings suggesting the use of stair climbing equivalent loads for conservative estimates of primary stability.

Including muscle loads in the in-vitro load reproduction yielded the highest micro motion values for both a 6 KN and a 1.85 KN grafting load. Including muscle forces did not yield the highest micro motion values in all regions, with the neglecting of muscle forces over predicting micro motion locally.

As the grafting forces enforced by the surgeon could influence the primary stability of the prosthesis, it should be introduced as a parameter in studies of prosthesis primary stability. Based on the findings in this study, the neglecting of grafting forces could underestimate primary stability.

12 Preliminary Study of Interaction between Prosthesis and Femur

12.1 Objective

The motivation for the preliminary study is to isolate the frictional coefficient's influence on the pressure distribution between two geometries. The geometries are designed to illustrate some aspects in prosthesis-femur interaction. If the frictional coefficient influences the pressure distribution, the friction coefficient could be one additional degree of freedom for further improvement of the surgical techniques and prosthesis design.

12.2 Method

In order to isolate the effect of frictional coefficient on contact pressure distribution, two models were developed. They deviate in their objective, one meant to avoid geometrical effect, and the other geometrical effect resembling a prosthesis.

The first model constitutes of a outer conical cylinder with equal wall thickness over its entire length, and a inner plug with the same slope of the walls, see in figure 54a. The entire contact surface of the inner plug contacts the outer surface, in order to avoid contact surface area as a influencing factor. The model exploits symmetry allowing for reduced computational cost. The applied boundary conditions are illustrated in figure 54b. At the top of inner plug, a displacement is enforced which is slightly larger than neccesary to ensure contact between the bodies. Large deformations are avoided.

The second model resembles a prosthesis-femur interaction, but still with a highly simplified geometry. The outer geometry is a long slender cylinder with a inner cavity. The cavity has sloping walls as often found on commercial prostheses. The inner rod has the same slope as the outer walls, and contacts the outer cylinder with its entire sloped surface. The model exploits symmetry in order to reduce computational costs. Boundary conditions are illustrated in figure 55b.

Both meshes are generated using parabolic tetrahedrons (C310) with 28406 elements in the mesh shown in figure 54 and 56370 elements in the mesh illustrated in figure 55. The increased mesh refinement used in the slender geometry is due to meshing difficulties, as the inner cavity varies from narrow to wide. The increased mesh refinement was therefore chosen to ensure an even contact surface. The meshes were checked for global convergence through monitoring of internal energy as the meshes were refined, and the used mesh refinements were within the converged region of internal energy.

The normal contact conditions used were a linear overclosure relationship

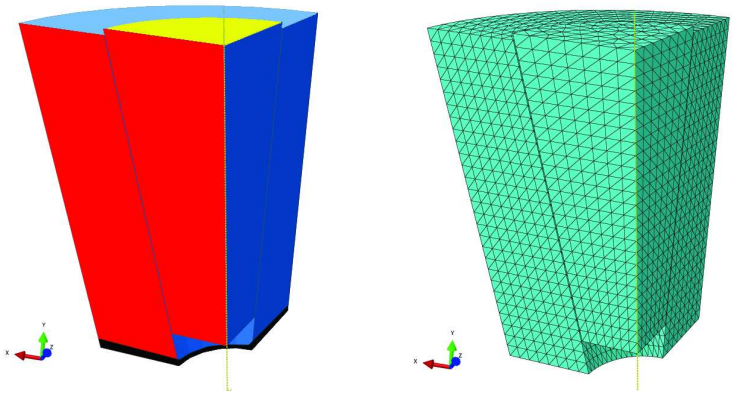

54a: Boundary conditions 54b: Mesh

Figure 54: Graphical illustration of boundary conditions and mesh. Symmetry conditions are enforce on both inner surfaces (Red and Blue), fully fixated at distal end (Black) and a axial displacement assigned at the proximal end (Yellow). The outer peremiter is fully constrained.

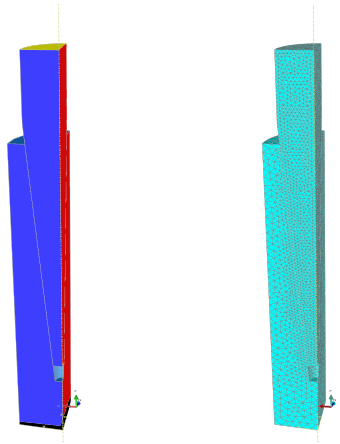

55a: Boundary conditions 55b: Mesh

Figure 55: Graphical illustration of boundary conditions and mesh. Symmetry conditions are enforce on both inner surfaces (Red and Blue), fully fixated at distal end (Black) and a axial displacement assigned at the proximal end (Yellow).

with a contact stiffness of 1300N/mm. The tangential contact was imposed using the penalty method. The materials used were a 110 GPa titanium equivalent for the inner cylinders and a 17Gpa bone equivalent for the outer cylinders. A poisons number of 0.3 were used for both materials.

The analyses were done, with the frictional coefficient varied from 0.1 to

0.6 with intervals of 0.1. The contact pressure was then extracted from paths located longitudinally at the contact interface.

12.3 Results and Discussion

The contact pressure extracted from the model illustrated in figure 54, is illustrated in figure 56. The contact pressure shows a peak at the distal end and a gradually dropping trend towards the proximal end. The highest friction coefficient produces the overall lowest contact pressure, except for at the distal end where it produces the highest local peak. The lowest friction coefficient produces the overall highest contact pressure except for at the proximal end.

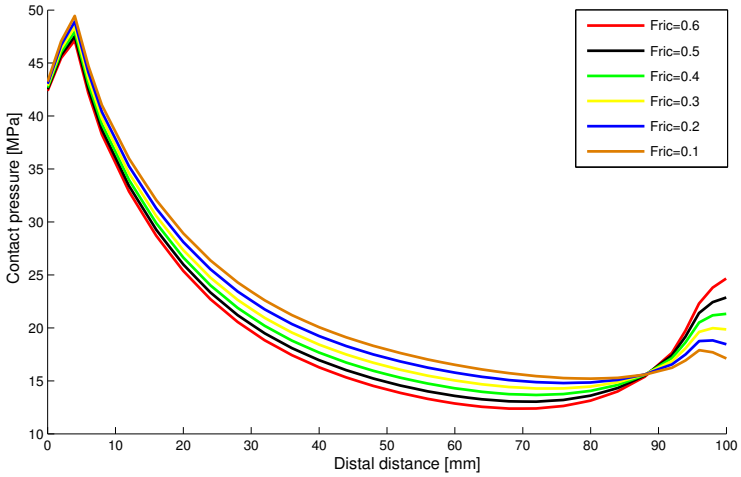

Figure 56: Contact pressure distribution of highly constrained simplified geometry.

The slender model illustrated in figure 55 produced a contact pressure distribution as illustrated in figure 57. A approximately constant slope is observed from distally to proximally. The contact pressure is increased as the frictional coefficient is reduced, having a gradual reduction towards the proximal end.

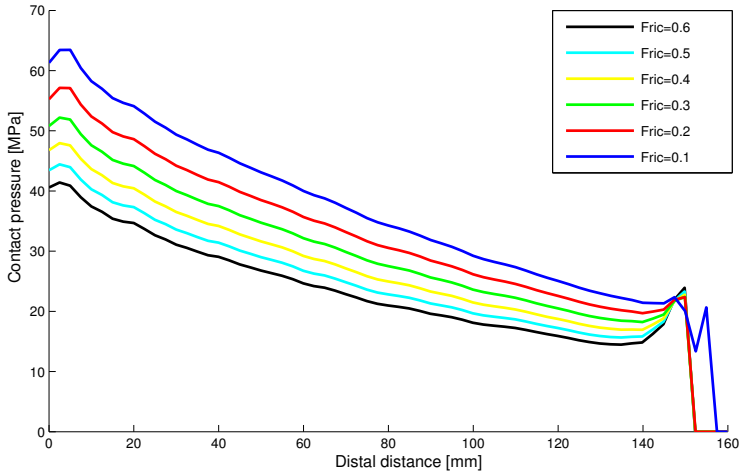

Figure 57: Contact pressure distribution of slender simplified geometry.

12.4 Conclusion

The friction coefficients influence on the contact pressure distribution is evident for both models, with the deviation between highest and lowest contact pressure being up to approximately 65%. A possible mechanism causing the reduction in contact pressure as the frictional coefficient increases is that the sum of forces in the axial direction is gradually more dominated by frictional forces. The forces in the axial direction are mainly the pressure acting on the interface decomposed axially, and the axial contribution of the frictional forces at the interface. However, the model has displacement constraints and not a force, which questions this explanation.

13 Development of a Non-Linear Friction Model

The discovery of nonlinear friction characteristics between trabecular bone and prosthesis material, and its possible influence on micro-motion, is motivates the development of a non-linear friction model. The frictional response found by Shirazi-Adl et al. (1993) shows a pronounced hardening, similar to hardening observed in metal plasticity. Plasticity theory is therefore chosen as a framework and inspiration for the structure of the algorithm. The goal for the model is to robustly reproduce the response discovered by Shirazi-Adl et al. (1993), and being applicable to 3D analyses. The extension multi axial loading lacks empirical data, and fundamental assumptions are therefore made for the responses not described by Shirazi-Adl et al. (1993).

13.1 Non-Linear Friction Characteristics

In the work of Shirazi-Adl et al. (1993) the frictional behavior of a trabecular bone-prosthesis interface was investigated. The experimental setup was based on blocks of trabecular bone extracted proximally from donor human tibias. An experimental study of the friction characteristics between the bone blocks and corresponding metal plates was done, and is here briefly summarized.

Investigation of the normal pressure's influence on the friction coefficient, and the friction's qualitative behavior was done with pressures of 0.1MPa, 0.15MPa and 0.25MPa.

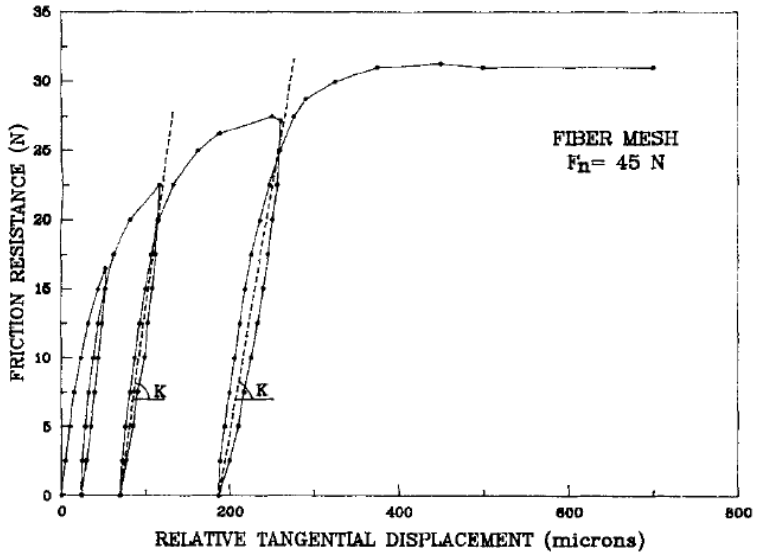

Figure 58: Frictional response found by Shirazi-Adl et al. (1993)

The extraction site of the bone specimens was found not to have significant

influence on the friction coefficient. However, the initial slope of the friction force-displacement curve does show a significant influence by the extraction site. The bone specimens extracted from the medial and lateral side of the bone showed a significantly higher initial slope.

The findings showed a highly non-linear behavior illustrated in figure 58. The tangential displacements recorded reached approximately 400 microns before the maximum resistance value was obtained. The normal displacement did not exceed 10microns. The maximum resistance value was found to be independent of the location of the extracted bone, normal load, storage time of bone in saline solution and type of coated metal plate. However, smooth metal plates tested yielded a significantly reduced friction coefficient.

The behavior of the frictional response under loading was found to be non-linear, whereas the unloading was linear. The response showed a pronounced hardening which increases as the loading exceeds the loading applied prior to unloading. The elastic response observed at unloading shows a nearly constant slope K for all plastic deformations.

13.2 The Abaqus Subroutine Interface

In order to expand the Abaqus environment to non-implemented algorithms, external subroutines can be written. Such algorithms have a predefined formating and variable feedback provided by Simulia Inc. The chosen friction subroutine for non-linear friction modeling is the FRIC routine, extensively described in the Abaqus Subroutine user's Manual. The friction subroutine is only called if the contact gap between elements is determined closed. Abaqus exports a set of parameters to the subroutine, which is updated by the subroutine and passed back to Abaqus. The parameters which have to be passed back to Abaqus are the gap parameter LM, the frictional stress τ_i, the partial derivative of the frictional stress τ_i with respect to displacement D_j being $\frac{\partial \tau_i}{\partial D_j}$ and the partial derivative of the frictional stress τ_i with respect to the contact pressure P $\frac{\partial \tau_i}{\partial P}$. Several other variables are also provided to the user, but are not necessary to update.

13.2.1 Variables

The passed gap parameter LM describes the state of contact, taking the value 0 in the case of slipping, 1 in the case of sticking and 2 if the contact surface gap is open. If the interface sticks, a no relative motion constraint is imposed using the Lagrangian multiplier method. In the case of an open gap, the friction subroutine does not need to update any variables as there is no shear stress transfer between surfaces. If however the surfaces are in sliding contact, the frictional stresses τ_i has to be estimated by the routine by any variables passed by Abaqus.

The frictional stress τ_i is updated by the subroutine, and may be estimated as a function of any variable passed from Abaqus or variables stores internally in the subroutine.

The partial derivative of the stress τ_i with respect to displacement D_j written as $\frac{\partial \tau_i}{\partial D_j}$ along with the partial derivative of the stress τ_i with respect to the contact pressure P written as $\frac{\partial \tau_i}{\partial P}$ is passed as to Abaqus for iterative purposes (Simulia (2012)).

13.3 Experimental Data Implementation

In order to develop a non-linear friction model reproducing the response found by Shirazi-Adl et al. (1993), some form of regression or interpolation method had to be employed. The experimental data was extracted from the the work of Shirazi-Adl et al. (1993), and a Voce-law as described by equation (33) was fitted. The parameters used for fitting were the constants K_1 [-] and K_2 [$\frac{1}{\text{mm}}$]. $G(\alpha)$ is here treated as the magnitude of frictional stress, with α treated as the displacement parameter. The fitting was done using a least square fitting routine. The fit was considered satisfactory with respect to the provided dataset and is illustrated in figure 59.

$$G(\alpha) = PK_1(1 - e^{-K_2\alpha}) \tag{33}$$

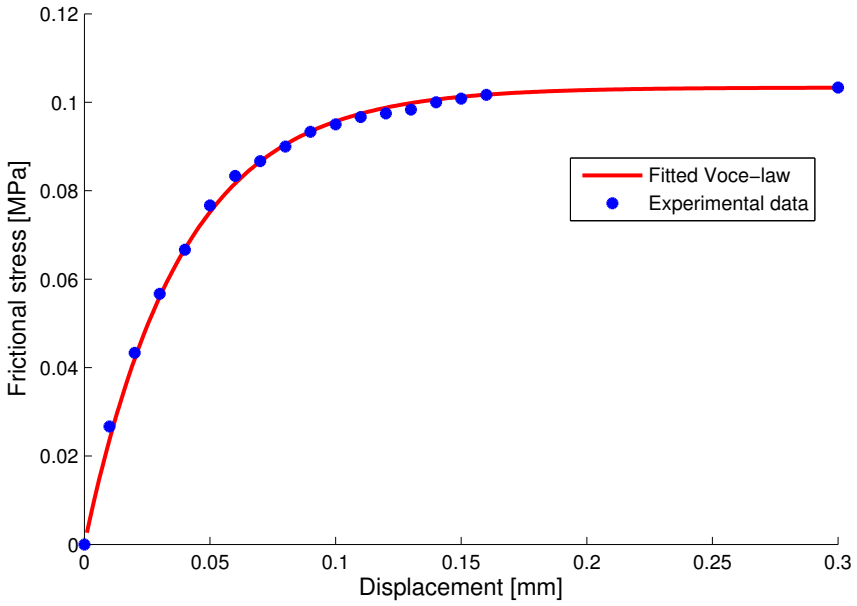

Figure 59: Fitted Voce law and experimental data from Shirazi-Adl et al. (1993), for a contact force of 45N.

The obtained parameters were $K_1 = 0.0693$ and $K_2 = 26$. The chosen unloading stiffness K was equal 3.11 Mpa/mm, corresponding to a fiber mesh plate. The fiber mesh plate refers to the surface structure of the metal plate used in the experiments by Shirazi-Adl et al. (1993), producing an intermediate value of K. These parameters correspond to a contact pressure of 0.15 MPa, which is now denoted P_{ref}.

The function described by equation (33) is later used to describe the hardening behavior of the material. $G(\alpha)$ is known as a hardening law, described by the plastic parameter α. These variables are further discussed in the following sections.

The response of a material model connecting stresses and displacement, assuming isotropic plasticity and a voce hardening law, is illustrated in figure 60. In order to reproduce the response found by Shirazi-Adl et al. (1993), the yield stress is assumed zero.

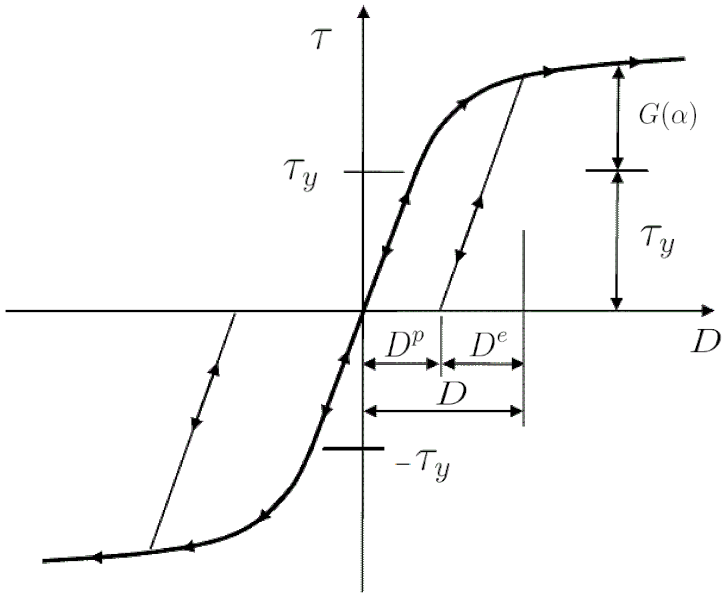

Figure 60: Isotropic hardening response, using a Voce hardening law

13.4 The Algorithmic Framework

The algorithm is inspired by the principles of plasticity theory, using an associated flow rule. The analogy to plasticity theory is chosen for the sake of convenience, but in the friction model all displacements are non-elastic in the sense that they mimic sliding. The frictional behavior to be modeled is illustrated in figure 58 and exhibits both a linear and a nonlinear response. What in plasticity theory is denoted a elastic regime, is in the friction model the linear response regime. The non-linear friction response is here analogous to a nonlinear plastic response. The terminology used in plasticity theory is here adopted to help describe the logic of the algorithm.

As no experimental data are available for bi-axial displacements, the coupling between stress components are neglected in the sense that the material stiffness matrix $[E]$ are assumed diagonal. The response is assumed isotropic with Voce hardening, and is implemented with an initial yield stress for the sake of flexibility in the case of further investigation and extension.

The derivations are inspired by the book by Simó & Hughes (1998), and adapted to the experimental data. This derivation deviates from material plasticity in the sense that it connects displacements and stress, in contrast to strain and stress. Additionally, the contact pressure is included as a parameter.

13.5 Analytical Derivation

The derivations are first done analytically and then solved using numerical schemes introduced later. A fundamental assumption is done on the frictional stress coupling to contact pressure, namely that the frictional stress is proportional to the contact pressure. This assumption simplifies the derivations, and the contact pressure P is introduced later in this derivation. The derivation begins with the definition of the main constituents and further steps are explained.

The total displacement $\{D\}$ vector can be decomposed into an elastic and an plastic part:

$$\{D\} = \{D^e\} + \{D^p\} \tag{34}$$

where

$$\{D\} = \begin{bmatrix} D_1 \\ D_2 \end{bmatrix}$$

Here $\{D\}[mm]$ denotes the total strain increment vector, $\{D^e\}[mm]$ is the elastic strain increment vector and $\{D^p\}[mm]$ is the plastic strain increment vector.

The stress increment is assumed to be a function of the elastic strain only, and through partial differentiation of equation (34) with respect to time and the introduction of Hookes law, the following expression is obtained.

$$\frac{d}{dt}\{\tau\} = [E](\frac{d}{dt}\{D\} - \frac{d}{dt}\{D^p\}) \tag{35}$$

where:

$$[E] = \begin{bmatrix} E & 0 \\ 0 & E \end{bmatrix}$$

The matrix element E is the elastic modulus with units N/mm^3. This is done as isotropy and a diagonal material stiffness matrix is assumed. This is done as no measurements on the bi-axial frictional response are available to the author.

In order to determine the transition between and elastic and a plastic state, a yield condition for isotropic hardening is introduced.

$$f = f(\tau_i, G(\alpha)) = \sqrt{\tau_1^2 + \tau_2^2} - (\tau_y + G(\alpha)) \tag{36}$$

Where:

$$G(\alpha) = PK_1(1 - e^{-k_2\alpha}) \tag{37}$$

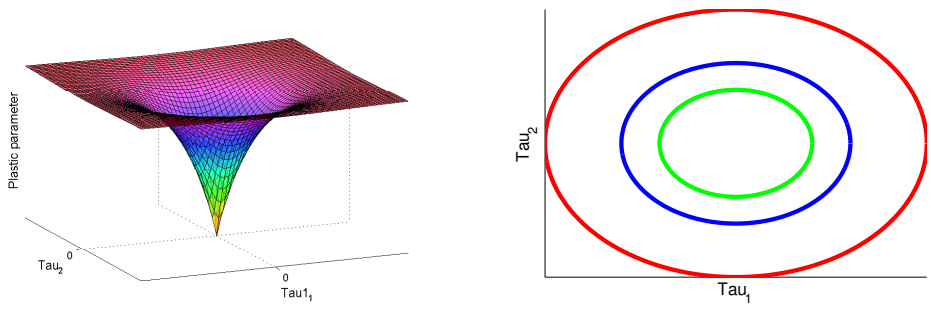

61a: 3D view

61b: 2D view

Figure 61: Graphical illustration of the yield surface. Figure a) shows the frictional stress$[MPa]$ as a function of the plastic parameter α $[mm]$, assuming a yield stress τ_y equal zero. Figure b) shows the frictional stress components $[Mpa]$ as a function of three values of the plastic variable $\alpha[mm]$.

$G(\alpha)$ is a parameter defining the isotropic hardening response of the model. The particular function here used is known as the Voce rule, which produces a good fit with the experimental data used. The parameter $\alpha[mm]$ is known as the plastic parameter, here acting as an accumulation of the plastic strain.

The yield condition can take the following three states:

$$\begin{array}{ll} f < 0 & \text{Elastic response} \\ f = 0 & \text{At yielding} \\ f > 0 & \text{Not physical} \end{array} \tag{38}$$

One of the fundamental problems in plasticity is the determination of the plastic portion$\{D^P\}$ of the displacement increment $\{D\}$. This is overcome through the use of an flow rule, here on the following form:

$$\frac{d}{dt}\{D^p\} = \{\frac{\partial Q}{\partial \tau}\}\frac{d\alpha}{dt} \tag{39}$$

The parameter $\gamma[mm/time]$ is known as the consistency parameter, here being equivalent to the time derivative of the plastic parameter. If now a associated flow rule is assumed "$Q = F$", equation 39 takes the form:

$$\frac{d}{dt}\{D^p\} = \{\frac{\partial f}{\partial \tau}\}\frac{d\alpha}{dt} = \{S\}\frac{d\alpha}{dt} = \{S\}\gamma \tag{40}$$

where

$$S = \begin{bmatrix} \frac{\tau_1}{\sqrt{\tau_1^2+\tau_2^2}} \\ \frac{\tau_2}{\sqrt{\tau_1^2+\tau_2^2}} \end{bmatrix}$$

As a mean for further determination of the consistency parameter α a loading-unloading condition is introduced, here being the Kuhn-Tucker condition:

$$\gamma \geq 0, \qquad f(\sigma) \leq 0 \qquad and \qquad \gamma f(\sigma) = 0 \tag{41}$$

In the case where $\gamma > 0$ and the term $\gamma f(\sigma)$ is to be equal zero, it necessary that $\frac{\partial f}{\partial t}$ is equal 0. Using the chain rule the following expression is given:

$$\frac{\partial f}{\partial t} = \frac{\partial f}{\partial \sigma}\frac{\partial \sigma}{\partial t} + \frac{\partial f}{\partial G}\frac{\partial G}{\partial \alpha}\frac{\partial \alpha}{\partial t} = 0 \tag{42}$$

If now equation (35) and equation (40) are inserted, an expression for the plastic parameter γ is obtained:

$$\gamma = \frac{\{S\}^T[E]\frac{\partial}{\partial t}\{D\}}{\{S\}^T E\{S\} + \frac{\partial G}{\partial \alpha}} \tag{43}$$

Where

$$\frac{\partial G}{\partial \alpha} = PK_1K_2e^{-K_2\alpha} \tag{44}$$

The tangential stiffness matrix $[C_{EP}]$ can now be found using equation (35) and inserting equation (40) and equation (43) giving:

$$\frac{\partial}{\partial t}\{\tau\} = \{D\}([E] - \frac{\{S\}\{S\}^T[E]}{\{S\}^T[E]\{S\} + \frac{\partial G}{\partial \alpha}})\frac{\partial}{\partial t} \tag{45}$$

and

$$[C_{EP}] = \frac{d\tau_i}{dD_j} = [E] - \frac{1}{E + \frac{\partial G}{\partial \alpha}}[E_S] \tag{46}$$

where $[E_S]$ is:

$$[E_S] = \begin{bmatrix} ES_1^2 & ES_1S_2 \\ ES_1S_2 & ES_2^2 \end{bmatrix}$$

It is to be noted that this tangential stiffness matrix is not necessarily equal to the algorithmic stiffness matrix. This could reduce the convergence rate, but is here neglected due to time constraints

13.6 The Numerical Algorithm

In order to solve for stresses from an arbitrary displacement, a numerical scheme is developed. The procedure used to determine the elastic and plastic strain composition is commonly known as return mapping, and the scheme is here introduced.

First a trial stress i determined assuming that no plastic flow occurs. From this trial stress, the correct stress is determined solving for the consistency parameter γ.

$$\{\tau_{n+1}\} = [E](\{D_{n+1}\} - \{D^p_{n+1}\}) \tag{47}$$

If now (47) is added $[E](\{D^p_n\} - \{D^p_n\})$, the following expression is obtained:

$$\{\tau_{n+1}\} = [E](\{D_{n+1}\} - \{D^p_n\}) - [E](\{D^p_{n+1}\} - \{D^p_n\}) \tag{48}$$

If now $\{\tau^{trial}_{n+1}\}$ is recognized as:

$$\{\tau^{trial}_{n+1}\} = [E](\{D_{n+1}\} - \{D^p_n\}) \tag{49}$$

and

$$[E](\{D^p_{n+1}\} - \{D^p_n\}) = [E]\frac{d}{dt}\{D_{n+1}\} = [E]\{S\}\Delta\gamma \tag{50}$$

the following expression is obtained:

$$\{\tau_{n+1}\} = \{\tau^{trial}_{n+1}\} - [E]S\Delta\gamma \tag{51}$$

The radial return mapping scheme determines the plastic parameter as follows:

$$\sqrt{\tau_{1(n+1)}^2 + \tau_{2(n+1)}^2} S_{i(n+1)} = \sqrt{\tau_{1(n+1)}^{trial2} + \tau_{2(n+1)}^{trial2}} S_{i(n+1)}^{trial} - \Delta\gamma E S_{i(n+1)} \tag{52}$$

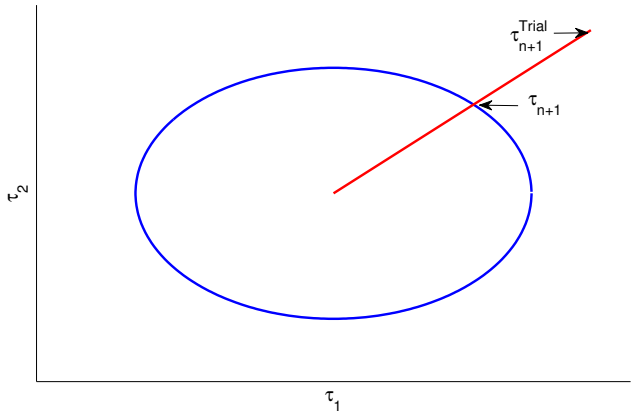

Figure 62: Illustration of radial return mapping scheme. Yield surface is shown in blue, and τ^{trial} is shown in red

The term $\sqrt{\tau_{1(n+1)}^2 + \tau_{2(n+1)}^2} S_{i(n+1)}$ represents the vector components of the stress $\tau_{i(n+1)}$, and $\sqrt{\tau_{1(n+1)}^{trial2} + \tau_{2(n+1)}^{trial2}} S_{i(n+1)}^{trial}$ represents the vector components of $\tau_{i(n+1)}^{trial}$. When the consistency parameter $\Delta\gamma$ has been determined, the vector $\tau_{i(n+1)}^{trial}$ is scaled by the term $\Delta\gamma E S_{i(n+1)}$ in order to obtain $\tau_{i(n+1)}$. The scaling is not done by multiplication with a scalar, but rather the addition of a vector with the same direction as $\tau_{i(n+1)}^{trial}$.

Rearranging of equation (52) gives:

$$S_{i(n+1)}(\sqrt{\tau_{1(n+1)}^2 + \tau_{2(n+1)}^2} + \Delta\gamma E) = S_{i(n+1)}^{trial} \sqrt{\tau_{1(n+1)}^{trial2} + \tau_{2(n+1)}^{trial2}} \tag{53}$$

We here recognize that since the consistency parameter and the stiffness both are defined positive, the following has to be true:

$$\sqrt{\tau_{1(n+1)}^{trial2} + \tau_{2(n+1)}^{trial2}} = \sqrt{\tau_{1(n+1)}^2 + \tau_{2(n+1)}^2} + \Delta\gamma E \tag{54}$$

$$\{S_{n+1}\} = \{S_{n+1}^{trial}\} \tag{55}$$

The plastic parameter is now determined based on the yield condition as described in equation 65, with the stresses as described in equation 54.

$$f_{n+1} = \sqrt{\tau_{1(n+1)}^{trial2} + \tau_{2(n+1)}^{trial2}} - \Delta\gamma E - G(\alpha_{n+1}) \tag{56}$$

If now the equation 56 is added $G(\alpha_n) - G(\alpha_n)$ and the yield condition is recognized, the following expression is found:

$$f_{n+1} = f_{n+1}^{trial} - \Delta\gamma E - G(\alpha_{n+1}) + G(\alpha_n) = 0 \tag{57}$$

The parameter α_n is now to be determined. This is done using a Newton Rapson scheme. For convenience, the parameter f_{n+1} is denoted R in the algorithm. The resulting Newton Rapson scheme is as follows:

$$R = f_{n+1}^{trial} - \Delta\gamma E - G(\alpha_{n+1}) + G(\alpha_n) \tag{58}$$

$$\frac{dR}{d\Delta\gamma} = -E + k_1 k_2 e^{-k_2(\alpha_n + \Delta\gamma)} \tag{59}$$

$$d_g = -(\tfrac{dR}{d\Delta\gamma})^{-1} R \tag{60}$$

$$\Delta\gamma = \Delta\gamma + d_g \tag{61}$$

The scheme described in (58) is repeated until $|R|$ is below a prescribed tolerance, or a given number of iterations is performed.

If now the the value of $\Delta\gamma$ is found, the stress $\{\tau_{n+1}\}$, plastic displacement $\{D_{n+1}^p\}$, plastic parameter α_{n+1} and yield condition f are updated as:

$$\{\tau_{n+1}\} = \{\tau_{n+1}^{trial}\} - [E]S\Delta\gamma \tag{62}$$

$$\{D_{n+1}^p\} = \{D_n^p\} + \Delta\gamma S \tag{63}$$

$$\alpha_{n+1} = \alpha_n + \Delta\gamma \tag{64}$$

$$f_{n+1} = \sqrt{\tau_{1(n+1)}^2 + \tau_{2(n+1)}^2} - (\sigma_y + G(\alpha_{n+1})) \tag{65}$$

In order to introduce a contact pressure dependency, it is assumed that the frictional stresses are linearly dependent of the contact pressure. In order to obtain this relation, all stresses $\{\tau_{n+1}\}$ are scaled with the factor $\{\frac{P}{P_{ref}}\}$, hereby denote P_C. This is also done with the tangent modulus $[C_{EP}]$, corresponding with that the stresses $\{\tau_{n+1}\}$ are now a product with the scalar P_C.

The partial derivative of the stresses as function of the contact pressure $\frac{\partial}{dP}\{\tau_{n+1}\}$ are now to be determined. However, since the stresses are linearly scaled by the contact pressure, the derivative simply is the frictional stress value divided by the scalar P_C. This means that:

$$\frac{\partial}{dP}\{\tau_{n+1}\} = \{\tau_{n+1}\}\frac{1}{P_C} \tag{66}$$

The resulting scheme is found in A for both Matlab. The Matlab script was used in the development and debugging phase.

13.7 Model Verification and Discussion

The development of the algorithm is based on analytical derivations, which are then numerically solved. The numerical scheme may be unstable for certain parameter combinations and displacement histories, which is the studied subject in this section.

The test scenarios are constructed to verify the algorithms ability to reproduce the experimental data provided by Shirazi-Adl et al. (1993) and to uncover logical and numerical errors or weaknesses in the algorithm. All tests are performed in Matlab, in an imitated Abaqus environment. The displacement histories are generated as in a displacement controlled analysis, and data of interest exported.

13.7.1 Parameter Sensitivity

The numerical scheme's sensitivity to parameter input is of interest as, certain parameter combinations could potentially cause stability issues. The variables, K_1,K_2 and K are varied, the pressure P fixed, and it was uncovered that the relative value of K_2 and K_1 to K had a significant impact on numerical stability. A relative increase of K did cause non-convergence in the Newton Rapson scheme. The parameters fitted to the experimental data did cause convergence issues, but an increase of the parameter K did stabilize the scheme. The parameter now used is $K = 6$ instead of $K = 3.3$, which is significantly higher than the experimental data. This increase is awaited to be negligible in pure loading scenarios, but could have significant impact when unloading is modeled. The choice to increase K instead of decreasing K_2 is due to the reproduction of the loading phase. The impact of this inconsistency is considered a point of interest for further work.

13.7.2 Experimental Data Reproduction

A displacement history similar to the experiments by Shirazi-Adl et al. (1993) was implemented in the algorithm to test its ability to reproduce the scenario. This was done in three directions being the 1,2 and a diagonal direction. The algorithm produced the data illustrated in figure 63. The reproduced data did not exactly correspond to the experimental, which is thought to be due to the plastic parameter α, not exactly correspond to the slip length as in the experimental data. The fit is however considered satisfactory, as an increase in the parameter K_2 would cause numerical instability if the slope of the unloading curve is not to be increased further.

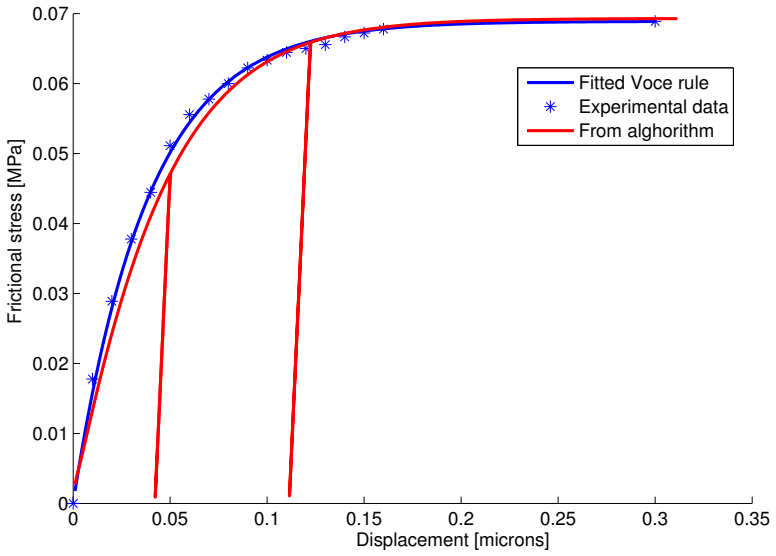

Figure 63: Comparison of algorithmic output and experimental data. Stresses in MPa and displacements in mm. A contact pressure of 0.1 MPa is her used

The change in loading direction did not cause any change in frictional stress magnitude, being of importance in finite element analysis causing displacements in multiple directions. The full output is found on the next page for the diagonally loaded case.

The algorithms response to contact pressure is illustrated in figure 64, showing a linear scaling of the frictional stress. The frictional stress at saturation is exported and plotted as function of contact pressure in figure 65. A linear trend is here observed as expected

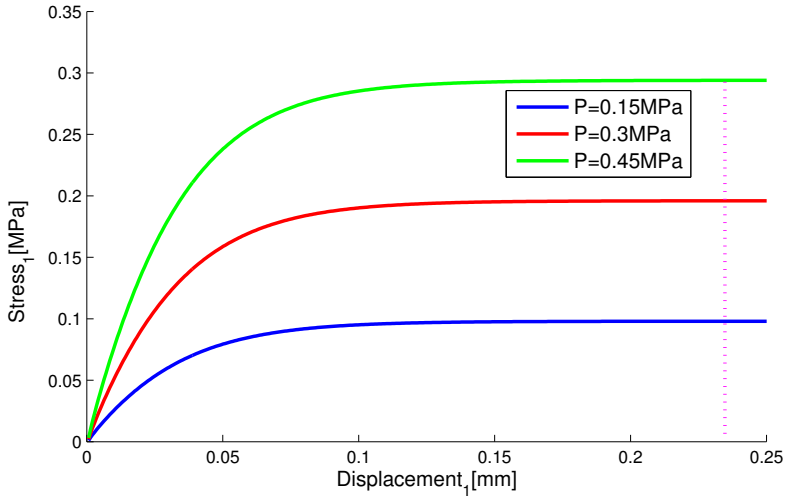

Figure 64: Frictional stress as function of displacement, for three contact pressures.

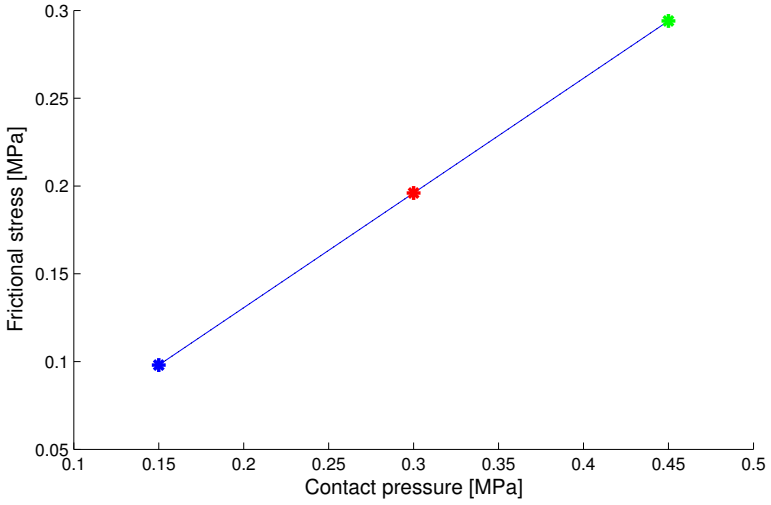

Figure 65: Illustration of frictional stress to contact pressure dependency

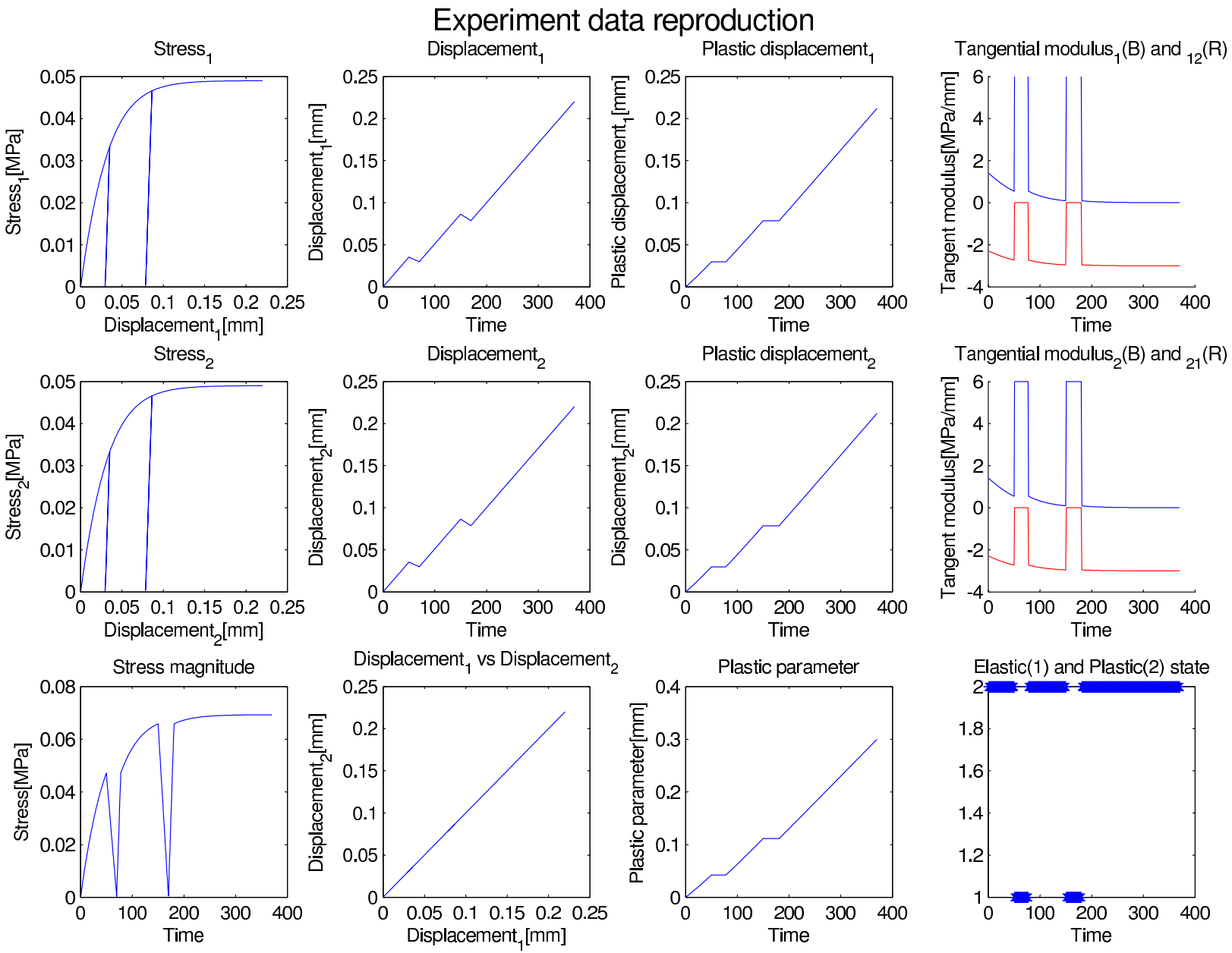
Experiment data reproduction
Stress1
Stress1[MPa]
Displacement1[mm]
Displacement1
Displacement1[mm]
Time
Plastic displacement1
Plastic displacement1[mm]
Time
Tangential modulus1(B) and 12(R)
Tangent modulus[MPa/mm]
Time
Stress2
Stress2[MPa]
Displacement2[mm]
Displacement2
Displacement2[mm]
Time
Plastic displacement2
Displacement2[mm]
Time
Tangential modulus2(B) and 21(R)
Tangent modulus[MPa/mm]
Time
Stress magnitude
Stress[MPa]
Time
Displacement1 vs Displacement2
Displacement2[mm]
Displacement1[mm]
Plastic parameter
Plastic parameter[mm]
Time
Elastic(1) and Plastic(2) state
Time

13.8 Demanding Displacement Patterns

A series of tests designed to provoke the algorithm and to cause instabilities were implemented and was not able to cause numerical instabilities. The tests were designed such that the qualitative behavior was predictable, and the results hence possible to verify in a qualitative manner. Three tests were designed, each meant to provoke different potential weaknesses.

The first test is a circular displacement pattern, which is meant to check the algorithms robustness for un-synchronized displacements passing through zero displacement.

The second test is a symmetric sinusoidal loading, one with small increments and one with very large increments. This test is meant to provoke instabilities in the case of large displacement increments.

The last test is a fully symmetric loading, which reaches a displacement plateau after the hardening law has reached full saturation.

13.8.1 Circular Displacement Pattern

The circular displacement test showed no obvious tendencies towards instability in its stress and plastic displacement reproduction as shown on the next page. The tangent modulus for both axial stresses showed a gradual decrease as anticipated, and the coupled component $C_{EP(12)}$ and $C_{EP(21)}$ fluctuated. This fluctuation in tangent modulus could be intuitively explained as the stress vector direction changes as the yield surface moves as function of the plastic displacements. No compilations or abnormalities were obvious in this test

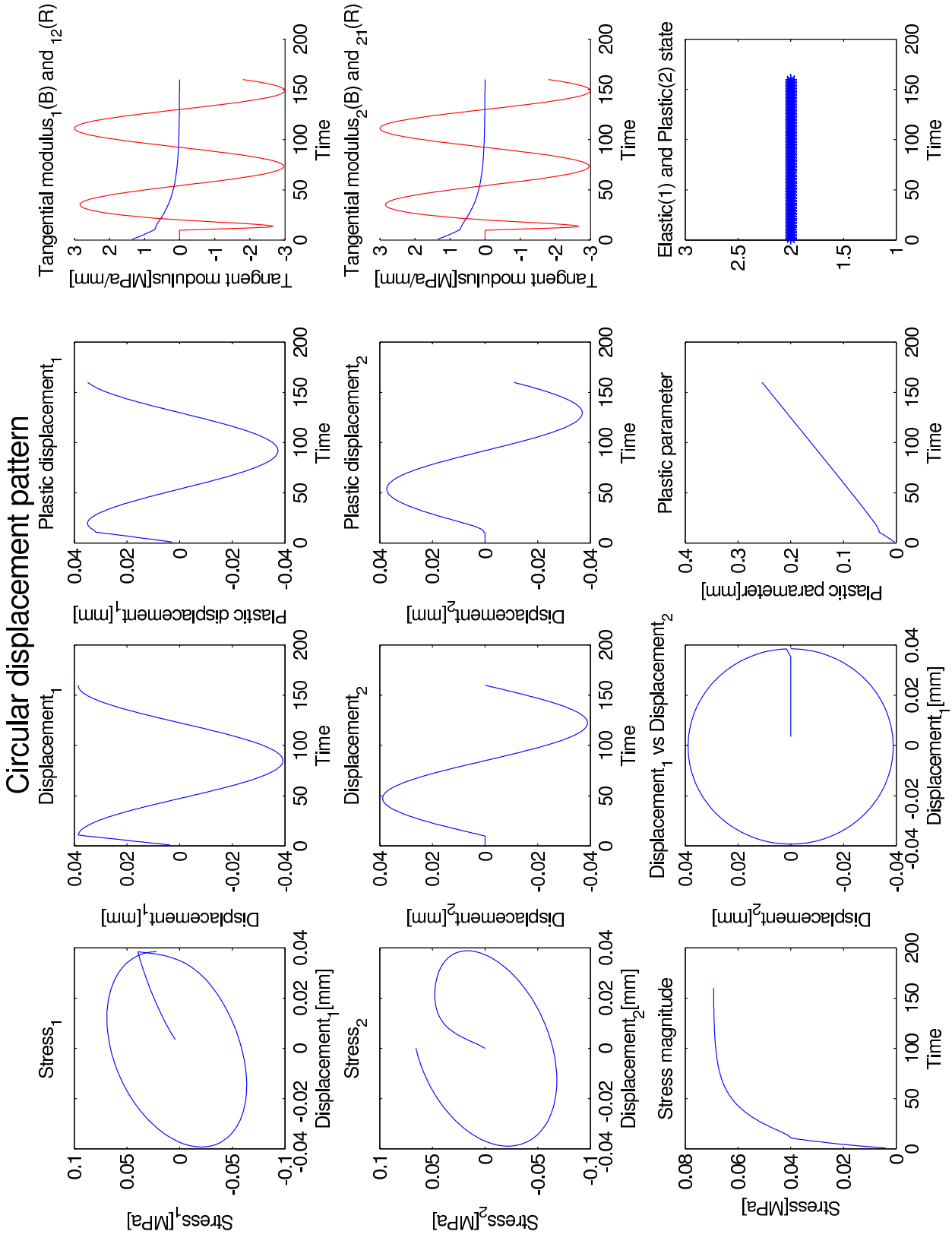
Circular displacement pattern
Displacement1
Displacement1[mm]
Time
Plastic displacement1
Plastic displacement1[mm]
Time
Tangential modulus1(B) and 12(R)
Tangent modulus[MPa/mm]
Time
Stress1
Stress1[MPa]
Displacement1[mm]
Displacement2
Displacement2[mm]
Time
Plastic displacement2
Plastic displacement2[mm]
Time
Tangential modulus2(B) and 21(R)
Tangent modulus[MPa/mm]
Time
Stress2
Stress2[MPa]
Displacement2[mm]
Displacement1 vs Displacement2
Displacement2[mm]
Displacement1[mm]
Plastic parameter
Plastic parameter[mm]
Time
Elastic(1) and Plastic(2) state
Time
Stress magnitude
Stress[MPa]
Time

13.8.2 Sinusoidal Loading and Large Increments

A sinusoidal load was implemented with both very large and very small increments. The largest increments were equal to $\pi/4$ and shown on the following page. The smallest were equal to $\pi/40$. The length of this test is shorter than necessary to saturate the hardening function $G(\alpha)$. The loading showed a hysteresis stress output as awaited, with the tangent modulus being equal to the elastic modulus in the elastic regimes. Both large and small increments yielded the same qualitative response with the only difference being the look of the plot as the output with large increments yields a courses resolution of the plots.

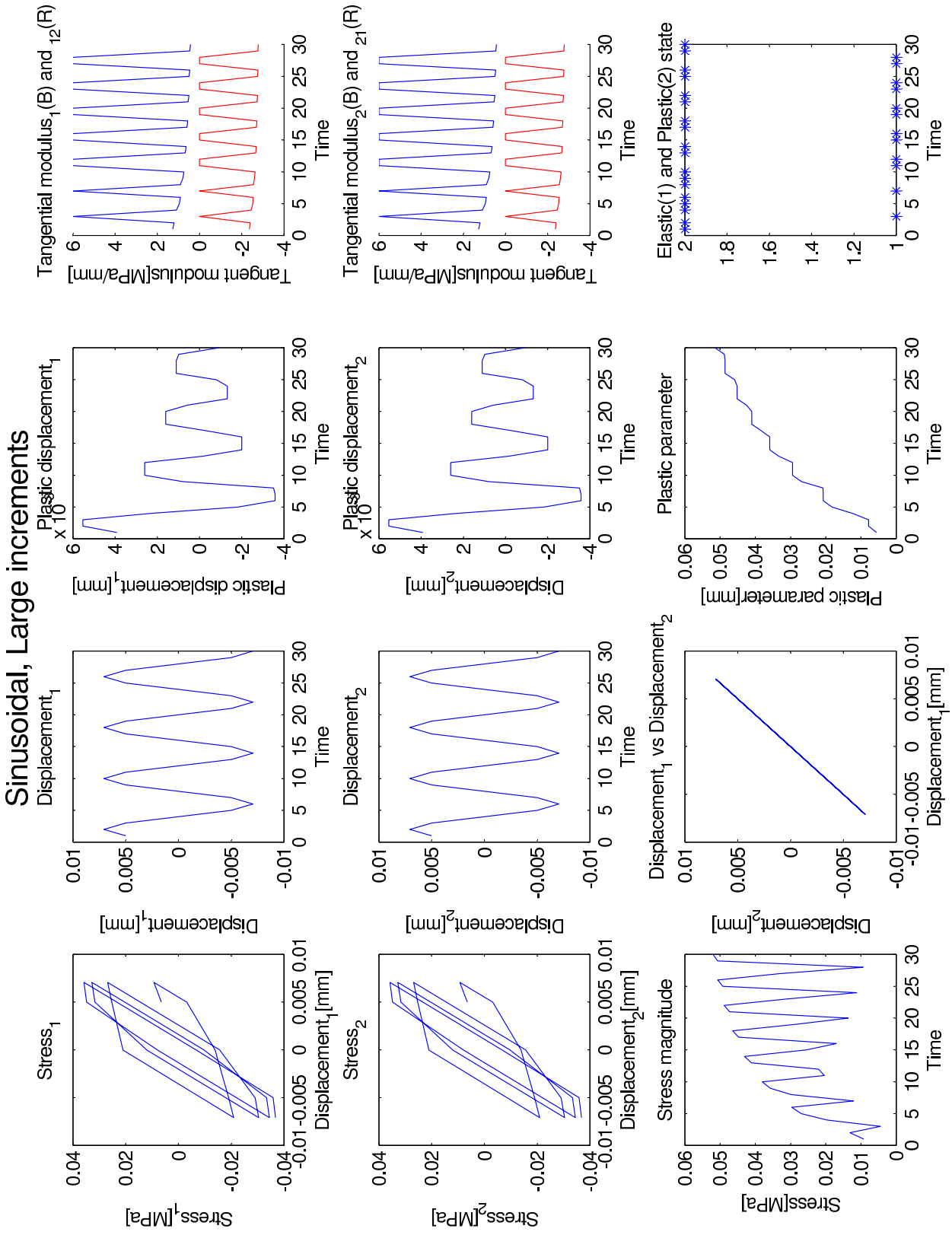
Sinusoidal, Large increments
Displacement1
Displacement2
Plastic displacement1
Plastic displacement2
Plastic parameter
Elastic(1) and Plastic(2) state
Tangential modulus1(B) and 12(R)
Tangential modulus2(B) and 21(R)
Stress1
Stress2
Displacement1 vs Displacement2
Stress magnitude
Time
Displacement1[mm]
Displacement2[mm]
Stress1[MPa]
Stress2[MPa]
Plastic displacement1[mm]
Plastic displacement2[mm]
Plastic parameter[mm]
Tangent modulus[MPa/mm]
Stress[MPa]

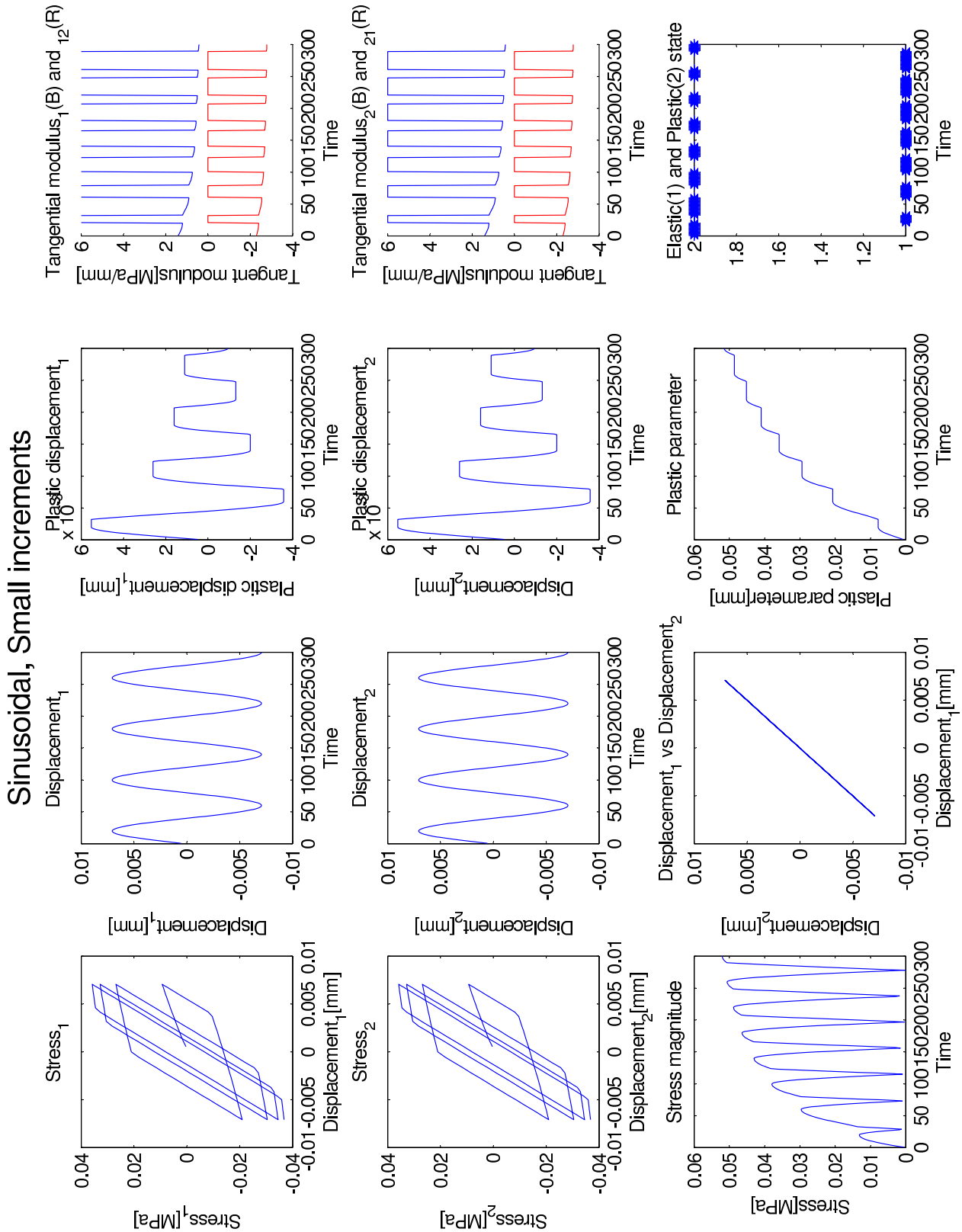
Sinusoidal, Small increments
Stress1[MPa]
Displacement1[mm]
Stress1
Displacement1
Time
Displacement1[mm]
Plastic displacement1
Plastic displacement1[mm]
Tangent modulus[MPa/mm]
Tangential modulus1(B) and 12(R)
Stress2[MPa]
Displacement2[mm]
Stress2
Displacement2
Time
Displacement2[mm]
Plastic displacement2
Plastic displacement2[mm]
Tangent modulus[MPa/mm]
Tangential modulus2(B) and 21(R)
Displacement2[mm]
Displacement1[mm]
Displacement1 vs Displacement2
Stress[MPa]
Stress magnitude
Time
Plastic parameter[mm]
Plastic parameter
Time
Elastic(1) and Plastic(2) state
Time

13.8.3 Symmetric Loading and Saturated Hardening

The load history and output are shown on the following page. The peak found around increment 200 corresponds to the elastic unloading, being physical. This can also be seen by the function changing from plastic(2) to elastic(1)[6] It is here evident that no instabilities have occurred as the hardening function reaches saturation.

[6]The output of the algorithm provides the parameter 1 if the yield condition gives a elastic state, and 2 if it yields a plastic state. This can be found in the lower right corner of the plots found in the appendix.

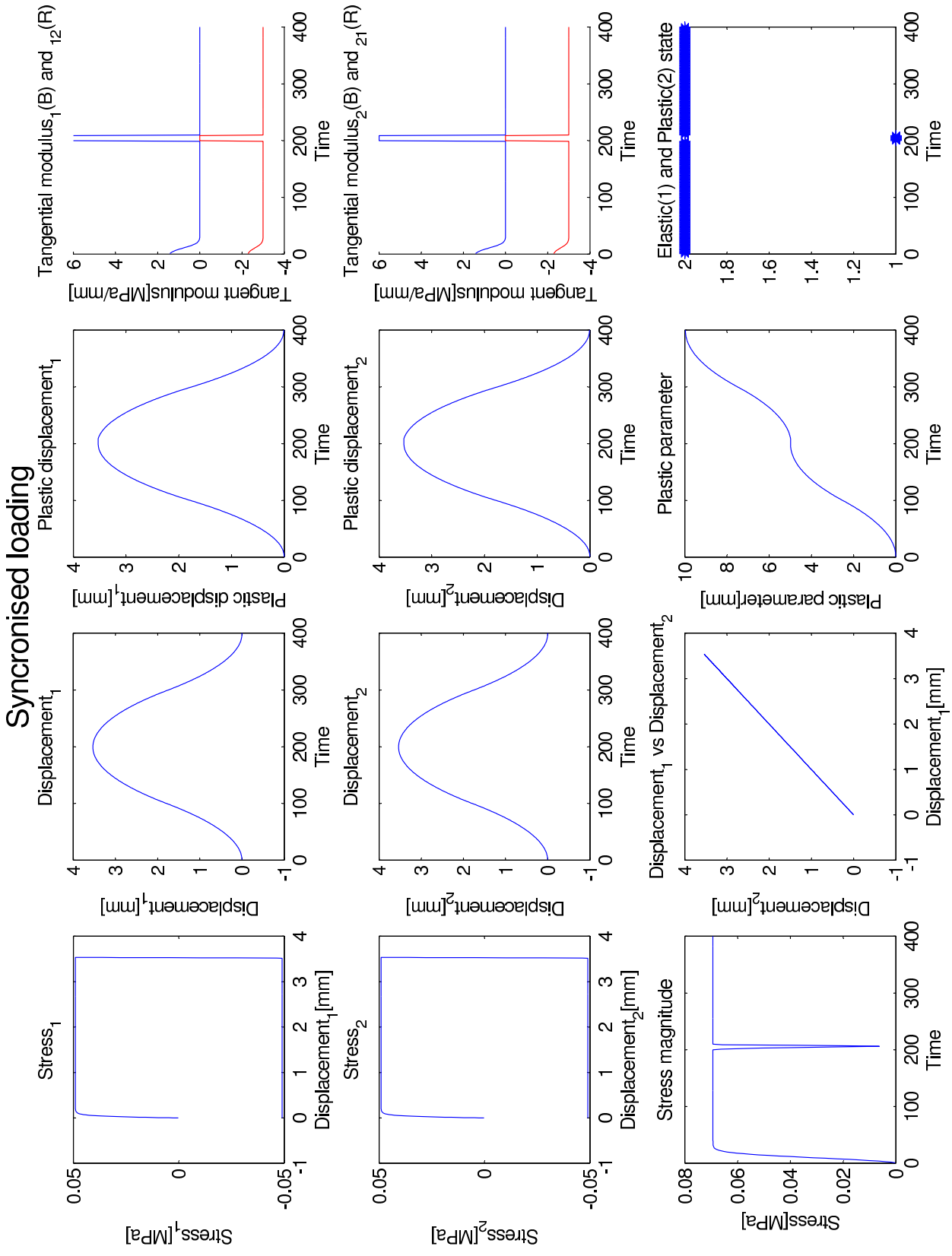
Syncronised loading
Stress1
Stress1[MPa]
Displacement1[mm]
Displacement1
Displacement1[mm]
Time
Plastic displacement1
Plastic displacement1[mm]
Time
Tangential modulus1(B) and 12(R)
Tangent modulus[MPa/mm]
Time
Stress2
Stress2[MPa]
Displacement2[mm]
Displacement2
Displacement2[mm]
Time
Plastic displacement2
Plastic displacement2[mm]
Time
Tangential modulus2(B) and 21(R)
Tangent modulus[MPa/mm]
Time
Stress magnitude
Stress[MPa]
Time
Displacement1 vs Displacement2
Displacement2[mm]
Displacement1[mm]
Plastic parameter
Plastic parameter[mm]
Time
Elastic(1) and Plastic(2) state
Time

14 Suggestions for further work

Suggestions for further work are here presented. The suggestions are based on findings of this study and points of uncertainty uncovered through discussion with experienced surgeons.

The influence of non-linear friction characteristics

The findings by Shirazi-Adl et al. (1993) suggests that the metal-trabecular bone interface characteristics deviate from those assumed in this study. The impact of this simplification is a point of interest, as a reduced friction coefficient was found to increase interface micro motion.

Experimental study on Lubricated Impact Grafting Technique (LIGT)

Findings of this study suggest that a reduced friction coefficient could be beneficial when the prosthesis is pressed into the reamed cavity of the femur, causing a higher contact pressure. If the frictional coefficient could be increased after this pressing phase, enhanced implant stability was found. This finding is based purely on this numerical study, and its relevance for real life application is still unknown. An experimental investigation could therefore be of interest. A suggestion on how to obtain such a frictional response is the use of some lubrication compound, which dissipates after a limited time. The existence of such a compound is unknown to the author.

The consequence of trabecular bone compression

Under impact grafting, the trabecular bone is both removed and compressed. The impact of the trabecular bone compression on frictional characteristics was not investigated by Shirazi-Adl et al. (1993), being a point of uncertainty. An experimental study on the trabecular compression's influence on frictional characteristics is therefore proposed.

Investigation of the reamed femoral cavity conditions

Studies as by Shirazi-Adl et al. (1993) determines frictional characteristics based on dry interface contact. However, after discussion with highly experienced surgeons it was found that the reamed cavity does contain blood, bone residue, marrow and several other materials. If the presence of these materials does affect the frictional characteristics of the bone-prosthesis interface, this could be a source of uncertainty.

15 Bibliography

Abdul-Kadir, M. R., Hansen, U., Klabunde, R., Lucas, D. & Amis, A. (2008), 'Finite element modelling of primary hip stem stability: the effect of interference fit.', *Journal of biomechanics* **41**(3), 587–94.

Baleani, M., Cristofolini, L. & Toni, a. (2000), 'Initial stability of a new hybrid fixation hip stem: experimental measurement of implant-bone micromotion under torsional load in comparison with cemented and cementless stems.', *Journal of biomedical materials research* **50**(4), 605–15.

Bayraktar, H. H., Morgan, E. F., Niebur, G. L., Morris, G. E., Wong, E. K. & Keaveny, T. M. (2004), 'Comparison of the elastic and yield properties of human femoral trabecular and cortical bone tissue', *Journal of Biomechanics* **37**(1), 27–35.

Bergmann, G. & Graichen, F. (1993), 'Hip joint loading during walking and running', *Journal of biomedical materials research* **26**(8), 969–990.

Bergmann, G., Deuretzbacher, G., Heller, M., Graichen, F., Rohlmann, a., Strauss, J. & Duda, G. N. (2001), 'Hip contact forces and gait patterns from routine activities.', *Journal of biomechanics* **34**(7), 859–71.

Bernakiewicz, M. & Viceconti, M. (2002), 'The role of parameter identification in finite element contact analyses with reference to orthopaedic biomechanics applications.', *Journal of biomechanics* **35**(1), 61–7.

Cummins, F., Reilly, P. O., Flannery, O., Kelly, D. & Kenny, P. (2011), 'Defining the impaction frequency and threshold force required for femoral impaction grafting in revision hip arthroplasty. A human cadaveric mechanical study.', *Acta orthopaedica* **82**(4), 433–7.

Duda, G. N., Heller, M., Albinger, J., Schulz, O., Schneider, E. & Claes, L. (1998), 'Influence of muscle forces on femoral strain distribution.', *Journal of biomechanics* **31**(9), 841–6.

Gilbert, L. & Jacobs, J. (1994), 'Composition and morphology of wear debris in failed uncemented total hip replacement', *The Journal of bone and joint surgery* pp. 60–67.

Götze, C., Steens, W., Vieth, V., Poremba, C., Claes, L. & Steinbeck, J. (2002), 'Primary stability in cementless femoral stems: custom-made versus conventional femoral prosthesis.', *Clinical biomechanics (Bristol, Avon)* **17**(4), 267–73.

Heller, M. O., Bergmann, G., Kassi, J.-P., Claes, L., Haas, N. P. & Duda, G. N. (2005), 'Determination of muscle loading at the hip joint for use in pre-clinical testing.', *Journal of biomechanics* **38**(5), 1155–63.

Huiskes, R., Weinans, H. & Grootenboer, H. (1986), 'Adaptive bone-remodeling theory applied to prosthetic.design analysis', *Journal of biomechanics*.
Information for Patients of Total Hip Replacement, or Total Hip Arthroplasty (THA)

Information for Patients of Total Hip Replacement, or Total Hip Arthroplasty (THA) *(02.06.2012), Website.* `http://www.jisrf.org/total_hip_replacement.htm`.

Kassi, J.-P., Heller, M. O., Stoeckle, U., Perka, C. & Duda, G. N. (2005), 'Stair climbing is more critical than walking in pre-clinical assessment of primary stability in cementless THA in vitro.', Journal of biomechanics **38***(5), 1143–54*.

*Kuiper, J. H. & Huiskes, R. (1996*a*), 'Friction and stem stiffness affect dynamic interface motion in total hip replacement.',* Journal of orthopaedic research : official publication of the Orthopaedic Research Society **14***(1), 36–43*.

*Kuiper, J. H. & Huiskes, R. (1996*b*), 'Friction and stem stiffness affect dynamic interface motion in total hip replacement.',* Journal of orthopaedic research : official publication of the Orthopaedic Research Society **14***(1), 36–43*.

Malchau, H., Herberts, P. & Ahnfelt, L. (1993), 'Prognosis of total hip replacement in Sweden', Acta Orthopaedica Scandinavica **64***(5), 497–506*.

Mann, K. a., Bartel, D. L., Wright, T. M. & Burstein, a. H. (1995), 'Coulomb frictional interfaces in modeling cemented total hip replacements: a more realistic model.', Journal of biomechanics **28***(9), 1067–78*.

Mjoberg, B. (1994), 'Theories of wear and loosening in hip prostheses', Acta Orthopaedica Scandinavica **65***(3), 361–371*.

Monti, L., Cristofolini, L. & Viceconti, M. (1999), 'Methods for quantitative analysis of the primary stability in uncemented hip prostheses.', Artificial organs **23***(9), 851–9*.

Morlock, M., Schneider, E., Bluhm, a., Vollmer, M., Bergmann, G., Müller, V. & Honl, M. (2001), 'Duration and frequency of every day activities in total hip patients.', Journal of biomechanics **34***(7), 873–81*.

Olav, F. A. (2012), 'Personal comunication with Dr.Med Olav A. Foss'.

Olufsen, S. N. (2011), Numerical Investigation of Interaction Between Human Femur and Composite Hip Prosthesis, Project work, Norwegian University of Science and Technology.

Orleans, N. (1976), 'Bone remodeling I : theory of adaptive elasticity', Journal of Elasticity **6***(3), 313–326.*

Pancanti, A., Bernakiewicz, M. & Viceconti, M. (2003), 'The primary stability of a cementless stem varies between subjects as much as between activities', Journal of Biomechanics **36***(6), 777–785.*

Park, Y., Shin, H., Choi, D., Albert, C. & Yoon, Y.-S. (2008), 'Primary stability of cementless stem in THA improved with reduced interfacial gaps.', Journal of biomechanical engineering **130***(2), 021008.*

Popoc, V. L. (2010), Contact Mechanics and Friction. Physical Principles and Application*, Springer.*

Porrino, J. a., Kohl, C. a., Taljanovic, M. & Rogers, L. F. (2010), 'Diagnosis of proximal femoral insufficiency fractures in patients receiving bisphosphonate therapy.', AJR. American journal of roentgenology **194***(4), 1061–4.*

Reggiani, B., Cristofolini, L., Varini, E. & Viceconti, M. (2007), 'Predicting the subject-specific primary stability of cementless implants during pre-operative planning: preliminary validation of subject-specific finite-element models.', Journal of biomechanics **40***(11), 2552–8.*

Reilly, D. T. & Burstein, a. H. (1974), 'Review article. The mechanical properties of cortical bone.', The Journal of bone and joint surgery. American volume **56***(5), 1001–22.*

Reilly, D. T. & Burstein, a. H. (1975), 'The elastic and ultimate properties of compact bone tissue.', Journal of biomechanics **8***(6), 393–405.*

Scand, O. (1998), 'Fluid pressure may cause periprosthetic osteolysis', Journal of Orthopaedic Research **69***(1), 1–4.*
Science Photo Library, Cortical Bone

Science Photo Library, Cortical Bone (02.06.2012), Website. `http://www.sciencephoto.com/media/301780/enlarge`.
Science Photo Library, Trabecular Bone

Science Photo Library, Trabecular Bone *(02.06.2012), Website.* `http://www.sciencephoto.com/media/301748/enlarge`.

Shirazi-Adl, A., Dammak, M. & Paiement, G. (1993), 'Experimental determination of friction characteristics at the trabecular bone/porous-coated metal interface in cementless implants.', Journal of biomedical materials research **27***(2), 167–75*.

Shultz, T. R., Blaha, J. D., Gruen, T. a. & Norman, T. L. (2006), 'Cortical Bone Viscoelasticity and Fixation Strength of Press-Fit Femoral Stems: A Finite Element Model', Journal of Biomechanical Engineering **128***(1), 7*.

Simó, J. C. & Hughes, T. J. R. (1998), Computational Inelasticity*, Springer*.

Simulia (2012), 'Abaqus 6.11 Documentation', Elements.

Soballe, K. (1992), 'Hydroxyapatite coating converts fibrous tissue to bone around loaded implants', The Journal of bone and joint surgery. America *pp. 270–278*.

Sundfeldt, M., Carlsson, L. V., Johansson, C. B., Thomsen, P. & Gretzer, C. (2006), 'Aseptic loosening, not only a question of wear: a review of different theories.', Acta orthopaedica **77***(2), 177–97*.

Viceconti, M., Muccini, R., Bernakiewicz, M., Baleani, M. & Cristofolini, L. (2000), 'Large-sliding contact elements accurately predict levels of bone-implant micromotion relevant to osseointegration.', Journal of biomechanics **33***(12), 1611–8*.

Vis, H. M. V. D., Aspenberg, P., Tigchelaar, W. & Noorden, C. J. F. V. (1999), 'Mechanical compression of a fibrous membrane surrounding bone causes bone resorption', Acta Histochemica **212***, 203–212*.

Waide, V., Cristofolini, L., Stolk, J., Verdonschot, N., Boogaard, G. & Toni, a. (2004), 'Modelling the fibrous tissue layer in cemented hip replacements: experimental and finite element methods', Journal of Biomechanics **37***(1), 13–26*.

Wriggers, P. (2006), Computational Contact Mechanics*, second edn, Springer, 30167 Hannover*.

Wright (2010), 'PROFEMUR GLADIATOR, Surgical Technique'.

A Friction subroutine (MatLab)

The MatLab script here given uses variable names which may deviate slightly from those found in the derivation in section 13. Therefore, in order to ease the reading of the scheme, the variables are here introduced.

d1n,d2n The elements of the displacement vector $\{D_{n+1}\}$

pc The pressure coefficient P_C

sitrial1,sitrial2 The elements of the trial stress vector $\{\tau_{n+1}^{trial}\}$

s1,s2 The elements of the vector$\{S_{n+1}\}$

ftrial The value of f_{n+1}^{Trial}

siy The yield stress τ_y

alphan The plastic parameter α

state Variable updated for verification of the algorithm.

sigma1,sigma The elements of the updated stress vector $\{\tau_{n+1}\}$

Cep1,Cep2,Cep12,Cep21 The elements of the tangen stiffness matrix $[C_{EP}]$

C1p,C2p The elements of the $\frac{\partial}{dP}\{\tau_{n+1}\}$ vector.

drdgamma The term $\frac{\partial R}{\partial \gamma}$ used in the Newton Rapson scheme.

dg The consistency parameter increment $\delta\Delta\gamma$

dgamma The consistency parameter $\Delta\Gamma$

dp1n,dp2n The elements of the plastic displacement vector $\{D_{n+1}^P\}$

alphan The plastic parameter α_{n+1}

```
1
2     %Update Displacement
3     d1n=d1n+inp1;
4     d2n=d2n+inp2;
5
6     %Determine Pressure Coefficient P_C
7     pc=P/0.1;
8
9     %Determine Trial Stress
10    sitrial1=E*(d1n-dp1n);
11    sitrial2=E*(d2n-dp2n);
12
13    %Determine the S_i Values
14    s1=sitrial1/sqrt(sitrial1^2+sitrial2^2);
15    s2=sitrial2/sqrt(sitrial1^2+sitrial2^2);
16
17    %Determine Yield Condition
18    ftrial=sqrt(sitrial1^2+sitrial2^2)-(siy+k1*P*(1-exp(-
          k2*alphan)));
19
20    if ftrial <= 0  %Elastic State
21
22        %Set State Variable to Elastic(1)
23        state(u)=1;
24
25        %Update Stresses
26        sigma1=sitrial1*pc;
27        sigma2=sitrial2*pc;
28
29        %Update Tanget Stiffnesses
30        Cep1=E*pc;
31        Cep2=E*pc;
32        Cep12=0;
33        Cep21=0;
34        C1p=sitrial1;
35        C2p=sitrial2;
36
37
38    else    %Plastic State
39
40        %Set State Variable to Plastic(2)
41        state(u)=2;
42
```

```
43          %Start Newton Rapson Scheme
44          R=ftrial-dgamma*E-(siy+k1*P*(1-exp(-k2*(alphan+
                dgamma))))+(siy+k1*P*(1-exp(-k2*alphan)));
45          while abs(R)>tol && i<maxiter
46              drdgamma=-E+k1*k2*P*exp(-k2*(alphan+dgamma));
47              dg=-R/drdgamma;
48              dgamma=dgamma+dg;
49              R=ftrial-dgamma*E-(siy+k1*P*(1-exp(-k2*(
                    alphan+dgamma))))+(siy+k1*P*(1-exp(-k2*
                    alphan)));
50              i=i+1;
51          end
52
53          %Reset Iteration Counter
54          i=0;
55
56          %Update Stresses
57          sigma1=(sitrial1-dgamma*E*s1)*pc;
58          sigma2=(sitrial2-dgamma*E*s2)*pc;
59
60          %Update Plastic Displacement
61          dp1n=dp1n+dgamma*s1;
62          dp2n=dp2n+dgamma*s2;
63
64          %Update Plastic Parameter
65          alphan=alphan+dgamma;
66
67          %Update Tangent Stiffnesses
68          Cep1=pc*(E*k1*P*k2*exp(-k2*alphan))/(E+k1*P*k2*
                exp(-k2*alphan));
69          Cep2=pc*(E*k1*P*k2*exp(-k2*alphan))/(E+k1*P*k2*
                exp(-k2*alphan));
70          Cep12=-pc*(E^2*s1*s2)/(E+k1*P*k2*exp(-k2*alphan))
                ;
71          Cep21=Cep12;
72          C1p=sigma1/pc;
73          C2p=sigma2/pc;
```